Article

Cancer Cell

GABAergic neuronal lineage development determines clinically actionable targets in diffuse hemispheric glioma, H3G34-mutant

Graphical abstract

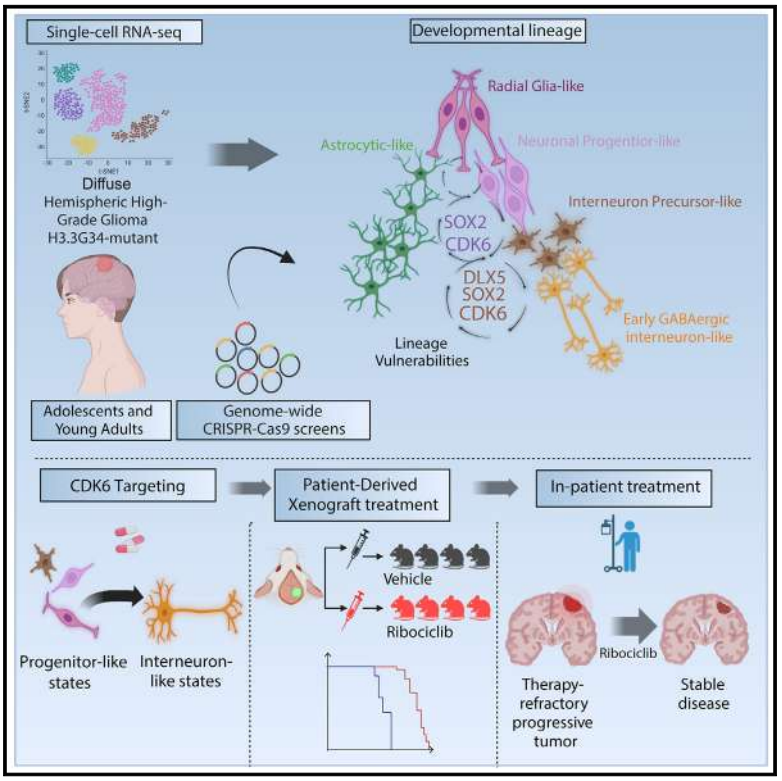

Highlights

- DHG-H3G34 follows a hierarchy along the interneuron lineage development continuum
- DHG-H3G34 tumor cells mirror spatial nests of normal human interneuron development
- Interneuron lineage progenitor states present a distinct vulnerability
- CDK6 is a promising clinically actionable target in DHG-H3G34

Authors

Ilon Liu, Gustavo Alencastro Veiga Cruzeiro, Lynn Bjerke, ..., Michelle Monje, Chris Jones, Mariella G. Filbin

Correspondence

chris.jones@icr.ac.uk (C.J.), mariella.filbin@childrens.harvard.edu (M.G.F.)

In brief

Liu et al. show that interneuron lineage progenitor-like states, emulating spatial niches of human brain development, present a distinct vulnerability and highlight CDK6 as a promising clinically actionable target in H3G34-mutant diffuse hemispheric glioma (DHG-H3G34).

Liu et al., 2024, Cancer Cell *42*, 1528–1548
September 9, 2024
https://doi.org/10.1016/j.ccell.2024.08.006

CellPress

CellPress
OPEN ACCESS

Cancer Cell

Article

GABAergic neuronal lineage development determines clinically actionable targets in diffuse hemispheric glioma, H3G34-mutant

Ilon Liu,[1,2,3,4,38] Gustavo Alencastro Veiga Cruzeiro,[1,2,38] Lynn Bjerke,[5,38] Rebecca F. Rogers,[5,38] Yura Grabovska,[5] Alexander Beck,[6] Alan Mackay,[5] Tara Barron,[7] Olivia A. Hack,[1,2] Michael A. Quezada,[7] Valeria Molinari,[5] McKenzie L. Shaw,[1,2] Marta Perez-Somarriba,[8] Sara Temelso,[5] Florence Raynaud,[9] Ruth Ruddle,[9] Eshini Panditharatna,[1,2] Bernhard Englinger,[1,2,10,11] Hafsa M. Mire,[1,2] Li Jiang,[1,2] Andrezza Nascimento,[1,2] Jenna LaBelle,[1,2] Rebecca Haase,[1,2] Jacob Rozowsky,[1,2] Sina Neyazi,[1,2] Alicia-Christina Baumgartner,[1,2] Sophia Castellani,[1,2] Samantha E. Hoffman,[1,2] Amy Cameron,[12] Murry Morrow,[12] Quang-De Nguyen,[12] Giulia Pericoli,[13]

(Author list continued on next page)

[1]Department of Pediatric Oncology, Dana-Farber Boston Children's Cancer and Blood Disorders Center, Boston, MA 02215, USA
[2]Broad Institute of Harvard and MIT, Cambridge, MA 02142, USA
[3]Department of Neurology with Experimental Neurology, Charité – Universitätsmedizin Berlin, Corporate Member of Freie Universität Berlin und Humboldt-Universität zu Berlin, 10117 Berlin, Germany
[4]Berlin Institute of Health at Charité – Universitätsmedizin Berlin, BIH Biomedical Innovation Academy, BIH Charité Digital Clinician Scientist Program, 10117 Berlin, Germany
[5]Division of Molecular Pathology, The Institute of Cancer Research, Sutton, Surrey SM2 5 NG, UK
[6]Center for Neuropathology, Ludwig-Maximilians-University, 81377 Munich, Germany
[7]Department of Neurology and Neurological Sciences, Stanford University School of Medicine, Stanford, CA 94305, USA
[8]Children & Young People's Unit, Royal Marsden Hospital NHS Trust, Sutton, Surrey SM2 5 NG, UK
[9]Division of Cancer Therapeutics, The Institute of Cancer Research, London SW7 3RK, UK
[10]Department of Urology, Comprehensive Cancer Center, Medical University of Vienna, 1090 Vienna, Austria
[11]Center for Cancer Research, Comprehensive Cancer Center, Medical University of Vienna, 1090 Vienna, Austria
[12]Lurie Family Imaging Center, Center for Biomedical Imaging in Oncology, Dana-Farber Cancer Institute, Boston, MA 02215, USA
[13]Department of Onco-haematology, Gene and Cell Therapy, Bambino Gesù Children's Hospital-IRCCS, 00165 Rome, Italy
[14]Department of Pediatrics and Adolescent Medicine, Comprehensive Center for Pediatrics and Comprehensive Cancer Center, Medical University of Vienna, 1090 Vienna, Austria
[15]Department of Neurosurgery, Medical University of Vienna, 1090 Vienna, Austria

(Affiliations continued on next page)

SUMMARY

Diffuse hemispheric gliomas, H3G34R/V-mutant (DHG-H3G34), are lethal brain tumors lacking targeted therapies. They originate from interneuronal precursors; however, leveraging this origin for therapeutic insights remains unexplored. Here, we delineate a cellular hierarchy along the interneuron lineage development continuum, revealing that DHG-H3G34 mirror spatial patterns of progenitor streams surrounding interneuron nests, as seen during human brain development. Integrating these findings with genome-wide CRISPR-Cas9 screens identifies genes upregulated in interneuron lineage progenitors as major dependencies. Among these, CDK6 emerges as a targetable vulnerability: DHG-H3G34 tumor cells show enhanced sensitivity to CDK4/6 inhibitors and a CDK6-specific degrader, promoting a shift toward more mature interneuron-like states, reducing tumor growth, and prolonging xenograft survival. Notably, a patient with progressive DHG-H3G34 treated with a CDK4/6 inhibitor achieved 17 months of stable disease. This study underscores interneuronal progenitor-like states, organized in characteristic niches, as a distinct vulnerability in DHG-H3G34, highlighting CDK6 as a promising clinically actionable target.

INTRODUCTION

High-grade gliomas (HGG) are lethal primary brain cancers and represent the leading cause of cancer-related deaths in children and adolescents.[1] Around half of pediatric HGGs are classified into clinical-molecular subgroups by mutually exclusive driver mutations at either lysine 27 (K27M) or glycine 34 (G34R/V) in the tail of histone 3 (H3),[2–5] each thought to arise from specific

CellPress
OPEN ACCESS

Sibylle Madlener,[14] Lisa Mayr,[14] Christian Dorfer,[15] Rene Geyeregger,[16] Christopher Rota,[17] Gerda Ricken,[18] Keith L. Ligon,[2,19,20,21] Sanda Alexandrescu,[21] Rodrigo T. Cartaxo,[22] Benison Lau,[22] Santhosh Uphadhyaya,[22] Carl Koschmann,[22] Emelie Braun,[23] Miri Danan-Gotthold,[23] Lijuan Hu,[23] Kimberly Siletti,[23] Erik Sundström,[24] Rebecca Hodge,[25] Ed Lein,[25] Sameer Agnihotri,[26] David D. Eisenstat,[27] Simon Stapleton,[28] Andrew King,[29] Cristina Bleil,[30] Angela Mastronuzzi,[13] Kristina A. Cole,[31] Angela J. Waanders,[32] Angel Montero Carcaboso,[33] Ulrich Schüller,[34] Darren Hargrave,[35] Maria Vinci,[13] Fernando Carceller,[8,36] Christine Haberler,[18] Irene Slavc,[14] Sten Linnarsson,[23] Johannes Gojo,[1,14] Michelle Monje,[7,37] Chris Jones,[5,39,*] and Mariella G. Filbin[1,2,39,40,*]
[16]Clinical Cell Biology, Children's Cancer Research Institute (CCRI), Vienna 1090, Austria
[17]Department of Neurobiology, Harvard Medical School, Boston, MA 02215, USA
[18]Division of Neuropathology and Neurochemistry, Department of Neurology, Medical University of Vienna, Vienna 1090, Austria
[19]Department of Oncologic Pathology, Dana-Farber Cancer Institute, Boston, MA 02215, USA
[20]Department of Pathology, Brigham and Women's Hospital, Boston, MA 02215, USA
[21]Department of Pathology, Boston Children's Hospital, Boston, MA 02115, USA
[22]Department of Pediatrics, University of Michigan, Ann Arbor, MI 48109, USA
[23]Division of Molecular Neurobiology, Department of Medical Biochemistry and Biophysics, Karolinska Institute, 17177 Stockholm, Sweden
[24]Division of Neurodegeneration, Department of Neurobiology, Care Sciences and Society, Karolinska Institute, 17177 Stockholm, Sweden
[25]Allen Institute for Brain Science, Seattle, WA 98109, USA
[26]Departments of Neurosurgery and Pediatrics, Children's Hospital of Pittsburgh, University of Pittsburgh School of Medicine, Pittsburgh, PA 15224, USA
[27]Murdoch Children's Research Institute, Department of Paediatrics, University of Melbourne, Parkville, VIC 3052, Australia
[28]Department of Neurosurgery, St George's Hospital NHS Trust, London SW17 0QT, UK
[29]Department of Neuropathology, King's College Hospital NHS Trust, London SE5 9RS, UK
[30]Department of Neurosurgery, King's College Hospital NHS Trust, London SE5 9RS, UK
[31]Division of Oncology, Children's Hospital of Philadelphia, Philadelphia, PA 19104, USA
[32]Ann & Robert H Lurie Children's Hospital of Chicago, Chicago, IL 60611, USA
[33]Laboratory of Molecular Oncology, Hospital Sant Joan de Déu, 08950 Barcelona, Spain
[34]Institute of Neuropathology, University Medical Center Hamburg-Eppendorf, 20251 Hamburg, Germany
[35]University College London Great Ormond Street Institute for Child Health, London WC1N 1EH, UK
[36]Division of Clinical Studies, The Institute of Cancer Research, London SW7 3RK, UK
[37]Howard Hughes Medical Institute, Stanford, CA, USA
[38]These authors contributed equally
[39]These authors contributed equally
[40]Lead contact
*Correspondence: chris.jones@icr.ac.uk (C.J.), mariella.filbin@childrens.harvard.edu (M.G.F.)
https://doi.org/10.1016/j.ccell.2024.08.006

spatiotemporally restricted cellular lineages.[6,7] Diffuse midline gliomas harboring the K27M mutation (DMG-H3K27) are present primarily in early- to mid-childhood within midline neuroanatomical structures, and extensive studies have demonstrated the pivotal role of an oligodendroglial precursor lineage as a main driver and rational therapeutic target.[8–16] In contrast, diffuse hemispheric glioma, H3G34-mutant (DHG-H3G34), which is present mainly in adolescence and accounts for more than 30% of pediatric or adolescent HGG, is almost exclusively localized in the cerebral hemispheres, and is relatively understudied. DHG-H3G34 have been shown to be molecularly distinct from their H3K27-altered and H3-wild-type counterparts,[2,17,18] and more recent studies indicate an interneuronal lineage as the putative origin of DHG-H3G34.[19–21]

However, the full developmental spectrum and functional role of this interneuronal lineage in DHG-H3G34 remain incompletely understood, in particular if and how this represents a distinctive cellular state which may be harnessed for lineage-directed therapeutic strategies against this deadly glioma type.

Here, we aimed to address these questions, resolving DHG-H3G34 tumor cells along a continuum of interneuronal lineage development. Genes upregulated in interneuronal lineage progenitor-like cells exhibited distinct vulnerabilities in DHG-HG34, with CDK6 emerging as a druggable target. Targeting CDK6 shifted tumor cells toward more mature states, reduced tumor growth and prolonged survival. Together, we show that targeting developmental states of the interneuronal lineage presents a potential clinically actionable strategy in DHG-H3G34.

RESULTS

DHG-H3G34 display a continuum of cell states resembling interneuronal lineage development

DHG-H3G34 has been shown to arise from interneuronal lineage progenitors,[17,19–21] whose full developmental spectrum, phenotypes, and functional significance remain to be dissected. To address this question, we started by analyzing an extended bulk transcriptomic cohort of 191 pediatric patient HGGs comprising previously published as well as new patient tumor data.[17,22–24] We observed an enrichment of transcription factors (TFs) and marker genes (e.g., *DLX1*,*2*,*5*,*6*, *FOXG1*, and *ARX*) of forebrain interneuron specification in DHG-H3G34 compared to DMG-H3K27 and H3-wild-type HGG (Figures 1A, 1B, and S1A; Table S1). Next, we profiled the single-cell transcriptomes of nine (8 untreated, 1 treated) patient DHG-H3G34 tumors using the full-transcript-length Smart-Seq2 technique, obtaining n = 2,587 high-quality single cells. Cells were assigned as malignant based on copy-number alteration (Figure S1B), graph-based clustering, and differential expression of canonical marker genes (Figure 1C). Analysis of mutant H3.3G34R/V expression further

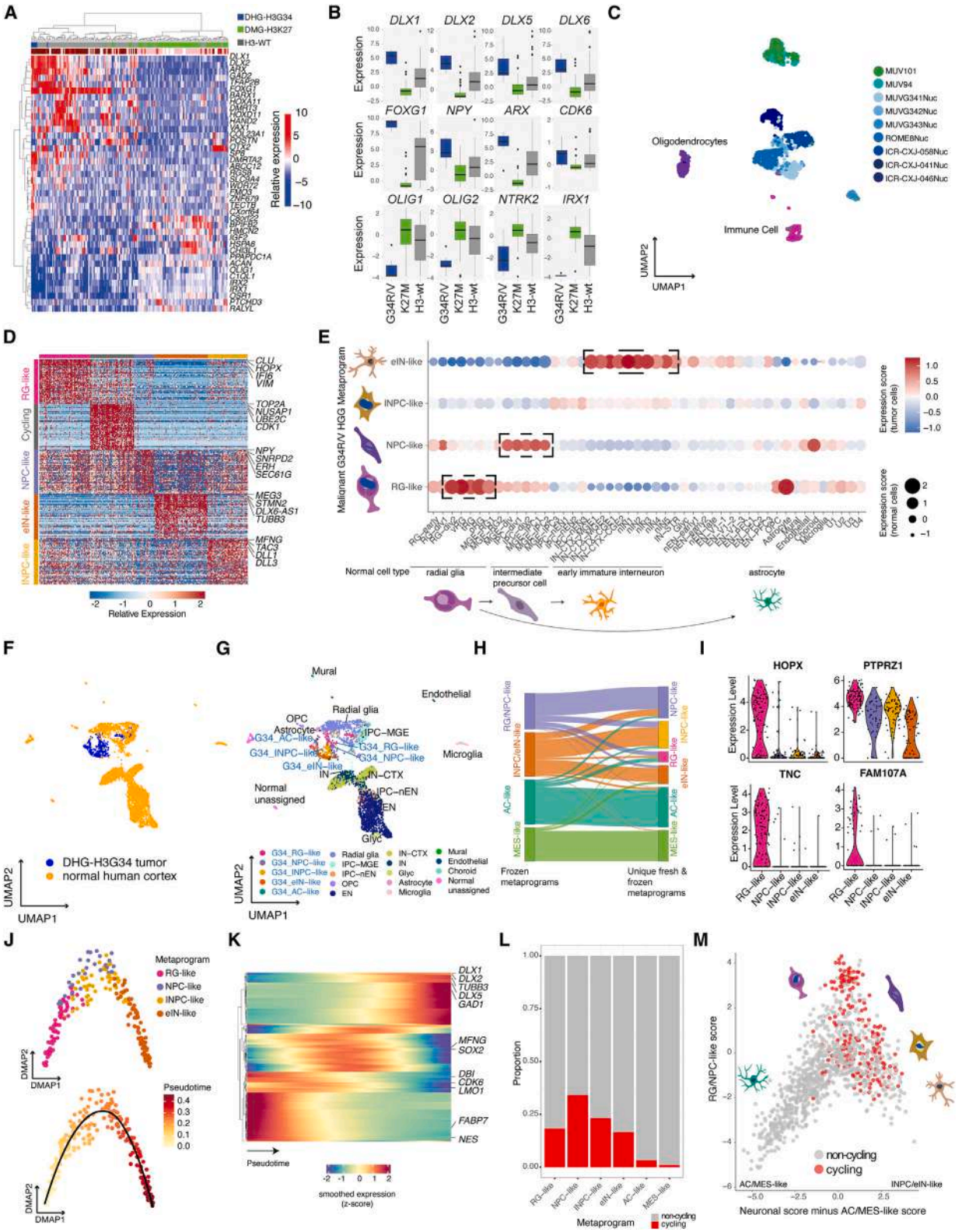

Figure 1. Developmental spectrum of interneuronal lineage tumor cells in DHG-H3G34

(A) Differentially expressed genes (rows) between DHG-H3G34 (blue), DMG-H3K27 (green), and H3-wild-type HGG (gray), in *n* = 191 pediatric patient HGG bulk RNA-seq profiles.

(legend continued on next page)

validated our malignancy annotations (Figure S1C). Within malignant cells, we identified five major metaprograms using orthogonal approaches of non-negative matrix factorization and graph-based clustering following data integration (Figures S1D and S1E; Table S2): cycling cells (e.g., *RRM2*, *NUSAP1*, and *TOP2A*), radial glia-like to neuronal progenitor-like cells (e.g., *NPY*, *FABP7*, *STMN1*, and *SOX2*; termed "RG/NPC-like"), interneuron progenitor to early GABAergic interneuron-like cells (e.g., *DLX1*,*2*,*5*,*6*, *GAD1*,*2*; termed "INPC/eIN-like"), as well as astrocyte-like (e.g., *AQP4*, *ID3*, and *AGT1*; termed "AC-like"), and mesenchymal cells (e.g., *ANXA1*, *CD44*, and *CLU*; termed "MES-like") (Figures S1D–S1G).

Independent analysis of freshly processed DHG-H3G34, MUV94, achieved even higher granularity in resolving varying maturity of interneuronal lineage cells by distinctly classifying RG/NPC-like cells into RG-like and NPC-like and INPC/eIN-like cells into INPC-like and eIN-like populations (Figures 1D–1H). This was further supported by the resemblance of these tumor cell populations to their normal counterparts in human cortex development (Figures 1E–1G). Notably, RG-like cells depicting similarity to normal radial glia, specifically expressed marker genes of outer radial glia, such as *HOPX*, *PTPRZ1*, *TNC*, and *FAM107A* (Figures 1E and 1I).[26,27] Specifically in human cortical development, outer radial glia cells have been described to rapidly expand during the second trimester and drive cortical neurogenesis.[28] We next sought to address the question whether these tumor cell populations are ordered along a defined developmental path by performing pseudotime analysis. This concordantly revealed a trajectory from undifferentiated RG-like cells via NPC-like cells (resembling intermediate precursor cells/IPCs), INPC-like cells (mapping between IPCs and early interneurons), toward eIN-like cells (resembling early interneurons) (Figures 1J, 1K, and S1H). Moreover, we validated our findings by mapping these tumor cell signatures to a longitudinal single-cell RNA-sequencing (scRNA-seq) dataset tracking mouse ganglionic eminence interneuron progenitor cell fates.[29] Indeed, this analogously revealed sequential expression of RG-like and NPC-like toward INPC-like and eIN-like gene signatures in normal ganglionic eminence progenitors along their differentiation trajectory *in vivo* (Figure S1I).

Asking which tumor cell state contributed most to tumor proliferation, we observed that progenitor and interneuronal lineage populations in DHG-H3G34 harbored higher proportions of actively cycling cells (16–34%) compared to AC-like and MES-like cells (<5%) (Figure 1L). Specifically, the highest cycling fractions were detected in NPC-like cells and decreased gradually along INPC-like to eIN-like cells (Figure 1L), underscoring their resemblance to a continuous interneuron developmental trajectory spanning rapidly dividing ganglionic eminence progenitors that self-renew or give rise to neuroblasts and early post-mitotic interneurons.[30,31]

We next compared cell state proportions between patient tumors and noted that progenitor and interneuronal lineage-like cells were ubiquitously expressed in all DHG-H3G34 tumors at varying proportions (Figure S1J). By contrast, higher variability was observed for AC/MES-like cell state proportions ranging from complete absence to high proportions in a subset of tumors (Figure S1J). Interestingly, and in contrast to all other HGG types,[8,15,32–34] DHG-H3G34 tumor cells did not resemble any oligodendroglial lineage, which is consistent with the previous finding that these tumors arise in cells of a neuronal and not an oligodendroglial lineage precursor.[19,20]

Finally, we projected our newly resolved cell states onto a published 10x 3′mRNA scRNA-seq dataset of 16 DHG-H3G34 patient tumors,[19] where unsupervised analysis had indicated the presence of neuronal and astroglial lineage cells alongside indeterminably segregated dysplastic cells. Integration with our Smart-Seq2 results suggested a more granular classification of these 10x scRNA-seq-derived cells (Figures S1K and S1L).

Conclusively, our data demonstrate that DHG-H3G34 harness transcriptional programs of various stages along interneuron lineage development. This suggests a putative cellular hierarchy in which less differentiated RG-like and NPC-like cells and more committed INPC-like and eIN-like cells constitute the self-renewing compartments, mirroring rapid expansion of the GABAergic interneuronal lineage during human telencephalic development,[30,35,36] while non-neuronal AC-like and MES-like cells are largely quiescent (Figure 1M).

Interneuronal lineage programs are preferentially expressed and epigenetically maintained in DHG-H3G34

We next aimed to understand if interneuronal gene programs are selectively expressed in DHG-H3G34 tumor cells compared to

(B) Boxplots of select differentially expressed genes. The thick line within the box represents the median, the lower and upper limits of the boxes first and third quartiles, the whiskers 1.5× the interquartile range. All comparisons DHG-H3G34 versus DMG-H3K27: p value <0.0001, save for *CDK6*, p value = 0.016, t test.
(C) Uniform manifold approximation and projection (UMAP) of 2,587 DHG-H3G34 glioma cells/nuclei profiled by single-cell (2 samples)/single-nucleus RNA-seq (7 samples).
(D) Relative expression of NMF metaprogram marker genes (rows) in whole-cell transcriptomes (columns) from fresh sample MUV94.
(E) Projection of fresh single-cell metaprograms (y axis) onto a single-cell atlas of the developing human cortex.[25] Color scale: scores of normal cell signatures in tumor cells. Dot sizes: scores of tumor cell signatures in normal cells.
(F and G) Joint UMAP of normal human cortex cells[25] and DHG-H3G34 fresh tumor cells after data integration. Cells are colored by (F) data source and (G) cell type as well as fresh/frozen tumor metaprograms.
(H) Sankey plot depicting distribution of single nuclei (columns), scored for either metaprograms derived from frozen tumors (left) or for all unique, granularly resolved metaprograms derived from fresh and frozen tumors (right).
(I) Log-normalized expressions (y axes) of outer radial glia marker genes across fresh single-cell metaprograms (x axes) in MUV94.
(J) Diffusion map of MUV94 single-cell transcriptomes colored by fresh metaprograms (left), and pseudotime analysis with cells colored by relative pseudotime (right).
(K) Z scored expressions (color scale) of temporally dynamic genes (rows) in MUV94 single cells ordered along pseudotime (columns).
(L) Proportion (y axis) of cycling vs. non-cycling (color-scale) single cells/nuclei in combined fresh and frozen metaprograms (x axis).
(M) 2D-representation of the stem-like RG/NPC-like scores (y axis) and neuronal (INPC/eIN-like) vs. AC/MES-like scores (x axis) for all single nuclei, colored by their cycling status.
See also Figure S1 and Tables S1 and S2.

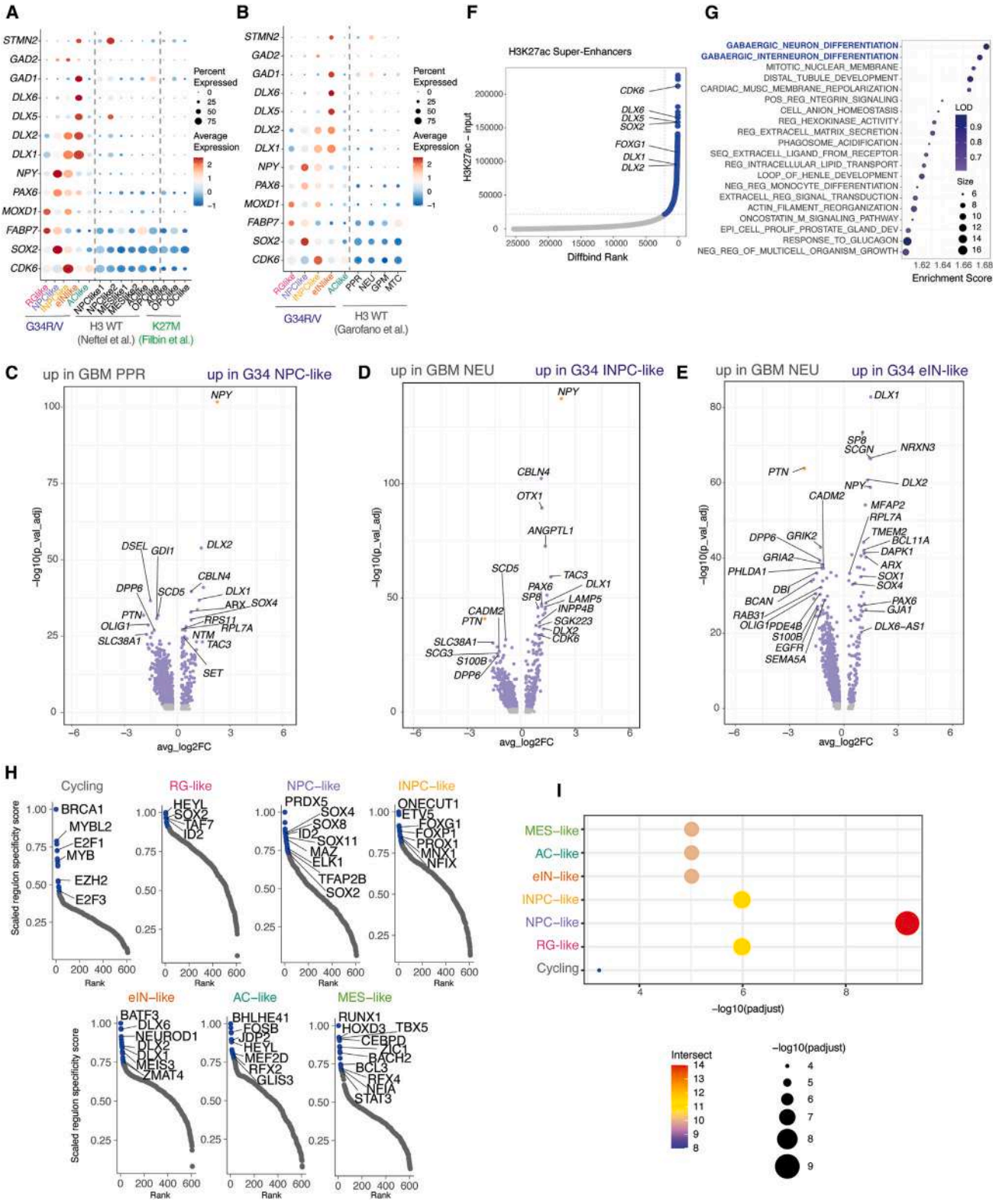

Figure 2. Interneuronal lineage programs are preferentially expressed and epigenetically maintained in DHG-H3G34

(A and B) Markers of interneuron lineage development/specification (y axis), compared for their expression across (A) DHG-H3G34, DMG-H3K27,[8] and H3-wild-type GBM[32] single-cell populations, and (B) DHG-H3G34 and H3-wild-type GBM pathway-based[37] single-cell populations (x axis). PPR: proliferative/progenitor,

(legend continued on next page)

other HGG types. As neuronal progenitor-like populations (GBM NPC-like–1&2) have been variably observed in IDH-wild-type/H3-wild-type glioblastoma (GBM),[32,37] we directly compared our DHG-H3G34 scRNA-seq data to GBM and DMG-H3K27 scRNA-seq datasets[8,32] of the same Smart-Seq2 protocol. Indeed, progenitor RG/NPC-like and early interneuronal INPC/eIN-like marker genes (e.g., *SOX2*, *CDK6*, *DLX1/2*, and *DCX*) were enriched in DHG-H3G34, even when only compared to GBM NPC-like-1 and 2 populations (Figure 2A). This held true when comparing DHG-H3G34 tumor cells to GBM cell states classified by pathway activities as progenitor/proliferative (PPR) or neuronal (NEU)[37,39,40] (Figure 2B), revealing that interneuronal progenitor markers and fate determinants like *ARX*, DLX TFs, and neuropeptide Y (*NPY*) were indeed upregulated in DHG-H3G34 NPC/INPC/eIN-like cells (Figures 2C–2E). Notably, NPY has been shown to stimulate neuronal progenitor proliferation and is almost exclusively expressed in the GABAergic interneuronal lineage.[41–43] By contrast, more mature neuronal and glutamatergic synaptic markers (e.g., *S100B*, *GRIA2*, and *GRIK2*) were more highly expressed in GBM NEU populations (Figures 2C–2E). Together, these results underline a distinct expression of GABAergic interneuron developmental states in DHG-H3G34 tumor cells, compared to other molecular glioma types.

To further dissect the epigenetic regulation of DHG-H3G34 tumor cell states, we performed chromatin immunoprecipitation sequencing (ChIP-seq) in patient-derived samples of various histone modifications (Figures 2F, 2G, and S2A–S2F). We observed general concordance between binding sites of mutant H3.3G34R/V and wild-type H3.3 (Figure S2A), with the majority of genes regulated by either heterogeneous nucleosomes or mutant H3.3G34R/V only (Figure S2B), in line with the heterozygous nature of the H3.3G34R/V mutation. To further discern epigenetic effects of mutant H3.3G34R/V, we transduced HEK293T cells with V5-tagged H3.3wt, H3.3G34R, or H3.3G34V, demonstrating a marked reduction of the activating H3K36me3 mark associated with mutant but not endogenous histone, pointing toward *cis* effects of the H3.3G34R mutation[19,44,45] (Figure S2C). Contrastingly, in patient-derived DHG-H3G34 cells, we detected higher proportions of H3K36me3 modifications in genomic loci marked by heterogeneous nucleosomes (Figure S2D). This suggests an additional *trans* effect of the H3.3G34R/V mutation increasing deposition of H3K36me3 at select genes, as previously indicated.[46] Next, super-enhancer analysis highlighted multiple interneuronal lineage precursor markers (e.g., *DLX1*,*2*,*5*,*6*, *SOX2*, and *CDK6*; Table S3) to be upregulated by activating epigenetic marks and super-enhancers in a concerted manner (Figures 2F, 2G, and S2E–S2I). Leveraging our Smart-Seq2 data, we further aimed to understand how each DHG-H3G34 cellular state is epigenetically regulated and reconstructed networks of TFs and their gene targets/regulons (Figure 2H; Table S4). This indicated that RG-like and NPC-like cells are governed by stemness-associated SOX TF family members (e.g., SOX2, SOX4, and SOX11). Top regulators of INPC-like cells included ONECUT1 and ETV5, which have been implicated in normal interneuron differentiation,[47,48] while eIN-like cells were governed by determinators more specific to GABAergic interneurons including the DLX TF family, NEUROD1 and MEIS3. We then asked to what extent cell state-specific regulons may be activated by DHG-H3G34 super-enhancers and overlaid our single-cell results with ChIP-seq-derived super-enhancer profiles. This revealed that the majority of DHG-H3G34 super-enhancers specifically govern the interneuronal progenitor populations as opposed to purely cycling, eIN-like, AC-like, and MES-like cell populations (Figure 2I), further underscoring epigenetic maintenance of stemness and interneuron progenitor signatures in DHG-H3G34.

Comparing super-enhancer profiles between DHG-H3G34 and DMG-H3K27, we likewise observed that interneuronal lineage progenitor markers were among the genes most differentially upregulated by super-enhancers in DHG-H3G34 (Figure S2J). Conversely, the repressive H3K27me3 mark was relatively depleted for these genes in DHG-H3G34 compared to DMG-H3K27 (Figure S2K).

We next asked whether the increase of interneuronal lineage progenitor signatures presents a direct effect of the H3.3G34R/V-mutation or rather a reflection of the putative cell of origin. Therefore, we integrated our scRNA-seq-derived tumor metaprograms with published bulk RNA-seq data of human embryonic forebrain neural stem cells, genetically engineered to express the H3.3G34R-mutant or H3.3-wild-type histone with *TP53* and *PDGFRA* co-alterations.[20] This revealed a downregulation of more mature neuronal INPC-like and eIN-like signatures in *PDGFRA*alt-*TP53*alt-*H3.3G34R*-mutant compared to *PDGFRA*alt-*TP53*alt-*H3.3*-wild-type neural stem cells. Conversely, undifferentiated RG-like and NPC-like signatures, along with glia-like metaprograms were upregulated in *PDGFRA*alt-*TP53*alt-*H3.3G34R*-mutant cells (Figure S2L). This, in line with previous findings,[19,20] suggests that the H3.3G34R/V-mutation does not

NEU: neuronal, GPM: glycolytic/plurimetabolic, MTC: mitochondrial. Dot size: percentage of cells expressing the gene in the given population. Color scale: scaled average relative expression.

(C–E) Volcano plots depicting differentially expressed genes with -log10 of the BH-adjusted Wilcoxon rank-sum test-derived *p* value (y axis) plotted against log2 fold change (x axis) in DHG-H3G34 NPC-like vs. GBM PPR cells (C), DHG-H3G34 INPC-like vs. GBM NEU cells (D), and DHG-H3G34 eIN-like vs. GBM NEU cells (E).

(F) Input-normalized, rank-ordered H3K27ac signals (x axis) against H3K27ac occupancy (y axis) in DHG-H3G34. Super-enhancer-associated genes are colored blue.

(G) Gene ontology analysis of DHG-H3G34 super-enhancer-associated genes, plotted as dots according to their enrichment score (x axis), scaled by the number of genes in the annotated ontology.

(H) Ranked cell state-specific TF regulatory networks (regulon, x axis) derived from 7 frozen tumors by SCENIC,[38] plotted against their normalized specificity score (y axis).

(I) Overrepresentation analysis of SCENIC-derived cell state-specific TF regulons (x axis), overlayed with H3K27ac ChIP-seq-derived super-enhancers. Dot size: -log10 of FDR-adjusted *p* values calculated using a Fisher's exact test. Color scale: number of intersecting genes.

See also Figure S2 and Tables S3 and S4.

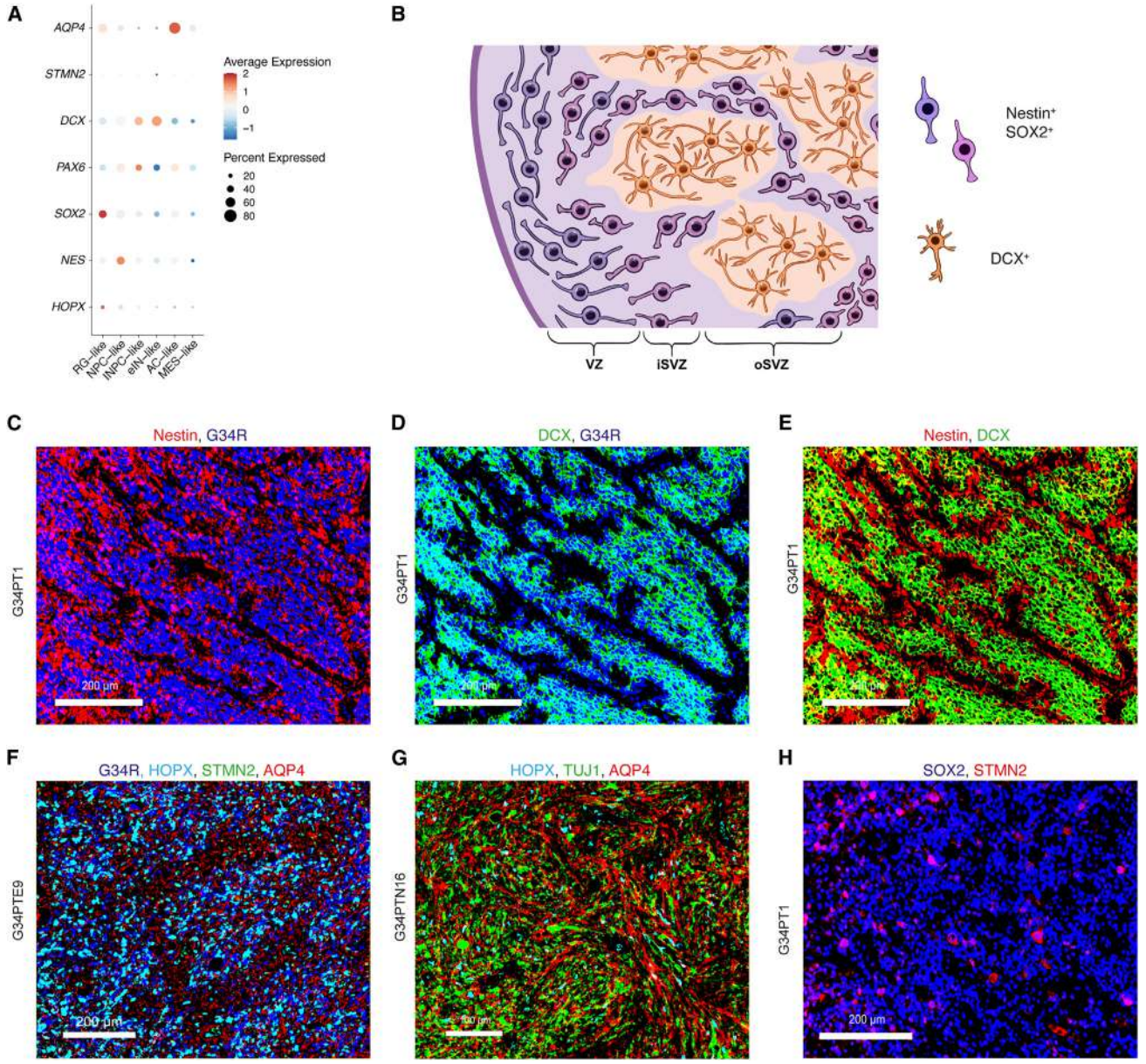

Figure 3. *In situ* validations of scRNA-seq derived DHG-H3G34 interneuronal lineage programs

(A) Markers of RG/NPC-like, INPC/eIN-like and AC-like DHG-H3G34 tumor cell populations used for immunofluorescence (IF) validations. Dot sizes: percentage of cells expressing the gene in the given cluster. Color scale: scaled average relative expression.

(B) Schematic of nests of DCX$^+$ neuroblasts surrounded by different Nestin$^+$ SOX2$^+$ progenitor cells detected in human developing MGE during 2nd trimester, as described by Paredes et al., 2022.[35] i/oSVZ: inner/outer subventricular zone.

(C–E) Nest-like structures of DCX$^+$ (green) G34R$^+$ (blue) tumor cells, surrounded by Nestin$^+$ (red) G34R$^+$ tumor cells in patient DHG-H3G34 G34PT1. Scales: 200 μm.

(F) IF representation of HOPX$^+$ RG/NPC-like tumor (G34R+) cells, along STMN2$^+$ INPC/eIN-like tumor cells and AQP4$^+$ AC-like tumor cells in patient DHG-H3G34 G34PTE9. Scale: 200 μm.

(G) IF of HOPX$^+$ RG/NPC-like tumor (G34R$^+$) cells, along TUJ1$^+$ INPC/eIN-like tumor cells and AQP4$^+$ AC-like tumor cells in patient DHG-H3G34 G34PTN16. Scale: 100 μm.

(H) IF of SOX2$^+$ RG/NPC-like tumor cells alongside rare STMN2$^+$ INPC/eIN-like cell populations in patient DHG-H3G34 G34PT1. Scale: 200 μm.

See also Figure S3 and Table S5.

directly induce the interneuronal lineage of origin per se but rather reinforces already existing progenitor cell states, thereby potentially hampering differentiation of these lineage precursors.

Collectively, we demonstrate that interneuronal lineage progenitor signatures are distinctly upregulated in DHG-H3G34 compared to other HGG types.

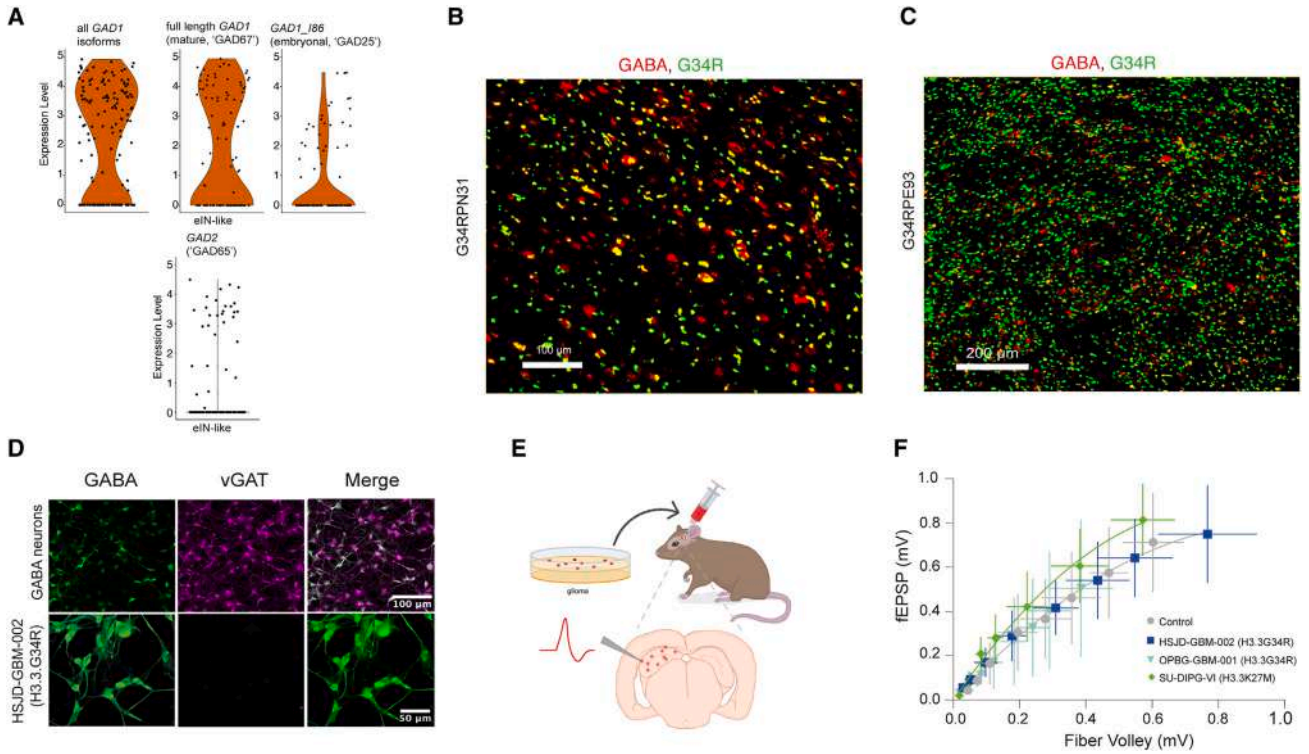

Figure 4. DHG-H3G34 display features of GABAergic interneuron development and exert neuron-glioma interactions distinct from other HGG types

(A) Log-normalized expression levels of *GAD1* splice isoforms (top middle and right) and *GAD2* transcripts (bottom) in fresh DHG-H3G34 eIN-like cells.
(B and C) IF showing GABA$^+$ (red) malignant cells (G34R$^+$) in two patient DHG-H3G34, G34RPN31 (B) and G34RPE93 (C), scales: 100 μm (B) and 200 μm (C).
(D) IF of GABA (green) and VGAT (purple) in HSJD-GBM-002 (H3.3G34R) and normal GABA neuron controls. Scales: 100 μm (top), 50 μm (bottom).
(E) Schematic of experimental design for panel (F).
(F) Neuronal hyperexcitability in patient-derived DMG-H3K27 (SU-DIPGVI, green) but not in two DHG-H3G34 (HSJD-GBM-002, dark blue; OPBG-GBM-001, light blue) xenografts in the mouse hippocampus. Plot of presynaptic fiber volley versus amplitude of fEPSP at increasing axonal stimulation intensities (10, 20, 30, 50, 75, 100, 150, and 200 μA) in glioma-bearing or needlestick control hippocampus (needlestick control: $n = 8$ slices from 4 mice; HSJD-GBM-002: $n = 9$ slices from 4 mice; OPBG-GBM-001: $n = 7$ slices from 3 mice; SU-DIPGVI: $n = 7$ slices from 3 mice at each data point). Data fit to a nonlinear regression and compared to needlestick by extra-sum-of-squares F-test (p values for HSJD-GBM-002: 0.0727; OPBG-GBM-001: 0.77; SU-DIPGVI: 0.0001). Data are mean ± SEM.
See also Figure S4.

DHG-H3G34 recapitulate spatial and phenotypic features of early GABAergic interneuron development

We next aimed at spatially validating the scRNA-seq tumor cell populations in 6 additional patient DHG-H3G34 tumors using multiple panels of scRNA-seq-derived cell state-characteristic markers for co-staining by immunofluorescence (IF) (Figure 3A; Table S5. We confirmed that all cell populations were discernable at the protein level. Furthermore, cells were not distributed randomly but tended to form spatially distinct structures (Figures 3B–3H and S3A–S3C). This was particularly notable for RG/NPC-like and INPC/eIN-like cells, which formed patterns of nest-like structures densely consisting of DCX$^+$ INPC/eIN-like cells that were surrounded by Nestin$^+$ RG/NPC-like cells in a subset (3 out of 6) of tumors (Figures 3B–3E, S3B, and S3C). Intriguingly, these nest-like structures were reminiscent of DCX$^+$ neuroblast nests recently described in human second trimester ganglionic eminence and shown to sustain GABAergic interneuron production during development (Figure 3B).[35]

This *in situ* spatial resemblance to developmental neuroblasts was consistent with our scRNA-seq based observation that a fraction of more differentiated tumor eIN-like cells were still mitotic and likely had not yet reached full maturity. Hence, we aimed to characterize the degree to which interneuron-like DHG-H3G34 tumor cells may differentiate and resemble mature GABAergic interneurons. First, we performed integrated analysis of DHG-H3G34 tumor cells with normal human embryonal cortical cells.[25] Here, we observed that all DHG-H3G34 cell populations clustered closely with normal radial glia and IPCs, hinting at potentially conserved stemness/progenitor features across all tumor cells extending to more mature eIN-like cells (Figures 1F and 1G). Second, we quantified splice isoform expression of the GABA-synthesis enzyme encoding gene, *GAD1*, observing that in addition to the mature *GAD1* transcript variant (encoding "GAD67"), a subset of eIN-like cells also expressed a transitional immature/embryonal *GAD1* isoform (encoding "GAD25") (Figure 4A). Conversely, *GAD2* encoding for the GAD65 isoform, which only becomes upregulated later in development,[49] was only lowly expressed in the majority of eIN-like tumor cells (Figure 4A). At the protein level, we confirmed that a fraction of H3.3G34R-positive tumor cells

contained GABA in DHG-H3G34 patient tissues (Figures 4B and 4C). Conversely, comparative staining of GABA in DMG-H3K27 and GBM patient tissues was negative (Figures S4A–S4C). To further assess whether DHG-H3G34 eIN-like cells may be capable of vesicular GABA release, we performed IF against the vesicular GABA transporter VGAT in patient-derived DHG-H3G34 tumor cells. While these were positive for intracellular GABA, they lacked expression of the VGAT transporter protein, which only becomes upregulated upon differentiation to more functionally mature GABAergic interneurons (Figures 4D and S4D).[50] Together, this suggests that DHG-H3G34 eIN-like cells are not capable of differentiating to mature functional interneuron-like cells, underscoring a developmental arrest in immature interneuron progenitor-like states.

DHG-H3G34 exert neuron-glioma interactions distinct from other HGG types

In light of the pronounced expression of interneuronal lineage states in DHG-H3G34, we hypothesized that this may engender functional consequences and vulnerabilities distinct from other glioma types. It has been previously shown that different glioma types of predominantly glial lineage, such as IDH-/H3-wild-type GBM/HGG and DMG-H3K27, induce neuronal hyperexcitability in normal neurons and around them[51–54] and engage in neuronal activity-regulated paracrine signaling[55–57] and glutamatergic neuron-to-glioma synaptic signaling to promote tumor growth.[54,58,59] We, therefore, compared the expression of synaptic signaling and neuronal activity-associated marker genes in our pan-glioma bulk and scRNA-seq datasets. Interestingly, we observed genes related to glutamatergic and calcium signaling to be broadly downregulated in DHG-H3G34 compared to DMG-H3K27 and GBM (Figure S4E). We next examined the effects of DHG-H3G34 tumor cells on neuronal hyperexcitability *in vivo* by measuring field excitatory postsynaptic potentials (fEPSPs) in acute hippocampal xenograft slices from two patient-derived DHG-H3G34 tumor cell lines xenografted into the hippocampus of immunocompromized NSG mice (Figures 4E and 4F). No differences were observed in measured fEPSPs of DHG-H3G34 engrafted hippocampus compared to a needlestick control, suggesting that DHG-H3G34 do not induce neuronal hyperexcitability. By contrast, neuronal hyperexcitability was detected in DMG-H3K27 hippocampal xenografts as expected[54] (Figure 4F). In both DHG-H3G34 and DMG-H3K27 xenografts, we observed adequate tumor cell infiltration into the hippocampus (Figure S4F). Last, we performed co-cultures of DHG-H3G34 cells with normal murine neurons, which led to a remarkable increase in glioma cell proliferation, comparable to effects seen for DMG-H3K27 cells (Figure S4G). In DMG-H3K27 and other glioma types, tumor cell proliferation has been shown to be incited via neuronal activity-dependent secretion of BDNF and NLGN3.[55–57] Thus, we tested the effects of BDNF and NLGN3 added to cultures of DHG-H3G34 cells but contrastingly did not see increased tumor cell proliferation (Figure S4H), which again points toward distinct modes of neuron-glioma crosstalk in DHG-H3G34.

Collectively, our data suggest that DHG-H3G34 cells uniquely emulate transcriptional signatures and spatial structures described in normal human embryonal interneuron development. Given their distinct expression of these interneuronal gene signatures, DHG-H3G34 may exert fundamentally different microenvironmental interactions than those that have been described for glioma types of predominantly glial lineage.

Progenitor-like states along interneuronal lineage development present a distinct vulnerability in DHG-H3G34

We next asked if the interneuronal developmental lineage characterizing DHG-H3G34 biology confers selective vulnerabilities that may lead to currently lacking targeted therapies. To investigate this question in an unbiased manner, we performed genome-wide CRISPR-Cas9 screens in two DHG-H3G34 cell models (Figures 5A, S5A, and S5B; Table S6). Gene dependencies described as common essentials were corrected for in both cell lines[60,61](Figure S5A). We projected top gene dependencies from both CRISPR-Cas9 screens onto our patient DHG-H3G34 scRNA-seq dataset, and observed that most hits were enriched in progenitor-like cells along interneuronal lineage development (Figure 5B). Contrastingly, almost no gene hits mapped to AC-like/MES-like cell programs, suggesting that DHG-H3G34 are mostly dependent on gene signatures that are part of interneuronal developmental states. Specifically, *SOX2* and *CDK6* emerged as top significant hits in both screens based on ranked gene-effect scores (Figures 5C, 5D, and S5B). Strikingly, these dependencies were highly selective in DHG-H3G34 cells compared to a panel of 769 pan-cancer cell lines assessed as part of the DepMap consortium (Figure 5C).

Next, we validated top CRISPR-Cas9 screen gene dependencies that were enriched in interneuronal developmental states in three DHG-H3G34 models by CRISPR-Cas9 single-gene knockouts. We observed a significant decrease of cell viability across all three cell lines upon knockout of *SOX2*, *FOXG1*, *DLX1*,*2*,*5*, and *6* (Figures 5E and S5C–S5F). *In vivo* validations of lineage dependencies via CRISPR-Cas9 mediated knockout in a patient-derived xenograft (PDX) model further resulted in delayed tumor growth and prolonged overall survival (Figures 5F and 5G). The effect was strongest after knockout of *SOX2*, an RG/NPC-like cell marker, which led to a complete abrogation of tumor growth, compared with knockout of markers of more differentiated INPC/eIN-like cells (*DLX2* and *DLX5*) (Figures 5F and 5G). This finding is in line with our proposed developmental model, suggesting that most immature RG/NPC-like cells represent the principal tumor-propagating cellular compartment.

Taken together, we demonstrate that genes enriched in early states of interneuronal lineage development are essential for DHG-H3G34 tumor growth *in vitro* and *in vivo*.

Efficacy of CDK4/6 targeting in DHG-H3G34

To move our findings toward more immediate clinical translatability, we next aimed at validating top targets for which FDA-approved drugs were already available. We focused on *CDK6*, a top gene dependency (Figures 5C, 5D, and 5H) and one of the most specific targets for DHG-H3G34 compared to >700 pan-cancer cell lines (Figure 5C). *CDK6* also presented a DHG-H3G34-selective vulnerability compared to 108 other molecular HGG in an oncology-focused CRISPR-Cas9 screen[62] (Figure S5G). This was contrasted by *CDK4*, which presented a broad gene hit across cancer and glioma types, hinting at its more pan-cancer-essential role (Figures 5C and S5G). Moreover,

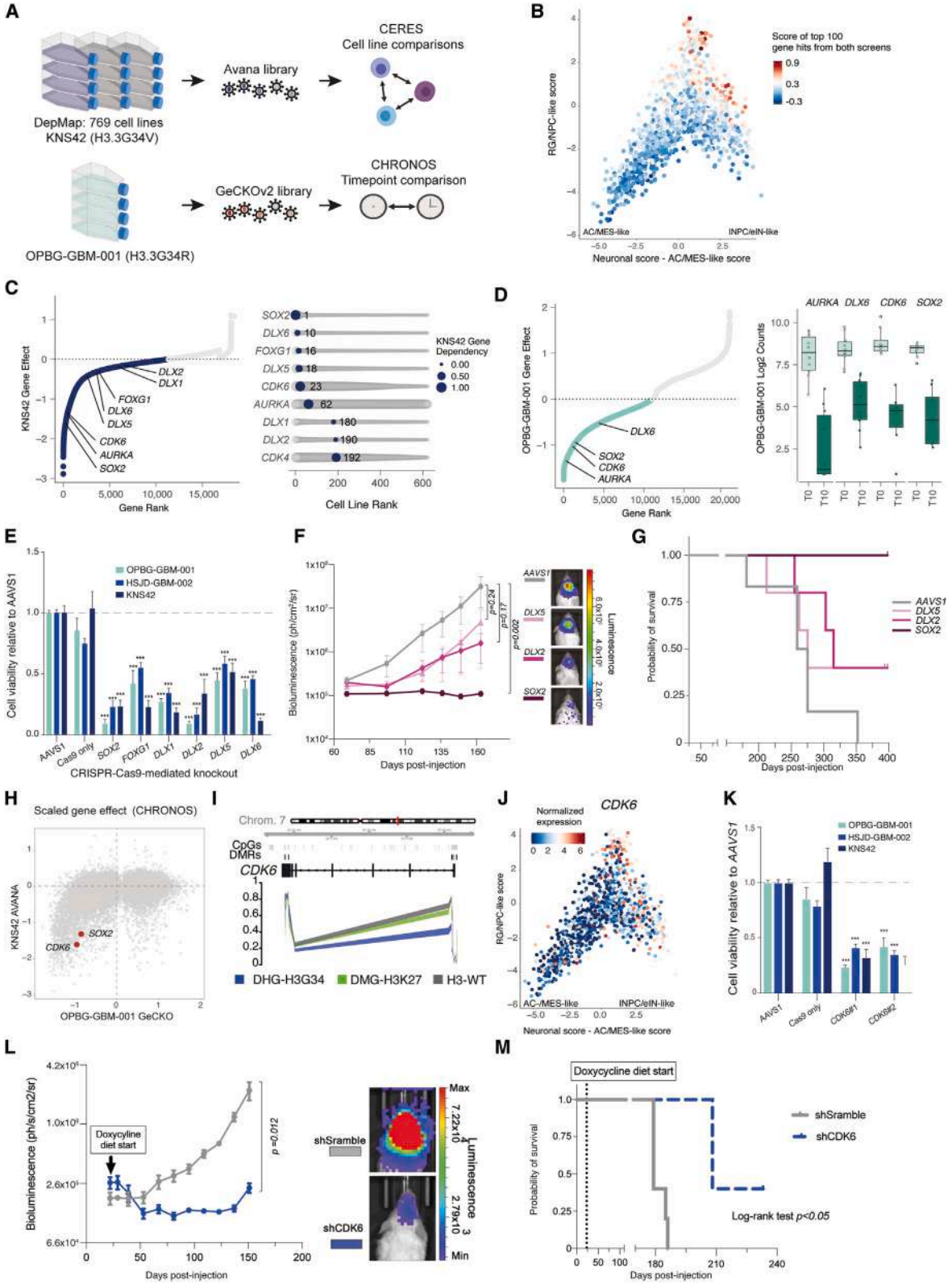

(legend on next page)

CDK6 was epigenetically upregulated by activating chromatin modifications (Figures 2B and S5H) and via DNA hypomethylation at its core promoter/transcription start site (TSS) specifically in DHG-H3G34 but not in DMG-H3K27 and H3-wild-type HGG (Figure 5I), leading to its high expression in cycling and non-cycling interneuronal lineage precursor populations (Figures 2A, 2B, 5J, and S5I). Notably, analysis of published transcriptomic data of DHG-H3G34 cell line HSJD-GBM-002, wherein the H3.3G34R-mutation was corrected by CRISPR-Cas9 editing,[20] revealed a significant downregulation of *CDK6* in H3.3-corrected compared to H3.3G34R-mutant tumor cells (Figure S5K). Contrastingly, differential DNA hypomethylation was not seen at the promoter/TSS locus of *CDK4* in DHG-H3G34 (Figure S5J) nor did correction of the H3.3G34R/V-mutation result in changes of *CDK4* expression (Figure S5K), further pointing toward a less specific role of CDK4 as opposed to CDK6 in DHG-H3G34.

We validated the effects of CDK6 depletion in DHG-H3G34 by CRISPR-Cas9 knockouts *in vitro*, leading to a significant decrease of viability across various DHG-H3G34 cell lines (Figures 5K and S5L). Furthermore, we performed *in vivo* validations of CDK6 depletion using two approaches: Firstly, by xenografting BT690 DHG-H3G34 tumor cells after *CDK6* knockout into mice (Figure S5M) and secondly, by inducing shRNA-mediated knockdown of *CDK6* after the formation of tumors in BT690 xenografts (Figure S5N). Both approaches significantly decreased tumor growth and enhanced overall survival (Figures 5L, 5M, S5O, and S5P).

Next, we assessed a range of CDK4/6-inhibitors and a CDK6-specific degrader BSJ-03-123 in multiple patient-derived HGG cell lines (Figures 6A, 6B, and S6A–S6C), observing sensitivity to different CDK4/6-inhibitors in four out of five DHG-H3G34 models (Figures 6A and 6B), which in KNS42 was diminished upon CRISPR-Cas9-mediated correction of the H3.3G34V-mutation (Figure S6B). Among CDK4/6-inhibitors, ribociclib has been shown to act most specifically on CDK4 and CDK6, whereas palbociclib and especially abemaciclib target additional kinases including GSK3, CDK7, and CAMKIIB.[63] Notably, when comparing effects of these different inhibitors in HGG cell lines, enhanced responsiveness to more CDK4/6-specifiic inhibitor ribociclib and a CDK6-specific PROTAC degrader was seen in DHG-H3G34 cells compared to a panel of DMG-H3K27, H3-wild-type/IDH-wild-type GBM cell lines, as well as an immortalized human astrocyte (NHA) and mouse OPC cell line (Figures 6A and 6B). By contrast, we observed broad sensitivity to less specific CDK4/6-inhibitors abemaciclib and palbociclib particularly across GBM cells (Figures 6A and 6B). To next examine potential genetic and non-genetic biomarkers of ribociclib efficacy, we characterized the different patient-derived cell models by exome- and RNA-sequencing. We did not detect a link between response to ribociclib and *CDKN2A/B* loss or *CDK4/6* amplification (Figure S6C). However, we observed significantly increased *CDK6* expression in ribociclib sensitive compared to non-sensitive cell lines (Figure 6C).

Together, these findings indicate that DHG-H3G34 display enhanced vulnerability to more specific CDK4/6- and particularly CDK6-targeting. This sensitivity is primarily conferred via non-genetic mechanisms upregulating *CDK6* expression, mediated by epigenetic effects of the H3.3G34R/V-mutation and the interneuronal lineage origin of DHG-H3G34.

We next aimed to investigate the mechanisms by which CDK6 inhibition targets the interneuronal developmental lineage in DHG-H3G34. A dose-dependent G1-phase cell-cycle arrest following CDK6 degradation was observed (Figures 6D and S6D), in line with cytostatic effects of CDK6 targeting. Of note, regulation of G1/S-length by CDK4/6 has been implicated in normal neuronal precursor amplification, where CDK4/6 ablation

Figure 5. Progenitor-like states along interneuronal lineage development present a distinct vulnerability in DHG-H3G34

(A) Schematic of the genome-wide CRISPR-Cas9 screen protocols.

(B) Top 100 gene dependencies from both CRISPR-Cas9 screens scored for their expression (color scale) in snRNA-seq data, plotted as 2D-representation of RG/NPC-like scores (y axis) and INPC/eIN-like vs. AC/MES-like scores (x axis).

(C) Left: Ranked gene effect for the KNS42 screen. Blue points indicate genes with dependency scores <0. Right: Ranked gene dependencies for the DepMap CRISPR-Cas9 screening panel of pan-cancer cell lines. Blue point indicates the ranked position of KNS42.

(D) Left: Ranked gene effect for the OPBG-GBM-001 screen. Turquoise points indicate genes with dependency scores <0. Right: Log2 read counts of multiple gRNAs targeting each gene at the beginning (T0) and after 10 cell doublings (T10). The thick line within the boxplot represents the median, the lower and upper box limits the first and third quartiles, the whiskers the 1.5× IQR.

(E) Cell viability after CRISPR-Cas9-directed single-gene knockouts compared to *AAVS1* negative gRNA control in 3 DHG-H3G34 cell lines. ***p values <0.001 for all targets relative to *AAVS1* negative control by unpaired two-sided t test. Data shown as mean ± SEM.

(F) Bioluminescent (BLI) signal quantification of animals orthotopically xenografted with HSJD-GBM-002 cells following CRISPR-Cas9-mediated single-gene knockouts (n = 6 animals per group), shown as mean ± SEM. p values derived from a two-sided unpaired Student's t test. Representative BLI images from each group are shown on the right.

(G) Kaplan-Meier analysis of mice harboring HSJD-GBM-002 DHG-H3G34 tumors with CRISPR-Cas9-mediated single-gene knockouts vs. *AAVS1* safe-harbor locus control (n = 6 animals per group). p values derived from log rank test compared with *AAVS1* control animals: for *SOX2*: 0.0014; *DLX2*: 0.11; *DLX5*: 0.24.

(H) Scaled gene effect calculated by CHRONOS for the genome-scale CRISPR-Cas9 screens in OPBG-GBM-001 (x axis) vs. KNS42 (y axis).

(I) Methylation beta values plotted as ribbons across the *CDK6* genomic locus, with samples separated by H3.3-mutation status (color legend). Ribbon size: degree of variation across samples.

(J) Log-normalized expression of *CDK6* in DHG-H3G34 single-nucleus transcriptomes, plotted as 2D-representation of RG/NPC-like score (y axis) and INPC/eIN-like vs. AC/MES-like scores (x axis).

(K) Relative cell viability of DHG-H3G34 cells after CRISPR-Cas9 knockout of *CDK6* using two different sgRNAs, compared to *AAVS1* negative gRNA control (***p-value <0.001, unpaired two-sided t test). Data shown as mean ± SEM.

(L) BLI quantification of animals with orthotopic BT690 DHG-H3G34 tumors, followed by shRNA doxycycline-inducible knockdown of *CDK6* compared to scramble shRNA (n = 5 animals per group), shown as mean ± SEM. p values calculated by two-sided unpaired Student's t test.

(M) Kaplan-Meier analysis of mice from (L), with shRNA doxycycline-inducible knockdown of *CDK6* after tumor formation compared to shRNA Scramble control (n = 5 animals per group). p value <0.05, log rank test.

See also Figure S5 and Table S6.

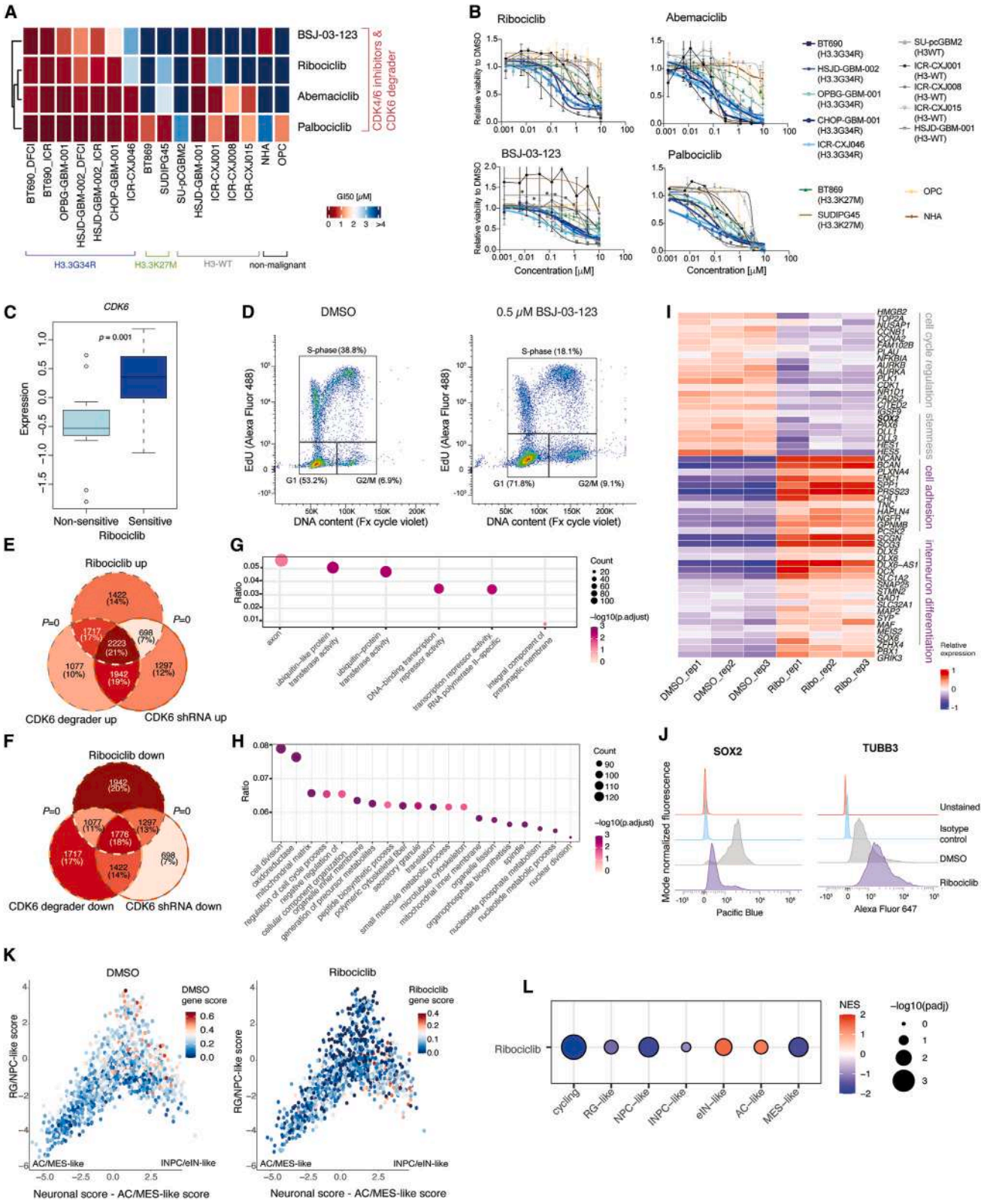

Figure 6. Enhanced efficacy of CDK4/6 pharmacological inhibition in DHG-H3G34

(A) Heatmap of GI 50 values (μM) assessed for CDK4/6-inhibitors (ribociclib, abemaciclib, and palbociclib) and CDK6 degrader (BSJ-03-123) at day 14 following 4 doses across DHG-H3G34 (BT690 [assessed independently at DFCI and ICR, plotted separately], OPBG-GBM-001, HSJD-GBM-002 [assessed independently

(legend continued on next page)

results in neuronal differentiation.[64–66] To interrogate gene signature changes in an unbiased manner, we performed RNA-seq following CDK6 degradation, CDK6 knockdown, and ribociclib treatment. Across all three conditions, we observed a notable overlap of downstream transcriptional effects (Figures 6E, 6F, and S6E). While downregulated genes were associated with proliferation and translation, commonly upregulated genes were enriched for pathways related to ubiquitination, transcription repression as well as axonal and presynaptic structures (Figures 6G and 6H). In ribociclib particularly, we detected upregulation of genes associated with synapse organization and interneuron specification (e.g., *DCX*, *STMN2*), cell adhesion and secretion (e.g., *NCAN*, *PLXN4A*, and *SCGN*), while progenitor-like markers (e.g., *SOX2* and *PAX6*) were decreased (Figure 6I). The decrease of progenitor-like marker SOX2 and increase of more mature interneuronal markers STMN2 and TUBB3 upon ribociclib treatment were validated at the protein level (Figures 6J and S6F). Next, we projected genes up- and downregulated following ribociclib treatment onto our patient scRNA-seq dataset, and indeed found that downregulated genes ("DMSO gene score") were enriched in the progenitor RG/NPC-like cells, while upregulated genes ("ribociclib gene score") were more strongly expressed in more differentiated eIN-like cells (Figure 6K). Concordantly, an enrichment for eIN-like signatures and to a lesser extent AC-like cells, as well as decrease of progenitor RG-like and NPC-like signatures were seen by gene set enrichment analysis (Figure 6L). Collectively, these findings suggest that CDK4/6-targeting induces a shift from undifferentiated, proliferating progenitor-like states toward more differentiated neuronal signatures.

Efficacy of CDK4/6 pharmacological inhibition in DHG-H3G34 *in vivo and in a patient*

To assess CDK4/6-inhibitor efficacy *in vivo*, we first evaluated blood-brain-barrier (BBB) penetrance and tolerability for ribociclib (200 mg/kg/day) or abemaciclib (100-150 mg/kg/day). Both drugs demonstrated sufficient BBB penetrance (Figures S7A and S7B), consistent with previous reports.[67–69] However, abemaciclib was less well tolerated than ribociclib requiring a dose reduction to 75 mg/kg/day (Figures S7C and S7D). We first treated DHG-H3G34 orthotopic PDX models with abemaciclib, and whilst tumor burden decreased significantly (Figures 7A and 7B), overall survival did not significantly improve. Since our data, in agreement with previous studies, indicated (i) more favorable BBB penetrance, (ii) higher unbound drug concentrations,[69,70] (iii) a higher specificity for CDK6-targeting, and (iv) better tolerability for ribociclib over abemaciclib, we next focused on treating DHG-H3G34 PDX with ribociclib, which led to a pronounced decrease of tumor burden and significantly improved overall survival (Figures 7C, 7D, S7E, and S7F). Notably, IF of treated PDX brains revealed upregulation of early interneuronal marker DCX after ribociclib (Figures 7E and 7F), validating our *in vitro* findings (Figures 6I–6L). Concordantly, we observed downregulation of progenitor-like marker Nestin at the tumor rim following ribociclib (Figures 7E and 7F).

Finally, we present initial clinical evidence of ribociclib treatment in a DHG-H3G34 patient (Figures 7G and 7H). A ten-year-old girl presented with headaches, vomiting, and photophobia. Head/spine magnetic resonance imaging (MRI) revealed a left frontal solid-cystic contrast-enhancing lesion which was completely resected (Figures 7G and 7H). Histology was consistent with a grade 4 HGG (Figures S7G–S7J), and molecular analysis revealed the presence of an *H3-3A*_G34R as well as *ATRX*_1514* mutation, and a methylation profile consistent with DHG-H34G34. Adjuvant treatment comprised radiotherapy plus concomitant and 12 subsequent cycles of temozolomide, leading to an initial complete remission. 13 months later, a routine MRI showed tumor recurrence with sulcal leptomeningeal enhancement, which was deemed not resectable (Figure 7H). Second-line chemotherapy with PCV (procarbazine, CCNU, and vincristine) was initiated, however, disease progression was seen after two cycles (Figures 7G and 7H).

Based on our pre-clinical evidence, third-line treatment with ribociclib on a compassionate use basis was started, and gradually increased to the recommended phase 2 dose (RP2D, i.e., 350 mg/m^2/day 3 weeks-on/1 week-off).[71] Due to an uncomplicated neutropenia grade 4, the dose was decreased to 280 mg/m^2/day after 2 cycles. No further dose reductions were needed

at DFCI and ICR, plotted separately], CHOP-GBM-001, and ICR-CXJ046), DMG-H3K27 (BT869, SUDIPG45), H3-wild-type HGG (SU-pcGBM2, HSJD-GBM-001, ICR-CXJ001, ICR-CXJ008, and ICR-CXJ015) cell lines, non-malignant human astrocytes (NHA) and mice OPCs (columns). GI 50 values were inferred for each cell line and drug from at least two biological replicates.

(B) Relative viabilities of DHG-H3G34, DMG-H3K27, H3-wild-type HGG cell lines, non-malignant human astrocytes (NHA), and mice OPCs, at day 14 following 4 doses of treatment compared to DMSO control, shown as mean ± SEM of at least two biological replicates per cell line and drug.

(C) Boxplot representation of *CDK6* expression across 5 ribociclib sensitive vs. 6 non-sensitive cell lines. *p* value was calculated using a Wald-test and BH-adjusted for multiple testing by DESeq2. The thick line within the box represents the median, the lower and upper limits the first and third quartiles, the whiskers 1.5× the interquartile range.

(D) Representative gating strategy for cell cycle analysis in OPBG-GBM-001 following treatment with 0.5 μM BSJ-03-123 or DMSO.

(E and F) Venn diagrams of commonly upregulated (E) and downregulated (F) genes between ribociclib, CDK6 degrader BSJ-03-123, and shRNA-mediated *CDK6* knockdown. *p* values calculated by Fisher's exact test.

(G and H) Gene ontology analyses of (G) upregulated and (H) downregulated genes shared between ribociclib, CDK6 degradation, and *CDK6* shRNA knockdown. Color scale: -log10 FDR/adjusted *p* values, size: number of genes within the respective GO term.

(I) Relative expression of select cell cycle, stemness, adhesion, and interneuron differentiation-associated marker genes down- or upregulated following 14 days of ribociclib compared to DMSO treatment in HSJD-GBM-002.

(J) Histogram of flow cytometry analysis in BT690 DHG-H3G34 line treated with 1 μM ribociclib over 10 days for SOX2$^+$ (top) and TUBB3$^+$ (bottom) cells.

(K) Genes down- ("DMSO gene score", left) or upregulated ("ribociclib gene score", right) in BT690 and HSJD-GBM-002 following ribociclib treatment scored in patient DHG-H3G34 snRNA-seq data, plotted as 2D-representation of RG/NPC-like score, INPC/eIN-like vs. AC/MES-like scores.

(L) Dotplot of gene set enrichment analysis for DHG-H3G34 scRNA-seq tumor signatures in differentially expressed genes after ribociclib treatment in BT690 and HSJD-GBM-002. Color scale: normalized enrichment score, dot size: -log10 of the BH-adjusted *p* value.

See also Figure S6.

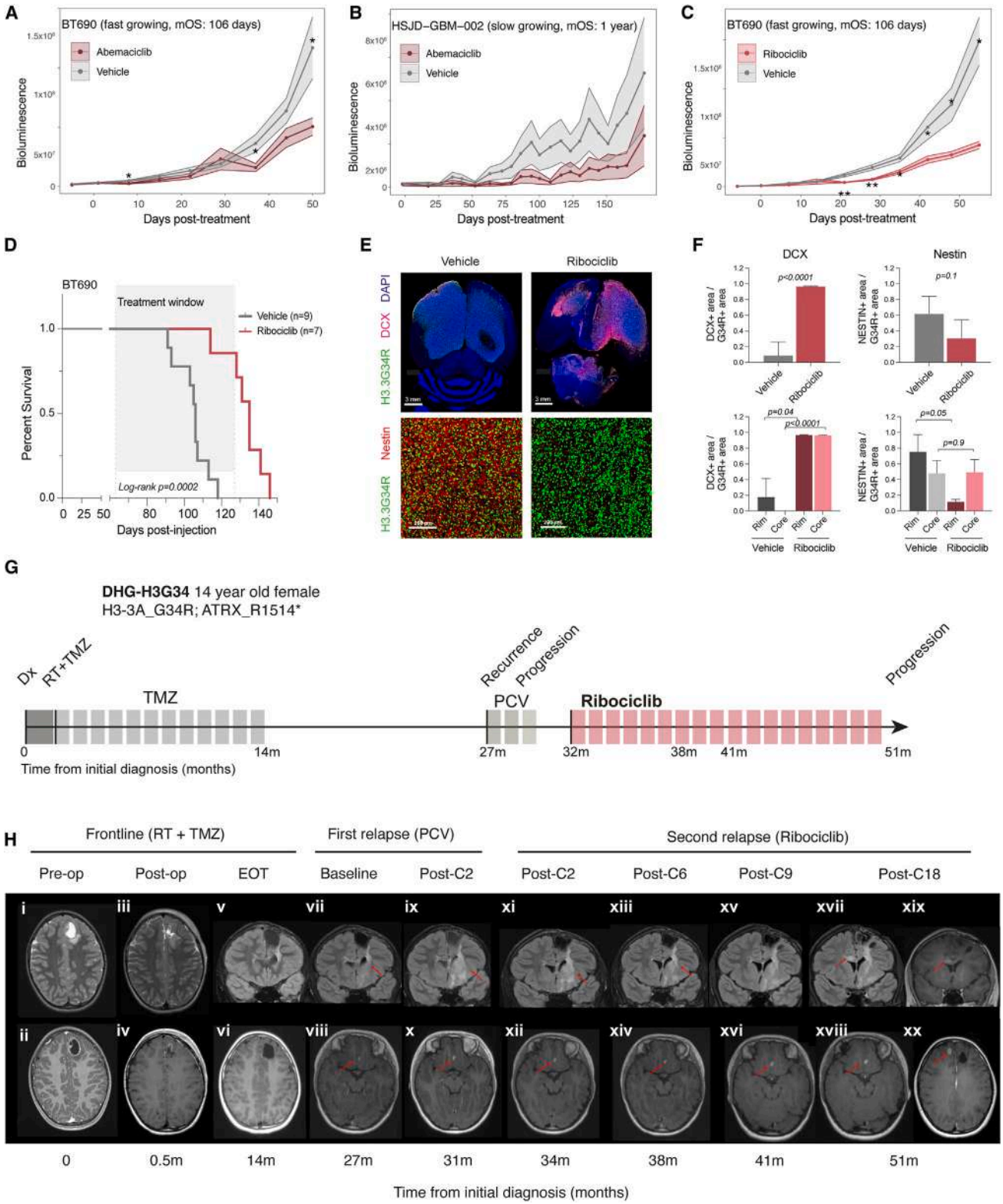

Figure 7. Efficacy of CDK4/6 pharmacological inhibition in DHG-H3G34 *in vivo* and in a patient with progressive DHG-H3G34

(A) BLI quantification of animals with DHG-H3G34R BT690 tumors treated orally with 75 mg/kg abemaciclib ($n = 7$) or vehicle ($n = 8$) (*p value <0.05, two-sided unpaired Student's t test).

(legend continued on next page)

and stable disease was sustained for 18 cycles of ribociclib. After 18 cycles, MRI scan showed disease progression with new enhancing foci in the corpus callosum, left orbital gyrus, and right frontal lobe (Figure 7H). At the time of writing, the patient remained asymptomatic, attending school full time and was being considered for another line of treatment. Her progression-free survivals after first (surgery, radiotherapy, and temozolomide), second (PCV), and third (ribociclib) lines of treatment were 27, 3, and 17 months, respectively. As such, our clinical report together with our preclinical data support tolerability and efficacy of ribociclib treatment in DHG-H3G34, underscoring its potential for evaluation in a clinical trial.

In summary, we show that CDK4/6 inhibition, in particular with more target-specific and pharmacokinetically favorable ribociclib, presents an effective therapeutic strategy in DHG-H3G34, opening up avenues for clinical translation.

DISCUSSION

Here, we demonstrated that DHG-H3G34 recapitulate various stages of interneuronal lineage development, thereby following a putative developmental hierarchy, from which we derived and validated distinct targets. Parallels to normal interneuron development were also highlighted by the identification of spatial structures in DHG-H3G34 resembling developmental nests of early migratory DCX^+ interneurons surrounded by $Nestin^+$ progenitors, recently described in normal human second trimester ganglionic eminences.[35] It will be of interest to investigate in future work how different cell states interact within these nest-like structures, and what functions from normal development these niches maintain in this aberrant tumor context.

Despite intertumor heterogeneity, our pan-glioma comparisons indicated interneuronal lineage cells of varying maturity to be present in all DHG-H3G34 and more strongly directed toward GABAergic interneuronal developmental states.[8,32,72] Therefore, we conclude these states are enriched in DHG-H3G34, from which we showed distinct functional and therapeutic consequences arise.

Mounting evidence indicates that most gliomas rooted in a glial developmental hierarchy, including DMG-H3K27 and H3-wild-type/IDH-wild-type GBM, employ specific modes of neuron-glioma interactions for tumor growth.[51–59,73–75] Here, the question arises whether such interactions with the neuronal microenvironment may differ in DHG-H3G34 given their GABAergic interneuronal lineage-biased identity. Indeed, our study points toward fundamentally distinct neuron-glioma interactions in DHG-H3G34 implicated at transcriptional, co-cultural, and electrophysiological levels, laying the basis for follow-up studies to more deeply dissect the particular neurobiology of DHG-H3G34.

We further focused on the question of how this distinct interneuronal developmental hierarchy can be leveraged therapeutically in DHG-H3G34, where thus far no targeted treatments exist. Through integrating our genome-wide CRISPR-Cas9 screens with our scRNA-seq findings, we showed that DHG-H3G34 depends most on the progenitor-like compartment of its interneuronal lineage hierarchy, whose targeting abrogates tumor growth *in vitro* and *in vivo*.

Focusing on druggable targets, we highlighted the efficacy of ribociclib, a CDK4/6-specific inhibitor, *in vivo* and in a patient. CDK4/6-targeting has been broadly studied across cancers, including in H3-wild-type/IDH-wild-type GBM and DMG-H3K27. However, preclinical monotherapy studies and early-phase clinical trials have shown limited efficacy in adult GBM and are still ongoing for DMG-H3K27.[76–78] One reason for therapy failure can be attributed to the context-dependent pan-essential profile of cell-cycle regulators, necessitating careful target validation against a cancer's unique biological context.[79] Our study presents multiple lines of evidence that CDK4/6-targeting bears a specifically favorable therapeutic window in DHG-H3G34:

(i) DHG-H3G34 are particularly responsive to more specific CDK6-targeting compared to other cancers and glioma types. (ii) Efficacy of CDK4/6 inhibition in DHG-H3G34 is observed irrespective of *CDKN2A/B* and *CDK4/6* genetic status, corroborating a more pervasive effect. (iii) CDK4/6 inhibition in DHG-H3G34 perturbs its characteristic developmental biology, shifting cells from progenitor-like toward more mature interneuronal states. This aligns with described neurodevelopmental functions of CDK4/6 in driving amplification of neuronal precursor cells via regulation of cell-cycle length, while its ablation results in neuronal differentiation.[64–66,80–82] Currently, the observed increase of mature signatures following CDK4/6

(B) BLI quantification of animals with DHG-H3G34R HSJD-GBM-002 tumors treated with 75 mg/kg abemaciclib or vehicle. Last datapoint represents 75 mg/kg abemaciclib (n = 5) or vehicle (n = 6), groups started with n = 10 mice each.
(C) BLI quantification of animals with DHG-H3G34R BT690 tumors treated orally with 200 mg/kg ribociclib (n = 7) or vehicle (n = 9). In (A)–(C), the y axis denotes mean ± SEM of BLI signal measurements, the x axis denotes the days post-treatment; *p values <0.05; **p-values <0.01, two-sided unpaired t test.
(D) Kaplan-Meier analysis of BT690 xenografts from (C). Treatment window is colored in gray. p value = 0.0002 for comparison between ribociclib (n = 7) and vehicle (n = 9), log rank test.
(E) Representative IF images following treatment with ribociclib or vehicle, stained for H3.3G34R (green), DCX (magenta), DAPI (blue), Nestin (red). Scales: top: 3 mm; bottom: 200 μm.
(F) Quantification of DCX^+ $G34R^+$ tumor cells and $Nestin^+$ $G34R^+$ tumor cells in top: vehicle (n = 4) vs. ribociclib (n = 4)-treated tumors.Bottom: Quantification stratified by tumor rim vs. tumor core. p values derived from an unpaired two-sided t test. Data shown as mean ± SEM.
(G) Timeline of disease course and treatment history in a 14-year-old female patient with recurrent DHG-H3G34.
(H) MRI scans (top: axial T2 w/coronal T2-FLAIR, bottom: axial T1w post-Gadolinium) of the DHG-H3G34 patient at initial diagnosis (i, ii), after complete resection (iii, iv), after first-line radiochemotherapy (v, vi), first recurrence (vii, viii), after two cycles of PCV (ix, x). The patient then received a third cycle of procarbazine/CCNU as a holding measure while securing access to ribociclib. The scans after two (xi, xii), six (xiii, xiv), and nine cycles (xv, xvi) of ribociclib showed disease stabilization, which was sustained until the scan after 18 cycles of ribociclib showed disease progression (xvii-xx). EOT: end of treatment; PCV: procarbazine, CCNU (lomustine), vincristine; RT: radiotherapy; TMZ: temozolomide.
See also Figure S7.

inhibition could be either explained by a decrease of tumor progenitor-like states, and/or by bona fide cellular differentiation, which will need to be further discerned by future lineage tracing studies.

Collectively, we highlight that interneuron progenitor-like cells are organized in characteristic spatial niches and are governed by distinct neuron-glioma interactions and vulnerabilities in DHG-H3G34. In addition to dependencies on progenitor and early interneuronal lineage genes, we provide evidence supporting CDK4/6 inhibition as a clinically actionable avenue that perturbs this interneuronal developmental biology, thereby paving the way for further translational study.

Limitations of the study

Despite similarities to normal development, our scRNA-seq analyses also denote remarkable malignant cell-specific aberrancies, such as expression of medial (e.g., *LHX6* and *ERBB4*) and caudal ganglionic eminence markers (e.g., *MEIS2* and *SCGN*) by the same cell, suggesting hybrid states deviant from normal neurodevelopment. This highlights the complexity and limitations of categorically comparing malignant cells to their normal counterparts in light of expected tumor cell dysregulation.

This study provides proof-of-principle for CDK4/6 inhibition as a targeted option to impede DHG-H3G34 growth. However, as a standalone treatment, it is unlikely to achieve a cure given its cytostatic effects. Thus, further investigation into resistance mechanisms and combination therapies is needed. Since CDK4/6 inhibition shifts DHG-H3G34 tumor cells toward a more differentiated interneuron-like state potentially resistant to conventional anti-cancer therapies, we postulate that this establishes a therapeutic window for sequential and/or combinatorial targeting in the context of cancer neuroscience-informed augmentations,[74,83] which requires validation in future studies.

STAR★METHODS

Detailed methods are provided in the online version of this paper and include the following:

- KEY RESOURCES TABLE
- RESOURCE AVAILABILITY
  - Lead contact
  - Materials availability
  - Data and code availability
- EXPERIMENTAL MODEL AND STUDY PARTICIPANT DETAILS
  - Human patients and ethical considerations
  - Animal studies
  - Cell lines
- METHOD DETAILS
  - Tumor tissue dissociation
  - Fluorescence-activated cell sorting (FACS)
  - Immunofluorescence staining
  - Lentivirus production
  - GeCKOv2 CRISPR-Cas9 genome-wide screens
  - Avana CRISPR-Cas9 genome-wide screen
  - CRISPR-Cas9 screen validations
  - CRISPR knockout efficiency assessment using Tracking of Indels by Decomposition (TIDE) analysis
  - Western blot analysis
  - Flow cytometry
  - Chromatin lysate preparation and nucleosome IP
  - CRISPR mediated gene editing of KNS42 cells
  - Drug screen
  - Extended drugging assays with CDK4/6 inhibitors and CDK6 degrader
  - NLGN3 and BDNF proliferation experiments
  - Neuron-glioma co-culture proliferation assays
  - *In vivo* orthotopic DHG-H3G34 knockout xenograft models
  - *In vivo* orthotopic DHG-H3G34 inducible *CDK6* knockdown xenograft models
  - Bioluminescence imaging (BLI)
  - *In vivo* hyperexcitability experiments
  - Pharmakokinetic and blood-brain-barrier penetration analyses
  - Treatment of *in vivo* DHG-H3G34 orthotopic xenograft models with CDK4/6-inhibitors
  - Treatment of *in vivo* DHG-H3G34 orthotopic xenograft model HSJD-GBM-002 with CDK4/6-inhibitors
  - Treatment of *in vivo* DHG-H3G34 orthotopic xenograft model BT690 with CDK4/6-inhibitors
  - Immunostaining of PDX brains
  - Bulk RNA sequencing of patient tumors and patient-derived cells
  - Bulk RNA sequencing of DHG-H3G34 cell lines treated with CDK4/6-inhibitors
  - ChIP sequencing
  - DNA methylation array analysis
  - Affymetrix microarray expression datasets
  - Genomic DNA library preparation and sequencing
  - scRNA-seq and snRNA-seq data generation
- QUANTIFICATION AND STATISTICAL ANALYSIS
  - Analysis of genome-wide screening data
  - Integration of CRISPR screen readouts at multiple timepoints using the Chronos model
  - scRNA-seq data processing
  - Analysis of CNAs in single-cell data
  - Clustering analysis and visualization
  - Integrated definition of malignant cells
  - Analysis of the H3.3G34R/V-mutation in Smart-Seq2 data
  - Identification of intra-tumor variability programs using NMF
  - Definition of single-cell expression scores
  - Data integration and graph-based clustering
  - Annotation of metaprograms and projection onto normal human brain atlas
  - Differential gene expression analysis in cell subpopulations
  - Pseudotime analysis of scRNA-seq cell populations
  - Integration of DHG-H3G34 scRNA-seq data with genetically edited human forebrain neural stem cell transcriptomes
  - Integration of DHG-H3G34 Smart-Seq2 data with published 10x scRNA-seq data
  - Identification of active transcription factors and their regulatory modules

SUPPLEMENTAL INFORMATION

Supplemental information can be found online at https://doi.org/10.1016/j.ccell.2024.08.006.

ACKNOWLEDGMENTS

This work was supported by generous funding from the Bonnie Feldman of National Brain Tumor Society, the Claudia Adams Barr Fund, the Cuming Family Fund for Pediatric Brain Tumor Research, the Helen Gurley Brown Foundation, and the Caroline Mortimer Fund for Pediatric Neuro-Oncology (all to M.G.F.). M.G.F. holds an NIH Director's New Innovator Award (DP2 award DP2NS127705), Distinguished Scientist Award from the Sontag Foundation, A-Award from the Alex's Lemonade Stand Foundation, an NCI SPORE grant (2P50CA165962), and a Career Award for Medical Scientist from the Burroughs Wellcome Fund. This work was also carried out as part of the INSTINCT network funded by The Brain Tumour Charity, Great Ormond Street Children's Charity, and Children with Cancer UK (all to C.J.). C.J. further acknowledges support from the Billie Butterfly Fund, the CRIS Cancer

Foundation, and Cancer Research UK (C13468/A23536 and DRCRPG-Nov21\100002). We acknowledge NHS funding to the NIHR Biomedical Research Centre at The Royal Marsden and the ICR. I.L. was supported by the German Research Foundation (DFG, #LI-3486/1-1 and 3486/2-1 and under the Germany Excellence Strategy – EXC-2049 - 390688087) and the Digital Clinician Scientist Program funded by the DFG, the Charité – Universitätsmedizin Berlin, and the BIH. G.A.V.C was supported by the NCI of the NIH (T32CA272386-01A1). D.H. is supported by funding from the NIHR Great Ormond Street Hospital Biomedical Research Center. B.E. was supported by the Stand-Alone grant/Erwin Schrödinger Fellowship of the Austrian Science Fund, Vienna, Austria (#J-4311, #P36435). R.H. was supported by the German Cancer Aid (DKH, 70114214). L.M. was supported by the Physician Researcher Pathway Scholarship of the Medical University of Vienna. J.G. was supported by the Forschungsgesellschaft für zerebrale Tumore and 'Verein unser Kind'. F.C. is partly funded by the Giant Pledge via the Royal Marsden Cancer Charity (RMCC). F.C. also acknowledges funding for the Pediatric Neuro-Oncology and Drug Development Unit at The Royal Marsden Hospital by the Hall-Hunter Foundation via the RMCC. The authors thank Dr. Joshua Dempster for providing guidance on CRISPR screen analysis, and the Children's Brain Tumor Network (CBTN) for sharing the CHOP-GBM001 cell line. The authors acknowledge support from Novartis UK for providing ribociclib under their Managed Access Program in response to an unsolicited request from the treating clinicians.

AUTHOR CONTRIBUTIONS

I.L., G.A.V.C., L.B., R.F.R., C.J., and M.G.F. developed the study concept, designed the experiments, interpreted results, and wrote the manuscript with the input of all co-authors; L.B. and S.T. generated methylation and ChIP-seq data; G.A.V.C. and L.B. generated bulk RNA-seq data; Y.G., A.M., and C.J. performed methylation and ChIP-seq analyses. Y.G., A.M., C.J., I.L., and J.L. performed bulk RNA-seq analyses; I.L., G.A.V.C., M.L.S., O.A.H., H.M.M., A.N., J.S.R., A.B., and S.C. performed glioma tissue dissociation, FACS, and scRNA-seq data generation; I.L. conducted glioma scRNA-seq analyses, with contributions from L.J. and G.A.V.C.; A.B., V.M., and G.A.V.C. performed immunofluorescence studies, with contributions from C.R.; G.R. and C.H. performed immunohistochemistry; R.F.R. conducted the primary GeCKOv2 CRISPR-Cas9 screens; Y.G. analyzed and integrated primary CRISPR-Cas9 screen data; G.A.V.C., I.L., E.P., and M.L.S. performed CRISPR validations; knockout efficiency testing by western blot and TIDE analysis were performed by G.A.V.C., B.E., I.L., and S.E.H., respectively; L.B., G.A.V.C., I.L., R.H., and S.N. conducted drug screen experiments, which were analyzed by I.L. and A.M.; G.A.V.C. and L.B. performed flow experiments and cell cycle analyses; S.T., S.M., and L.M. contributed to processing of patient tissues; G.A.V.C, A.C., M. Morrow, and Q.D.N. performed *in vivo* knockout and inducible knockdown studies; G.A.V.C., I.L., A.C., M. Morrow, Q.D.N., L.B., F.R., and R.R. performed *in vivo* drugging, tolerablity, and pharmacokinetic studies; T.B. and M.A.Q. performed *in vivo* hyperexcitability and neuron-glioma co-culture studies; DHG-H3G34 glioma cell line, primary tissue, antibody resources, and pathology consultation were provided by R.G., C.D., K.L.L., R.T.A., B.L., S.U., C.K., S.A., D.D.E., F.C., S.S., C.B., A.M., K.A.C., A.J.W., A.M.C., U.S., M.V., D.H., C.H., J.G., I.S., M. Monje; human developmental brain single-cell atlas data were generated by E.B., L.H., and E.S., analyzed by M.D.G. and S.L., and supervised by S.L.; human adult brain single-cell data were generated by K.S., L.H., and R.H., analyzed by K.S. and S.L., and supervised by E.L. and S.L; treatment and follow-up of the DHG-H3G34 patient was provided through F.C., A.K., and M.P.-S.; M. Monje provided guidance on glioma neurobiology; C.J. and M.G.F. supervised and funded the study.

DECLARATION OF INTERESTS

M.G.F. is a consultant for Twentyeight-Seven Therapeutics and Blueprint Medicines. M.M. is an SAB member for Cygnal Therapeutics. K.L.L. is founder and equity holder of Travera Inc. and receives consulting fees from BMS, Integragen, and Rarecyte, and research support from Lilly, BMS, and Amgen. D.H. has acted as an advisor for Novartis in relation to ribociclib.

Received: July 11, 2023
Revised: May 24, 2024
Accepted: August 7, 2024
Published: September 3, 2024

REFERENCES

1. Ostrom, Q.T., Patil, N., Cioffi, G., Waite, K., Kruchko, C., and Barnholtz-Sloan, J.S. (2020). CBTRUS Statistical Report: Primary Brain and Other Central Nervous System Tumors Diagnosed in the United States in 2013-2017. Neuro Oncol. *22*, iv1–iv96. https://doi.org/10.1093/neuonc/noaa200.
2. Schwartzentruber, J., Korshunov, A., Liu, X.Y., Jones, D.T.W., Pfaff, E., Jacob, K., Sturm, D., Fontebasso, A.M., Quang, D.A.K., Tönjes, M., et al. (2012). Driver mutations in histone H3.3 and chromatin remodelling genes in paediatric glioblastoma. Nature *482*, 226–231. https://doi.org/10.1038/nature10833.
3. Wu, G., Broniscer, A., McEachron, T.A., Lu, C., Paugh, B.S., Becksfort, J., Qu, C., Ding, L., Huether, R., Parker, M., et al. (2012). Somatic histone H3 alterations in pediatric diffuse intrinsic pontine gliomas and non-brainstem glioblastomas. Nat. Genet. *44*, 251–253. https://doi.org/10.1038/ng.1102.
4. Sturm, D., Witt, H., Hovestadt, V., Khuong-Quang, D.A., Jones, D.T.W., Konermann, C., Pfaff, E., Tönjes, M., Sill, M., Bender, S., et al. (2012). Hotspot mutations in H3F3A and IDH1 define distinct epigenetic and biological subgroups of glioblastoma. Cancer Cell *22*, 425–437. https://doi.org/10.1016/j.ccr.2012.08.024.
5. Louis, D.N., Perry, A., Wesseling, P., Brat, D.J., Cree, I.A., Figarella-Branger, D., Hawkins, C., Ng, H.K., Pfister, S.M., Reifenberger, G., et al. (2021). The 2021 WHO Classification of Tumors of the Central Nervous System: a summary. Neuro Oncol. *23*, 1231–1251. https://doi.org/10.1093/neuonc/noab106.
6. Jones, C., and Baker, S.J. (2014). Unique genetic and epigenetic mechanisms driving paediatric diffuse high-grade glioma. Nat. Rev. Cancer *14*, 651–661. https://doi.org/10.1038/nrc3811.
7. Filbin, M., and Monje, M. (2019). Developmental origins and emerging therapeutic opportunities for childhood cancer. Nat. Med. *25*, 367–376. https://doi.org/10.1038/s41591-019-0383-9.
8. Filbin, M.G., Tirosh, I., Hovestadt, V., Shaw, M.L., Escalante, L.E., Mathewson, N.D., Neftel, C., Frank, N., Pelton, K., Hebert, C.M., et al. (2018). Developmental and oncogenic programs in H3K27M gliomas dissected by single-cell RNA-seq. Science *360*, 331–335. https://doi.org/10.1126/science.aao4750.
9. Jessa, S., Blanchet-Cohen, A., Krug, B., Vladoiu, M., Coutelier, M., Faury, D., Poreau, B., De Jay, N., Hébert, S., Monlong, J., et al. (2019). Stalled developmental programs at the root of pediatric brain tumors. Nat. Genet. *51*, 1702–1713. https://doi.org/10.1038/s41588-019-0531-7.
10. Monje, M., Mitra, S.S., Freret, M.E., Raveh, T.B., Kim, J., Masek, M., Attema, J.L., Li, G., Haddix, T., Edwards, M.S.B., et al. (2011). Hedgehog-responsive candidate cell of origin for diffuse intrinsic pontine glioma. Proc. Natl. Acad. Sci. USA *108*, 4453–4458. https://doi.org/10.1073/pnas.1101657108.
11. Nagaraja, S., Vitanza, N.A., Woo, P.J., Taylor, K.R., Liu, F., Zhang, L., Li, M., Meng, W., Ponnuswami, A., Sun, W., et al. (2017). Transcriptional Dependencies in Diffuse Intrinsic Pontine Glioma. Cancer Cell *31*, 635–652.e6. https://doi.org/10.1016/j.ccell.2017.03.011.
12. Nagaraja, S., Quezada, M.A., Gillespie, S.M., Arzt, M., Lennon, J.J., Woo, P.J., Hovestadt, V., Kambhampati, M., Filbin, M.G., Suva, M.L., et al. (2019). Histone Variant and Cell Context Determine H3K27M Reprogramming of the Enhancer Landscape and Oncogenic State. Mol. Cell *76*, 965–980.e12. https://doi.org/10.1016/j.molcel.2019.08.030.
13. Pathania, M., De Jay, N., Maestro, N., Harutyunyan, A.S., Nitarska, J., Pahlavan, P., Henderson, S., Mikael, L.G., Richard-Londt, A., Zhang,

Y., et al. (2017). H3.3(K27M) Cooperates with Trp53 Loss and PDGFRA Gain in Mouse Embryonic Neural Progenitor Cells to Induce Invasive High-Grade Gliomas. Cancer Cell *32*, 684–700.e9. https://doi.org/10.1016/j.ccell.2017.09.014.

14. Haag, D., Mack, N., Benites Goncalves da Silva, P., Statz, B., Clark, J., Tanabe, K., Sharma, T., Jäger, N., Jones, D.T.W., Kawauchi, D., et al. (2021). H3.3-K27M drives neural stem cell-specific gliomagenesis in a human iPSC-derived model. Cancer Cell *39*, 407–422.e13. https://doi.org/10.1016/j.ccell.2021.01.005.

15. Liu, I., Jiang, L., Samuelsson, E.R., Marco Salas, S., Beck, A., Hack, O.A., Jeong, D., Shaw, M.L., Englinger, B., LaBelle, J., et al. (2022). The landscape of tumor cell states and spatial organization in H3-K27M mutant diffuse midline glioma across age and location. Nat. Genet. *54*, 1881–1894. https://doi.org/10.1038/s41588-022-01236-3.

16. Jessa, S., Mohammadnia, A., Harutyunyan, A.S., Hulswit, M., Varadharajan, S., Lakkis, H., Kabir, N., Bashardanesh, Z., Hébert, S., Faury, D., et al. (2022). K27M in canonical and noncanonical H3 variants occurs in distinct oligodendroglial cell lineages in brain midline gliomas. Nat. Genet. *54*, 1865–1880. https://doi.org/10.1038/s41588-022-01205-w.

17. Bjerke, L., Mackay, A., Nandhabalan, M., Burford, A., Jury, A., Popov, S., Bax, D.A., Carvalho, D., Taylor, K.R., Vinci, M., et al. (2013). Histone H3.3. mutations drive pediatric glioblastoma through upregulation of MYCN. Cancer Discov. *3*, 512–519. https://doi.org/10.1158/2159-8290.CD-12-0426.

18. Mackay, A., Burford, A., Carvalho, D., Izquierdo, E., Fazal-Salom, J., Taylor, K.R., Bjerke, L., Clarke, M., Vinci, M., Nandhabalan, M., et al. (2017). Integrated Molecular Meta-Analysis of 1,000 Pediatric High-Grade and Diffuse Intrinsic Pontine Glioma. Cancer Cell *32*, 520–537.e5. https://doi.org/10.1016/j.ccell.2017.08.017.

19. Chen, C.C.L., Deshmukh, S., Jessa, S., Hadjadj, D., Lisi, V., Andrade, A.F., Faury, D., Jawhar, W., Dali, R., Suzuki, H., et al. (2020). Histone H3.3G34-Mutant Interneuron Progenitors Co-opt PDGFRA for Gliomagenesis. Cell *183*, 1617–1633.e22. https://doi.org/10.1016/j.cell.2020.11.012.

20. Bressan, R.B., Southgate, B., Ferguson, K.M., Blin, C., Grant, V., Alfazema, N., Wills, J.C., Marques-Torrejon, M.A., Morrison, G.M., Ashmore, J., et al. (2021). Regional identity of human neural stem cells determines oncogenic responses to histone H3.3 mutants. Cell Stem Cell *28*, 877–893.e9. https://doi.org/10.1016/j.stem.2021.01.016.

21. Funato, K., Smith, R.C., Saito, Y., and Tabar, V. (2021). Dissecting the impact of regional identity and the oncogenic role of human-specific NOTCH2NL in an hESC model of H3.3G34R-mutant glioma. Cell Stem Cell *28*, 894–905.e7. https://doi.org/10.1016/j.stem.2021.02.003.

22. Krug, B., De Jay, N., Harutyunyan, A.S., Deshmukh, S., Marchione, D.M., Guilhamon, P., Bertrand, K.C., Mikael, L.G., McConechy, M.K., Chen, C.C.L., et al. (2019). Pervasive H3K27 Acetylation Leads to ERV Expression and a Therapeutic Vulnerability in H3K27M Gliomas. Cancer Cell *36*, 338–339. https://doi.org/10.1016/j.ccell.2019.08.012.

23. Mackay, A., Burford, A., Molinari, V., Jones, D.T.W., Izquierdo, E., Brouwer-Visser, J., Giangaspero, F., Haberler, C., Pietsch, T., Jacques, T.S., et al. (2018). Molecular, Pathological, Radiological, and Immune Profiling of Non-brainstem Pediatric High-Grade Glioma from the HERBY Phase II Randomized Trial. Cancer Cell *33*, 829–842.e5. https://doi.org/10.1016/j.ccell.2018.04.004.

24. Wu, G., Diaz, A.K., Paugh, B.S., Rankin, S.L., Ju, B., Li, Y., Zhu, X., Qu, C., Chen, X., Zhang, J., et al. (2014). The genomic landscape of diffuse intrinsic pontine glioma and pediatric non-brainstem high-grade glioma. Nat. Genet. *46*, 444–450. https://doi.org/10.1038/ng.2938.

25. Nowakowski, T.J., Bhaduri, A., Pollen, A.A., Alvarado, B., Mostajo-Radji, M.A., Di Lullo, E., Haeussler, M., Sandoval-Espinosa, C., Liu, S.J., Velmeshev, D., et al. (2017). Spatiotemporal gene expression trajectories reveal developmental hierarchies of the human cortex. Science *358*, 1318–1323. https://doi.org/10.1126/science.aap8809.

26. Pollen, A.A., Nowakowski, T.J., Chen, J., Retallack, H., Sandoval-Espinosa, C., Nicholas, C.R., Shuga, J., Liu, S.J., Oldham, M.C., Diaz, A., et al. (2015). Molecular identity of human outer radial glia during cortical development. Cell *163*, 55–67. https://doi.org/10.1016/j.cell.2015.09.004.

27. Bhaduri, A., Di Lullo, E., Jung, D., Müller, S., Crouch, E.E., Espinosa, C.S., Ozawa, T., Alvarado, B., Spatazza, J., Cadwell, C.R., et al. (2020). Outer Radial Glia-like Cancer Stem Cells Contribute to Heterogeneity of Glioblastoma. Cell Stem Cell *26*, 48–63.e6. https://doi.org/10.1016/j.stem.2019.11.015.

28. Kriegstein, A.R., Subramanian, L., Obernier, K., and Alvarez-Buylla, A. (2020). Chapter 31 - Neural stem cells among glia. In Patterning and Cell Type Specification in the Developing CNS and PNS, Second Edition, J. Rubenstein, P. Rakic, B. Chen, and K.Y. Kwan, eds. (Academic Press), pp. 775–806. https://doi.org/10.1016/B978-0-12-814405-3.00031-X.

29. Mayer, C., Hafemeister, C., Bandler, R.C., Machold, R., Batista Brito, R., Jaglin, X., Allaway, K., Butler, A., Fishell, G., and Satija, R. (2018). Developmental diversification of cortical inhibitory interneurons. Nature *555*, 457–462. https://doi.org/10.1038/nature25999.

30. Velmeshev, D., Chavali, M., Nowakowski, T.J., Bhade, M., Mayer, S., Goyal, N., Alvarado, B., Mancia, W., Wang, S., Speir, M., et al. (2021). Molecular diversity and lineage commitment of human interneuron progenitors. Preprint at bioRxiv. https://doi.org/10.1101/2021.05.13.444045.

31. Hansen, D.V., Lui, J.H., Flandin, P., Yoshikawa, K., Rubenstein, J.L., Alvarez-Buylla, A., and Kriegstein, A.R. (2013). Non-epithelial stem cells and cortical interneuron production in the human ganglionic eminences. Nat. Neurosci. *16*, 1576–1587. https://doi.org/10.1038/nn.3541.

32. Neftel, C., Laffy, J., Filbin, M.G., Hara, T., Shore, M.E., Rahme, G.J., Richman, A.R., Silverbush, D., Shaw, M.L., Hebert, C.M., et al. (2019). An Integrative Model of Cellular States, Plasticity, and Genetics for Glioblastoma. Cell *178*, 835–849.e21. https://doi.org/10.1016/j.cell.2019.06.024.

33. Venteicher, A.S., Tirosh, I., Hebert, C., Yizhak, K., Neftel, C., Filbin, M.G., Hovestadt, V., Escalante, L.E., Shaw, M.L., Rodman, C., et al. (2017). Decoupling genetics, lineages, and microenvironment in IDH-mutant gliomas by single-cell RNA-seq. Science *355*, eaai8478. https://doi.org/10.1126/science.aai8478.

34. Tirosh, I., Venteicher, A.S., Hebert, C., Escalante, L.E., Patel, A.P., Yizhak, K., Fisher, J.M., Rodman, C., Mount, C., Filbin, M.G., et al. (2016). Single-cell RNA-seq supports a developmental hierarchy in human oligodendroglioma. Nature *539*, 309–313. https://doi.org/10.1038/nature20123.

35. Paredes, M.F., Mora, C., Flores-Ramirez, Q., Cebrian-Silla, A., Del Dosso, A., Larimer, P., Chen, J., Kang, G., Gonzalez Granero, S., Garcia, E., et al. (2022). Nests of dividing neuroblasts sustain interneuron production for the developing human brain. Science *375*, eabk2346. https://doi.org/10.1126/science.abk2346.

36. Shi, Y., Wang, M., Mi, D., Lu, T., Wang, B., Dong, H., Zhong, S., Chen, Y., Sun, L., Zhou, X., et al. (2021). Mouse and human share conserved transcriptional programs for interneuron development. Science *374*, eabj6641. https://doi.org/10.1126/science.abj6641.

37. Garofano, L., Migliozzi, S., Oh, Y.T., D'Angelo, F., Najac, R.D., Ko, A., Frangaj, B., Caruso, F.P., Yu, K., Yuan, J., et al. (2021). Pathway-based classification of glioblastoma uncovers a mitochondrial subtype with therapeutic vulnerabilities. Nat. Cancer *2*, 141–156. https://doi.org/10.1038/s43018-020-00159-4.

38. Aibar, S., González-Blas, C.B., Moerman, T., Huynh-Thu, V.A., Imrichova, H., Hulselmans, G., Rambow, F., Marine, J.C., Geurts, P., Aerts, J., et al. (2017). SCENIC: single-cell regulatory network inference and clustering. Nat. Methods *14*, 1083–1086. https://doi.org/10.1038/nmeth.4463.

39. Migliozzi, S., Oh, Y.T., Hasanain, M., Garofano, L., D'Angelo, F., Najac, R.D., Picca, A., Bielle, F., Di Stefano, A.L., Lerond, J., et al. (2023).

Integrative multi-omics networks identify PKCdelta and DNA-PK as master kinases of glioblastoma subtypes and guide targeted cancer therapy. Nat. Cancer *4*, 181–202. https://doi.org/10.1038/s43018-022-00510-x.

40. Kim, K.H., Migliozzi, S., Koo, H., Hong, J.H., Park, S.M., Kim, S., Kwon, H.J., Ha, S., Garofano, L., Oh, Y.T., et al. (2024). Integrated proteogenomic characterization of glioblastoma evolution. Cancer Cell *42*, 358–377.e8. https://doi.org/10.1016/j.ccell.2023.12.015.
41. Decressac, M., Wright, B., David, B., Tyers, P., Jaber, M., Barker, R.A., and Gaillard, A. (2011). Exogenous neuropeptide Y promotes *in vivo* hippocampal neurogenesis. Hippocampus *21*, 233–238. https://doi.org/10.1002/hipo.20765.
42. Howell, O.W., Doyle, K., Goodman, J.H., Scharfman, H.E., Herzog, H., Pringle, A., Beck-Sickinger, A.G., and Gray, W.P. (2005). Neuropeptide Y stimulates neuronal precursor proliferation in the post-natal and adult dentate gyrus. J. Neurochem. *93*, 560–570. https://doi.org/10.1111/j.1471-4159.2005.03057.x.
43. Karagiannis, A., Gallopin, T., Dávid, C., Battaglia, D., Geoffroy, H., Rossier, J., Hillman, E.M.C., Staiger, J.F., and Cauli, B. (2009). Classification of NPY-expressing neocortical interneurons. J. Neurosci. *29*, 3642–3659. https://doi.org/10.1523/JNEUROSCI.0058-09.2009.
44. Jain, S.U., Khazaei, S., Marchione, D.M., Lundgren, S.M., Wang, X., Weinberg, D.N., Deshmukh, S., Juretic, N., Lu, C., Allis, C.D., et al. (2020). Histone H3.3 G34 mutations promote aberrant PRC2 activity and drive tumor progression. Proc. Natl. Acad. Sci. USA *117*, 27354–27364. https://doi.org/10.1073/pnas.2006076117.
45. Khazaei, S., Chen, C.C.L., Andrade, A.F., Kabir, N., Azarafshar, P., Morcos, S.M., França, J.A., Lopes, M., Lund, P.J., Danieau, G., et al. (2023). Single substitution in H3.3G34 alters DNMT3A recruitment to cause progressive neurodegeneration. Cell *186*, 1162–1178.e20. https://doi.org/10.1016/j.cell.2023.02.023.
46. Voon, H.P.J., Udugama, M., Lin, W., Hii, L., Law, R.H.P., Steer, D.L., Das, P.P., Mann, J.R., and Wong, L.H. (2018). Inhibition of a K9/K36 demethylase by an H3.3 point mutation found in paediatric glioblastoma. Nat. Commun. *9*, 3142. https://doi.org/10.1038/s41467-018-05607-5.
47. Kabayiza, K.U., Masgutova, G., Harris, A., Rucchin, V., Jacob, B., and Clotman, F. (2017). The Onecut Transcription Factors Regulate Differentiation and Distribution of Dorsal Interneurons during Spinal Cord Development. Front. Mol. Neurosci. *10*, 157. https://doi.org/10.3389/fnmol.2017.00157.
48. Liu, Y., and Zhang, Y. (2019). ETV5 is Essential for Neuronal Differentiation of Human Neural Progenitor Cells by Repressing NEUROG2 Expression. Stem Cell Rev. Rep. *15*, 703–716. https://doi.org/10.1007/s12015-019-09904-4.
49. Varju, P., Katarova, Z., Madarász, E., and Szabó, G. (2002). Sequential induction of embryonic and adult forms of glutamic acid decarboxylase during *in vitro*-induced neurogenesis in cloned neuroectodermal cell-line, NE-7C2. J. Neurochem. *80*, 605–615. https://doi.org/10.1046/j.0022-3042.2001.00733.x.
50. Minelli, A., Alonso-Nanclares, L., Edwards, R.H., DeFelipe, J., and Conti, F. (2003). Postnatal development of the vesicular GABA transporter in rat cerebral cortex. Neuroscience *117*, 337–346. https://doi.org/10.1016/s0306-4522(02)00864-3.
51. Buckingham, S.C., Campbell, S.L., Haas, B.R., Montana, V., Robel, S., Ogunrinu, T., and Sontheimer, H. (2011). Glutamate release by primary brain tumors induces epileptic activity. Nat. Med. *17*, 1269–1274. https://doi.org/10.1038/nm.2453.
52. Campbell, S.L., Buckingham, S.C., and Sontheimer, H. (2012). Human glioma cells induce hyperexcitability in cortical networks. Epilepsia *53*, 1360–1370. https://doi.org/10.1111/j.1528-1167.2012.03557.x.
53. John Lin, C.C., Yu, K., Hatcher, A., Huang, T.W., Lee, H.K., Carlson, J., Weston, M.C., Chen, F., Zhang, Y., Zhu, W., et al. (2017). Identification of diverse astrocyte populations and their malignant analogs. Nat. Neurosci. *20*, 396–405. https://doi.org/10.1038/nn.4493.
54. Venkatesh, H.S., Morishita, W., Geraghty, A.C., Silverbush, D., Gillespie, S.M., Arzt, M., Tam, L.T., Espenel, C., Ponnuswami, A., Ni, L., et al. (2019). Electrical and synaptic integration of glioma into neural circuits. Nature *573*, 539–545. https://doi.org/10.1038/s41586-019-1563-y.
55. Venkatesh, H.S., Johung, T.B., Caretti, V., Noll, A., Tang, Y., Nagaraja, S., Gibson, E.M., Mount, C.W., Polepalli, J., Mitra, S.S., et al. (2015). Neuronal Activity Promotes Glioma Growth through Neuroligin-3 Secretion. Cell *161*, 803–816. https://doi.org/10.1016/j.cell.2015.04.012.
56. Venkatesh, H.S., Tam, L.T., Woo, P.J., Lennon, J., Nagaraja, S., Gillespie, S.M., Ni, J., Duveau, D.Y., Morris, P.J., Zhao, J.J., et al. (2017). Targeting neuronal activity-regulated neuroligin-3 dependency in high-grade glioma. Nature *549*, 533–537. https://doi.org/10.1038/nature24014.
57. Pan, Y., Hysinger, J.D., Barron, T., Schindler, N.F., Cobb, O., Guo, X., Yalçın, B., Anastasaki, C., Mulinyawe, S.B., Ponnuswami, A., et al. (2021). NF1 mutation drives neuronal activity-dependent initiation of optic glioma. Nature *594*, 277–282. https://doi.org/10.1038/s41586-021-03580-6.
58. Venkataramani, V., Tanev, D.I., Strahle, C., Studier-Fischer, A., Fankhauser, L., Kessler, T., Körber, C., Kardorff, M., Ratliff, M., Xie, R., et al. (2019). Glutamatergic synaptic input to glioma cells drives brain tumour progression. Nature *573*, 532–538. https://doi.org/10.1038/s41586-019-1564-x.
59. Venkataramani, V., Schneider, M., Giordano, F.A., Kuner, T., Wick, W., Herrlinger, U., and Winkler, F. (2022). Disconnecting multicellular networks in brain tumours. Nat. Rev. Cancer *22*, 481–491. https://doi.org/10.1038/s41568-022-00475-0.
60. Dempster, J.M., Pacini, C., Pantel, S., Behan, F.M., Green, T., Krill-Burger, J., Beaver, C.M., Younger, S.T., Zhivich, V., Najgebauer, H., et al. (2019). Agreement between two large pan-cancer CRISPR-Cas9 gene dependency data sets. Nat. Commun. *10*, 5817. https://doi.org/10.1038/s41467-019-13805-y.
61. Meyers, R.M., Bryan, J.G., McFarland, J.M., Weir, B.A., Sizemore, A.E., Xu, H., Dharia, N.V., Montgomery, P.G., Cowley, G.S., Pantel, S., et al. (2017). Computational correction of copy number effect improves specificity of CRISPR-Cas9 essentiality screens in cancer cells. Nat. Genet. *49*, 1779–1784. https://doi.org/10.1038/ng.3984.
62. Sun, C.X., Daniel, P., Bradshaw, G., Shi, H., Loi, M., Chew, N., Parackal, S., Tsui, V., Liang, Y., Koptyra, M., et al. (2023). Generation and multidimensional profiling of a childhood cancer cell line atlas defines new therapeutic opportunities. Cancer Cell *41*, 660–677.e7. https://doi.org/10.1016/j.ccell.2023.03.007.
63. Hafner, M., Mills, C.E., Subramanian, K., Chen, C., Chung, M., Boswell, S.A., Everley, R.A., Liu, C., Walmsley, C.S., Juric, D., and Sorger, P.K. (2019). Multiomics Profiling Establishes the Polypharmacology of FDA-Approved CDK4/6 Inhibitors and the Potential for Differential Clinical Activity. Cell Chem. Biol. *26*, 1067–1080.e8. https://doi.org/10.1016/j.chembiol.2019.05.005.
64. Mi, D., Carr, C.B., Georgala, P.A., Huang, Y.T., Manuel, M.N., Jeanes, E., Niisato, E., Sansom, S.N., Livesey, F.J., Theil, T., et al. (2013). Pax6 exerts regional control of cortical progenitor proliferation via direct repression of Cdk6 and hypophosphorylation of pRb. Neuron *78*, 269–284. https://doi.org/10.1016/j.neuron.2013.02.012.
65. Beukelaers, P., Vandenbosch, R., Caron, N., Nguyen, L., Belachew, S., Moonen, G., Kiyokawa, H., Barbacid, M., Santamaria, D., and Malgrange, B. (2011). Cdk6-dependent regulation of G(1) length controls adult neurogenesis. Stem Cell. *29*, 713–724. https://doi.org/10.1002/stem.616.
66. Chirivella, L., Kirstein, M., Ferrón, S.R., Domingo-Muelas, A., Durupt, F.C., Acosta-Umanzor, C., Cano-Jaimez, M., Pérez-Sánchez, F., Barbacid, M., Ortega, S., et al. (2017). Cyclin-Dependent Kinase 4 Regulates Adult Neural Stem Cell Proliferation and Differentiation in Response to Insulin. Stem Cell. *35*, 2403–2416. https://doi.org/10.1002/stem.2694.
67. Jusino, S., Fadul, C.E., and Dillon, P. (2023). Systematic review of the management of brain metastases from hormone receptor positive breast cancer. J. Neuro Oncol. *162*, 45–57. https://doi.org/10.1007/s11060-023-04276-9.

68. Tien, A.C., Li, J., Bao, X., Derogatis, A., Kim, S., Mehta, S., and Sanai, N. (2019). A Phase 0 Trial of Ribociclib in Recurrent Glioblastoma Patients Incorporating a Tumor Pharmacodynamic- and Pharmacokinetic-Guided Expansion Cohort. Clin. Cancer Res. *25*, 5777–5786. https://doi.org/10.1158/1078-0432.CCR-19-0133.

69. Patel, Y.T., Davis, A., Baker, S.J., Campagne, O., and Stewart, C.F. (2019). CNS penetration of the CDK4/6 inhibitor ribociclib in non-tumor bearing mice and mice bearing pediatric brain tumors. Cancer Chemother. Pharmacol. *84*, 447–452. https://doi.org/10.1007/s00280-019-03864-9.

70. Raub, T.J., Wishart, G.N., Kulanthaivel, P., Staton, B.A., Ajamie, R.T., Sawada, G.A., Gelbert, L.M., Shannon, H.E., Sanchez-Martinez, C., and De Dios, A. (2015). Brain Exposure of Two Selective Dual CDK4 and CDK6 Inhibitors and the Antitumor Activity of CDK4 and CDK6 Inhibition in Combination with Temozolomide in an Intracranial Glioblastoma Xenograft. Drug Metab. Dispos. *43*, 1360–1371. https://doi.org/10.1124/dmd.114.062745.

71. Geoerger, B., Bourdeaut, F., DuBois, S.G., Fischer, M., Geller, J.I., Gottardo, N.G., Marabelle, A., Pearson, A.D.J., Modak, S., Cash, T., et al. (2017). A Phase I Study of the CDK4/6 Inhibitor Ribociclib (LEE011) in Pediatric Patients with Malignant Rhabdoid Tumors, Neuroblastoma, and Other Solid Tumors. Clin. Cancer Res. *23*, 2433–2441. https://doi.org/10.1158/1078-0432.CCR-16-2898.

72. Liu, I., Jiang, L., Samuelsson, E., Salas, S.M., LaBelle, J., Nilsson, M., and Filbin, M. (2022). The landscape of tumor cell states and spatial organization in H3-K27M mutant diffuse midline glioma across age and location. Custom scripts v1.0.0. https://doi.org/10.5281/zenodo.7073167.

73. Chen, P., Wang, W., Liu, R., Lyu, J., Zhang, L., Li, B., Qiu, B., Tian, A., Jiang, W., Ying, H., et al. (2022). Olfactory sensory experience regulates gliomagenesis via neuronal IGF1. Nature *606*, 550–556. https://doi.org/10.1038/s41586-022-04719-9.

74. Hausmann, D., Hoffmann, D.C., Venkataramani, V., Jung, E., Horschitz, S., Tetzlaff, S.K., Jabali, A., Hai, L., Kessler, T., Azoŕin, D.D., et al. (2023). Autonomous rhythmic activity in glioma networks drives brain tumour growth. Nature *613*, 179–186. https://doi.org/10.1038/s41586-022-05520-4.

75. Osswald, M., Jung, E., Sahm, F., Solecki, G., Venkataramani, V., Blaes, J., Weil, S., Horstmann, H., Wiestler, B., Syed, M., et al. (2015). Brain tumour cells interconnect to a functional and resistant network. Nature *528*, 93–98. https://doi.org/10.1038/nature16071.

76. Li, M., Xiao, A., Floyd, D., Olmez, I., Lee, J., Godlewski, J., Bronisz, A., Bhat, K.P.L., Sulman, E.P., Nakano, I., and Purow, B. (2017). CDK4/6 inhibition is more active against the glioblastoma proneural subtype. Oncotarget *8*, 55319–55331. https://doi.org/10.18632/oncotarget.19429.

77. Juric, V., and Murphy, B. (2020). Cyclin-dependent kinase inhibitors in brain cancer: current state and future directions. Cancer Drug Resist. *3*, 48–62. https://doi.org/10.20517/cdr.2019.105.

78. DeWire, M., Fuller, C., Hummel, T.R., Chow, L.M.L., Salloum, R., de Blank, P., Pater, L., Lawson, S., Zhu, X., Dexheimer, P., et al. (2020). A phase I/II study of ribociclib following radiation therapy in children with newly diagnosed diffuse intrinsic pontine glioma (DIPG). J. Neuro Oncol. *149*, 511–522. https://doi.org/10.1007/s11060-020-03641-2.

79. Chang, L., Ruiz, P., Ito, T., and Sellers, W.R. (2021). Targeting pan-essential genes in cancer: Challenges and opportunities. Cancer Cell *39*, 466–479. https://doi.org/10.1016/j.ccell.2020.12.008.

80. Grison, A., Gaiser, C., Bieder, A., Baranek, C., and Atanasoski, S. (2018). Ablation of cdk4 and cdk6 affects proliferation of basal progenitor cells in the developing dorsal and ventral forebrain. Dev. Neurobiol. *78*, 660–670. https://doi.org/10.1002/dneu.22588.

81. Hasenpusch-Theil, K., West, S., Kelman, A., Kozic, Z., Horrocks, S., McMahon, A.P., Price, D.J., Mason, J.O., and Theil, T. (2018). Gli3 controls the onset of cortical neurogenesis by regulating the radial glial cell cycle through Cdk6 expression. Development *145*, dev163147. https://doi.org/10.1242/dev.163147.

82. Bershteyn, M., Broer, S., Parekh, M., Maury, Y., Havlicek, S., Kriks, S., Fuentealba, L., Lee, S., Zhou, R., Subramanyam, G., et al. (2023). Human pallial MGE-type GABAergic interneuron cell therapy for chronic focal epilepsy. Cell Stem Cell *30*, 1331–1350.e11. https://doi.org/10.1016/j.stem.2023.08.013.

83. Winkler, F., Venkatesh, H.S., Amit, M., Batchelor, T., Demir, I.E., Deneen, B., Gutmann, D.H., Hervey-Jumper, S., Kuner, T., Mabbott, D., et al. (2023). Cancer neuroscience: State of the field, emerging directions. Cell *186*, 1689–1707. https://doi.org/10.1016/j.cell.2023.02.002.

84. Capper, D., Jones, D.T.W., Sill, M., Hovestadt, V., Schrimpf, D., Sturm, D., Koelsche, C., Sahm, F., Chavez, L., Reuss, D.E., et al. (2018). DNA methylation-based classification of central nervous system tumours. Nature *555*, 469–474. https://doi.org/10.1038/nature26000.

85. Sturm, D., Orr, B.A., Toprak, U.H., Hovestadt, V., Jones, D.T.W., Capper, D., Sill, M., Buchhalter, I., Northcott, P.A., Leis, I., et al. (2016). New Brain Tumor Entities Emerge from Molecular Classification of CNS-PNETs. Cell *164*, 1060–1072. https://doi.org/10.1016/j.cell.2016.01.015.

86. Li, B., and Dewey, C.N. (2011). RSEM: accurate transcript quantification from RNA-Seq data with or without a reference genome. BMC Bioinf. *12*, 323. https://doi.org/10.1186/1471-2105-12-323.

87. Fan, J., Salathia, N., Liu, R., Kaeser, G.E., Yung, Y.C., Herman, J.L., Kaper, F., Fan, J.B., Zhang, K., Chun, J., and Kharchenko, P.V. (2016). Characterizing transcriptional heterogeneity through pathway and gene set overdispersion analysis. Nat. Methods *13*, 241–244. https://doi.org/10.1038/nmeth.3734.

88. Street, K., Risso, D., Fletcher, R.B., Das, D., Ngai, J., Yosef, N., Purdom, E., and Dudoit, S. (2018). Slingshot: cell lineage and pseudotime inference for single-cell transcriptomics. BMC Genom. *19*, 477. https://doi.org/10.1186/s12864-018-4772-0.

89. Korsunsky, I., Millard, N., Fan, J., Slowikowski, K., Zhang, F., Wei, K., Baglaenko, Y., Brenner, M., Loh, P.R., and Raychaudhuri, S. (2019). Fast, sensitive and accurate integration of single-cell data with Harmony. Nat. Methods *16*, 1289–1296. https://doi.org/10.1038/s41592-019-0619-0.

90. Workman, P., Aboagye, E.O., Balkwill, F., Balmain, A., Bruder, G., Chaplin, D.J., Double, J.A., Everitt, J., Farningham, D.A.H., Glennie, M.J., et al. (2010). Guidelines for the welfare and use of animals in cancer research. Br. J. Cancer *102*, 1555–1577. https://doi.org/10.1038/sj.bjc.6605642.

91. Drokhlyansky, E., Smillie, C.S., Van Wittenberghe, N., Ericsson, M., Griffin, G.K., Eraslan, G., Dionne, D., Cuoco, M.S., Goder-Reiser, M.N., Sharova, T., et al. (2020). The Human and Mouse Enteric Nervous System at Single-Cell Resolution. Cell *182*, 1606–1622.e23. https://doi.org/10.1016/j.cell.2020.08.003.

92. Sanjana, N.E., Shalem, O., and Zhang, F. (2014). Improved vectors and genome-wide libraries for CRISPR screening. Nat. Methods *11*, 783–784. https://doi.org/10.1038/nmeth.3047.

93. Brinkman, E.K., Chen, T., Amendola, M., and van Steensel, B. (2014). Easy quantitative assessment of genome editing by sequence trace decomposition. Nucleic Acids Res. *42*, e168. https://doi.org/10.1093/nar/gku936.

94. Miyaoka, Y., Chan, A.H., Judge, L.M., Yoo, J., Huang, M., Nguyen, T.D., Lizarraga, P.P., So, P.L., and Conklin, B.R. (2014). Isolation of single-base genome-edited human iPS cells without antibiotic selection. Nat. Methods *11*, 291–293. https://doi.org/10.1038/nmeth.2840.

95. Vinci, M., Burford, A., Molinari, V., Kessler, K., Popov, S., Clarke, M., Taylor, K.R., Pemberton, H.N., Lord, C.J., Gutteridge, A., et al. (2018). Functional diversity and cooperativity between subclonal populations of pediatric glioblastoma and diffuse intrinsic pontine glioma cells. Nat. Med. *24*, 1204–1215. https://doi.org/10.1038/s41591-018-0086-7.

96. Bozec, D., Sattiraju, A., Bouras, A., Jesu Raj, J.G., Rivera, D., Huang, Y., Junqueira Alves, C., Tejero, R., Tsankova, N.M., Zou, H., et al. (2020). Akaluc bioluminescence offers superior sensitivity to track *in vivo* glioma expansion. Neurooncol. Adv. *2*, vdaa134. https://doi.org/10.1093/noajnl/vdaa134.

97. Ernst, J., and Kellis, M. (2012). ChromHMM: automating chromatin-state discovery and characterization. Nat. Methods *9*, 215–216. https://doi.org/10.1038/nmeth.1906.

98. Chen, X., Li, X., Zhang, B., Xu, J., Wu, Z., Wang, B., Li, H., Younas, M., Huang, L., Luo, Y., et al. (2013). Detection and genotyping of restriction fragment associated polymorphisms in polyploid crops with a pseudo-reference sequence: a case study in allotetraploid Brassica napus. BMC Genom. *14*, 346. https://doi.org/10.1186/1471-2164-14-346.

99. Pidsley, R., Zotenko, E., Peters, T.J., Lawrence, M.G., Risbridger, G.P., Molloy, P., Van Djik, S., Muhlhausler, B., Stirzaker, C., and Clark, S.J. (2016). Critical evaluation of the Illumina MethylationEPIC BeadChip microarray for whole-genome DNA methylation profiling. Genome Biol. *17*, 208. https://doi.org/10.1186/s13059-016-1066-1.

100. Paugh, B.S., Qu, C., Jones, C., Liu, Z., Adamowicz-Brice, M., Zhang, J., Bax, D.A., Coyle, B., Barrow, J., Hargrave, D., et al. (2010). Integrated molecular genetic profiling of pediatric high-grade gliomas reveals key differences with the adult disease. J. Clin. Oncol. *28*, 3061–3068. https://doi.org/10.1200/JCO.2009.26.7252.

101. Paugh, B.S., Broniscer, A., Qu, C., Miller, C.P., Zhang, J., Tatevossian, R.G., Olson, J.M., Geyer, J.R., Chi, S.N., da Silva, N.S., et al. (2011). Genome-wide analyses identify recurrent amplifications of receptor tyrosine kinases and cell-cycle regulatory genes in diffuse intrinsic pontine glioma. J. Clin. Oncol. *29*, 3999–4006. https://doi.org/10.1200/JCO.2011.35.5677.

102. Bender, S., Tang, Y., Lindroth, A.M., Hovestadt, V., Jones, D.T.W., Kool, M., Zapatka, M., Northcott, P.A., Sturm, D., Wang, W., et al. (2013). Reduced H3K27me3 and DNA hypomethylation are major drivers of gene expression in K27M mutant pediatric high-grade gliomas. Cancer Cell *24*, 660–672. https://doi.org/10.1016/j.ccr.2013.10.006.

103. Griesinger, A.M., Birks, D.K., Donson, A.M., Amani, V., Hoffman, L.M., Waziri, A., Wang, M., Handler, M.H., and Foreman, N.K. (2013). Characterization of distinct immunophenotypes across pediatric brain tumor types. J. Immunol. *191*, 4880–4888. https://doi.org/10.4049/jimmunol.1301966.

104. Pajtler, K.W., Wei, Y., Okonechnikov, K., Silva, P.B.G., Vouri, M., Zhang, L., Brabetz, S., Sieber, L., Gulley, M., Mauermann, M., et al. (2019). YAP1 subgroup supratentorial ependymoma requires TEAD and nuclear factor I-mediated transcriptional programmes for tumorigenesis. Nat. Commun. *10*, 3914. https://doi.org/10.1038/s41467-019-11884-5.

105. Joung, J., Konermann, S., Gootenberg, J.S., Abudayyeh, O.O., Platt, R.J., Brigham, M.D., Sanjana, N.E., and Zhang, F. (2017). Genome-scale CRISPR-Cas9 knockout and transcriptional activation screening. Nat. Protoc. *12*, 828–863. https://doi.org/10.1038/nprot.2017.016.

106. Gojo, J., Englinger, B., Jiang, L., Hübner, J.M., Shaw, M.L., Hack, O.A., Madlener, S., Kirchhofer, D., Liu, I., Pyrdol, J., et al. (2020). Single-Cell RNA-Seq Reveals Cellular Hierarchies and Impaired Developmental Trajectories in Pediatric Ependymoma. Cancer Cell *38*, 44–59.e9. https://doi.org/10.1016/j.ccell.2020.06.004.

107. Hovestadt, V., Smith, K.S., Bihannic, L., Filbin, M.G., Shaw, M.L., Baumgartner, A., DeWitt, J.C., Groves, A., Mayr, L., Weisman, H.R., et al. (2019). Resolving medulloblastoma cellular architecture by single-cell genomics. Nature *572*, 74–79. https://doi.org/10.1038/s41586-019-1434-6.

108. Dempster, J.M., Boyle, I., Vazquez, F., Root, D.E., Boehm, J.S., Hahn, W.C., Tsherniak, A., and McFarland, J.M. (2021). Chronos: a cell population dynamics model of CRISPR experiments that improves inference of gene fitness effects. Genome Biol. *22*, 343. https://doi.org/10.1186/s13059-021-02540-7.

109. Blomen, V.A., Májek, P., Jae, L.T., Bigenzahn, J.W., Nieuwenhuis, J., Staring, J., Sacco, R., van Diemen, F.R., Olk, N., Stukalov, A., et al. (2015). Gene essentiality and synthetic lethality in haploid human cells. Science *350*, 1092–1096. https://doi.org/10.1126/science.aac7557.

110. Hart, T., Brown, K.R., Sircoulomb, F., Rottapel, R., and Moffat, J. (2014). Measuring error rates in genomic perturbation screens: gold standards for human functional genomics. Mol. Syst. Biol. *10*, 733. https://doi.org/10.15252/msb.20145216.

111. Stuart, T., Butler, A., Hoffman, P., Hafemeister, C., Papalexi, E., Mauck, W.M., 3rd, Hao, Y., Stoeckius, M., Smibert, P., and Satija, R. (2019). Comprehensive Integration of Single-Cell Data. Cell *177*, 1888–1902.e21. https://doi.org/10.1016/j.cell.2019.05.031.

112. Hao, Y., Hao, S., Andersen-Nissen, E., Mauck, W.M., 3rd, Zheng, S., Butler, A., Lee, M.J., Wilk, A.J., Darby, C., Zager, M., et al. (2021). Integrated analysis of multimodal single-cell data. Cell *184*, 3573–3587.e29. https://doi.org/10.1016/j.cell.2021.04.048.

113. Tran, H.T.N., Ang, K.S., Chevrier, M., Zhang, X., Lee, N.Y.S., Goh, M., and Chen, J. (2020). A benchmark of batch-effect correction methods for single-cell RNA sequencing data. Genome Biol. *21*, 12. https://doi.org/10.1186/s13059-019-1850-9.

114. Van de Sande, B., Flerin, C., Davie, K., De Waegeneer, M., Hulselmans, G., Aibar, S., Seurinck, R., Saelens, W., Cannoodt, R., Rouchon, Q., et al. (2020). A scalable SCENIC workflow for single-cell gene regulatory network analysis. Nat. Protoc. *15*, 2247–2276. https://doi.org/10.1038/s41596-020-0336-2.

STAR★METHODS

KEY RESOURCES TABLE

REAGENT or RESOURCE	SOURCE	IDENTIFIER
Antibodies		
rabbit anti-SOX2 mAb (D6D9)	Cell Signaling Technologies	Cat# 3579; RRID: AB_2195767
rabbit anti-CDK6 mAb (D4S8S)	Cell Signaling Technologies	Cat# 13331; RRID: AB_2721897
anti-human nuclei Ab	Millipore	Cat# MAB4383; RRID: AB_827439
rabbit anti-Vinculin XP® mAb (E1E9V)	Cell Signaling Technologies	Cat# 13901; RRID: AB_2728768
rabbit anti-GABA pAb	Sigma Aldrich	Cat# A2052; RRID: AB_477652
rabbit anti-GAD67 pAb	Millipore	Cat# MAB5406; RRID: AB_2278725
rabbit anti-Histone H3.3 G34R (clone RM240)	RevMAb Biosciences	Cat# 31-1120-00; RRID: AB_2716433
mouse anti-Histone H3.3 G34V	Synaptic Systems	Cat# HS-388 011; RRID: AB_2661878
rabbit anti-Histone H3K36me3 pAb	Active Motif	Cat# 61101: RRID: AB_2615073
rabbit anti-Histone H4 pAb	Active Motif	Cat# 61299; RRID: AB_2650524
Pacific Blue anti-SOX2 antibody (Lot B330632)	Biolegend	Cat# 656112; RRID: AB_2566189
Alexa-Fluor 647 Mouse anti-TUBB3 antibody (Lot B321962)	Biolegend	Cat# 801210; RRID: AB_2686931
Anti-STMN2 pAb	Thermo Fisher	Cat# 720178; RRID: AB_2606219
mouse anti-VGAT	Synaptic Systems	Cat# 131003; RRID: AB_887869
α-Tubulin (DM1A) Mouse mAb	Cell Signaling Technologies	Cat# 3873; RRID: AB_1904178
β-Actin (8H10D10) Mouse mAb	Cell Signaling Technologies	Cat# 3700; RRID: AB_2242334
β3-Tubulin (D71G9) XP	Cell Signaling Technologies	Cat# 5568; RRID: AB_10694505
CDK6 (D4S8S) Rabbit mAb	Cell Signaling Technologies	Cat# 13331; RRID: AB_2721897
CRBN (D8H3S) Rabbit mAb	Cell Signaling Technologies	Cat# 71810; RRID: AB_2799810
Alexa Fluor 488-conjugated goat anti-mouse IgG	ThermoFisher	Cat# A11001; RRID: AB_2534069
Alexa Fluor 555-conjugated donkey anti-rabbit IgG	ThermoFisher	Cat# A31572; RRID: AB_162543
HRP-linked anti-rabbit IgG	Cell Signaling Technologies	Cat# 7074S; RRID: AB_2099233
HRP-linked anti-mouse IgG	Cell Signaling Technologies	Cat# 7076S; RRID: AB_330924
Anti-rabbit IgG (H+L), F(ab')2 Fragment (Alexa Fluor® 647 Conjugate)	Cell Signaling Technologies	Cat# 4414S; RRID: AB_10693544
Anti-mouse IgG (H+L), F(ab')2 Fragment (Alexa Fluor® 647 Conjugate)	Cell Signaling Technologies	Cat# 4410S; RRID: AB_1904023
Anti-rabbit IgG (H+L), F(ab')2 Fragment (Alexa Fluor® 488 Conjugate)	Cell Signaling Technologies	Cat# 4412S; RRID: AB_1904025
Anti-mouse IgG (H+L), F(ab')2 Fragment (Alexa Fluor® 488 Conjugate)	Cell Signaling Technologies	Cat# 4408S; RRID: AB_10694704
Anti-H3K36me3	Active Motif	Cat# 61101; RRID: AB_2615073
Anti-H3K27Ac	Active Motif	Cat# 39133; RRID: AB_2561016
Anti-PAX6	Abcam	Cat# ab78545; RRID: AB_1566562
Anti-RNA Pol II	Active Motif	Cat# 39097; RRID: AB_2732926
Anti-H3K9me3	Active Motif	Cat# 39161; RRID: AB_2532132
Anti-H3.3	Active Motif	Cat# 91191; RRID: AB_2793796
Anti-H3K27me3	Active Motif	Cat# 39155; RRID: AB_2561020
Anti-HOPX	Thermo Fisher	Cat# PA5-90538; RRID: AB_2806113
Anti-AQP4	Thermo Fisher	Cat# PA5-53234; RRID: AB_2638104
Anti-TUJ1	Biolegend	Cat# 801201; RRID: AB_2313773
Anti-Nestin	Biolegend	Cat# 656802; RRID: AB_2562474

(*Continued on next page*)

Continued

REAGENT or RESOURCE	SOURCE	IDENTIFIER
Anti-Ki67 Clone B56	BD Biosciences	Cat# 550609; RRID: AB_393778
Anti-DCX	Santa Cruz	Cat# sc-271390; RRID: AB_10610966
Bacterial and virus strains		
One Shot™ Stbl3™ Chemically Competent *E. coli*	ThermoFisher	Cat# C737303
Biological samples		
Tumors profiled by scRNA-seq/snRNA-seq and IF	Table S5	
Chemicals, peptides, and recombinant proteins		
Neurobasal-A Medium	Gibco	Cat# 11570556
NSA Working Medium	Stem Cell Technologies	Cat# 5751
DMEM/F12 with HEPES	Gibco	Cat# 11330057
Non Essential Amino Acids	Thermo Fisher	Cat# 363401
B27-minus A supplement	Biolegend	Cat# 328811
Human EGF	Shenandoah Biotech	Cat# 100-26
Human FGF	Shenandoah Biotech	Cat# 100-146
Human PDGF-BB	Shenandoah Biotech	Cat# 100-18
Human PDGF-AA	Shenandoah Biotech	Cat# 100-16
Heparin Solutino	Stem Cell Technologies	Cat# 7980
Mouse laminin	Thermo Fisher	Cat# 23017015
BrainPhys Neuronal Media	Stem Cell Technologies	Cat# 05790
Glutamax	Invitrogen	Cat# 35050-061
L-glutamine	Sigma	Cat# G8540
Akalumine-HCl/TokeOni	Bio-Techne Ltd	Cat# 6555
Geneticin/G418	Thermo Fisher	Cat# 10131035
Antibiotic-Antimycotic	Thermo Fisher	Cat# 15240062
Geltrex	Thermo Fisher	Cat# A1569601
Accutase	Thermo Fisher	Cat# A1569601
Sodium Pyruvate	Thomas Scientific	Cat# C809G58
Bovine Serum Albumin (BSA)	Biolegend	Cat# 644710
TCL Buffer	Qiagen	Cat# 1031576
Calcein AM	Life Technologies	Cat# 3100MP
TO-PRO3 iodide	Life Technologies	Cat# T3605
beta-mercaptoethanol	Sigma	Cat# M6250
Vybrant DyeCycle Ruby Stain	Life Technology	Cat# V10309
Dimethyl sulfoxide (DMSO)	Sigma	Cat# 276855
KAPA HiFi HotStart ReadyMix	Kapa Biosystems	Cat# KK2602
Maxima H Minus Reverse Transcriptase Recombinant	Life Technologies	Cat# EP0753
Recombinant RNAse Inhibitor (RRI)	Takara	Cat# 2313B
Betaine	Sigma	Cat# B0300
$MgCl_2$	Sigma	Cat# M1028
Agencourt RNAClean XP beads	Beckman	Cat# A63987
Agencourt AMPure XP beads	Beckman	Cat# A63881
Ribociclib	MedChemExpress	Cat# HY15777
Abemaciclib	MedChemExpress	Cat# HY16297A
Palbociclib	MedChemExpress	Cat# HY50767
BSJ-03-123 (PROTAC CDK6 degrader)	MedChemExpress	Cat# HY111556
Recombinant Cas9 protein	QB3 Macrolab	N/A
Recombinant HiFiCas9	Integrated DNA Technologies	Cat# 1801060
Recombinant NLGN3	Origene	Cat# TP307955
Recombinant BDNF	Shenandoah Biotech	Cat# 100-01-10

(*Continued on next page*)

Continued

REAGENT or RESOURCE	SOURCE	IDENTIFIER
Critical commercial assays		
Click-iT Plus EdU kit	ThermoFischer	Cat# C10337
True-Nuclear^{tm} Transcription Factor Buffer Set	Biolegend	Cat# 424401
RNAeasy plus Mini kit (50)	Qiagen	Cat# 74134
Opal Polaris 7 Color Manual IHC Detection Kit	Akoya Biosciences	Cat# OP-000003
Pierce™ BCA Protein Assay Kit	ThermoFisher	Cat# 23227
Neural Tissue Dissociation Kit	Miltenyi Biotech	Cat# 130-092-628
Neuron Isolation Kit	Miltenyi Biotech	Cat# 130-115-389
Brain Tumor Dissociation Kit	Miltenyi Biotech	Cat# 130-095-942
CellTiter-Glo assay	Promega	Cat# G7571
3D CellTiter-Glo assay	Promega	Cat# G9682
ONE-Glo EX Luciferase assay	Promega	Cat# E8110
Nextera XT DNA Library Preparation Kit	Illumina	Cat# FC-131-1096
NextSeq 500/550 High Output Kit v2.5 (75 Cycles)	Illumina	Cat# 20024906
Qubit dsDNA HS Assay Kit	Thermo Fisher Scientific	Cat# Q32854
Mycoplasma Stain Kit	Sigma	Cat# MP0025
Penicillin/Streptomycin	Thermo Fisher Scientific	Cat# 15140148
Deposited data		
ChIP-seq data	Gene Expression Omnibus (GEO)	GSE272262
Bulk RNA-seq data	GEO	GSE272261
scRNA-seq data of patient tumors	GEO	GSE162989
Original Western blot images	Mendeley	https://doi.org/10.17632/z9mhzbd3nr
Tumor RNA-seq data (Wu et al., 2012)[3]	EGA	EGAS00001000192
Tumor RNA-seq data (Krug et al., 2019)[22]	GEO	GSE117446
H3K27ac ChIP-seq data (Krug et al., 2019)[22]	GEO	GSE117446
DNA methylation microarray data (Capper et al., 2018)[84]	GEO	GSE109379
DNA methylation microarray data (Capper et al., 2018)[84]	GEO	GSE90496
DNA methylation microarray data (Sturm et al., 2016)[85]	GEO	GSE73801
DNA methylation microarray data (Mackay et al., 2017)[18]	EMBL-EBI	E-MTAB-5528
10x scRNA-seq data (Chen et al., 2020)[19]	EGA	EGAS00001004301
Human neural stem cell transcriptomes (Bressan et al., 2021)[20]	GEO	GSE163044
Experimental models: Cell lines		
OPBG-GBM-001 (H3.3G34R)	M.Vinci Lab, Rome	
HSJD-GBM-002 (H3.3.G34R)	A.Carcaboso lab, Barcelona	
KNS42 (H3.3G34V)	Japanese Collection of Research Bioresources Cell Bank	
CHOP-GBM-001(H3.3.G34R)	Children's Brain Tumour Tissue Consortium	
HEK293FT	ATCC	RRID: CVCL_6911
HSJD-GBM-001 (H3WT)	A.Carcaboso lab, Barcelona	
BT869 (H3.3K27M)	Boston Children's Hospital	
ICR-CXJ046	Institute of Cancer Research	
BT690	Boston Children's Hospital	
ICR-CXJ001	Institute of Cancer Research	
ICR-CXJ008	Institute of Cancer Research	

(*Continued on next page*)

Continued

REAGENT or RESOURCE	SOURCE	IDENTIFIER
ICR-CXJ015	Institute of Cancer Research	
SUDIPG45 (H3.3K27M)	M.Monje lab, Stanford	
SUpcGBM2 (H3WT)	M.Monje lab, Stanford	
Mouse OPC	M.Monje lab, Stanford	
Normal Human Astrocytes	LONZA	
Experimental models: Organisms/strains		
CD-1® IGS Mouse Details	Jihui Laboratory Animal Co. LTD	
NOD.Cg-Prkdc^{scid} Il2rg^{tm1Wjl}/SzJ (NOD *scid* gamma)	Charles River	
Oligonucleotides		
SOX2_gRNA_1	IDT (Table S6)	
SOX2_gRNA_2	IDT (Table S6)	
DLX1_gRNA_1	IDT (Table S6)	
DLX1_gRNA_2	IDT (Table S6)	
DLX2_gRNA_1	IDT (Table S6)	
DLX2_gRNA_2	IDT (Table S6)	
DLX5_gRNA_1	IDT (Table S6)	
DLX5_gRNA_2	IDT (Table S6)	
DLX6_gRNA_1	IDT (Table S6)	
DLX6_gRNA_2	IDT (Table S6)	
FOXG1_gRNA_1	IDT (Table S6)	
FOXG1_gRNA_2	IDT (Table S6)	
AURKA_gRNA_1	IDT (Table S6)	
AURKA_gRNA_2	IDT (Table S6)	
CDK6_gRNA_1	IDT (Table S6)	
CDK6_gRNA_2	IDT (Table S6)	
GAD1_gRNA_1	IDT (Table S6)	
GAD1_gRNA_2	IDT (Table S6)	
H3F3A gRNA_A	TTTCTTCACCCCTCCAGTAG	
H3F3A gRNA_B	CGTTACAGGTATTAAAAAAC	
Primer H3F3A seq tag For-	TCGTCGGCAGCGTCAGATGT GTATAAGAGACAGTGCTGGT AGGTAAGTAAGGAGG	
Primer H3F3A seq tag Rev-	GTCTCGTGGGCTCGGAGATG TGTATAAGAGACAGTAAGCA GTAGTTAAGTGTTC	
Template-Switch Oligo (TSO)	Qiagen	Custom
Oligo dT primer	IDT	Custom
ISPCR primer	IDT	Custom
Recombinant DNA		
Human GeCKO v2 gRNA pooled library in lentiCRISPRv2	Addgene	Cat# 1000000048
pLenti-PGK-Venus-Akaluc	Addgene	Cat# 124701; RRID: Addgene_124701
pHIV-Luc-ZsGreen	Addgene	Cat# 39196
psPAX2	Addgene	Cat# 12260; RRID: Addgene_12260
pMD2.G	Addgene	Cat# 12259; RRID: Addgene_12259
Software and algorithms		
R	https://www.r-project.org	v4.1.1
Python	https://www.python.org	v3.6
FlowJo	BD Biosciences	v10.6.1

(*Continued on next page*)

Continued

REAGENT or RESOURCE	SOURCE	IDENTIFIER
Tracking of Indels by Decomposition (TIDE)	http://shinyapps.datacurators.nl/tide/	v3.2.0
MAGeCK 0.5.9.4	https://sourceforge.net/p/mageck/wiki/Home/	v0.5.9.4
GraphPad Prism 8	GraphPad Prism Software	RRID:SCR_002798
MNP DNA methylation-based classification of tumors of the central nervous system	https://www.molecularneuropathology.org/mnp	
CHOPCHOP	https://chopchop.cbu.uib.no	v3; RRID: SCR_015723
ImageJ	https://imagej.net/ij/	v2.1.0; RRID: SCR_003070
SnapGene	GSL Biotech LLC	
AxoGraph X	Axograph Scientific	
IGOR Pro 8	Wavemetrics	RRID: SCR_000325
NIS-Element Viewer	Nikon	
MACS3	https://github.com/macs3-project/MACS	v3.0.0
Cancer Dependency Map	Broad Institute	RRID: SCR_017655
Bowtie	http://bowtie-bio.sourceforge.net/bowtie2/index.shtml	v0.12.7
Rsem	Li and Dewey, 2011[86]	v1.2.19
STAR	https://github.com/alexdobin/STAR	v2.7.3a; RRID: SCR_04463
samtools	https://www.htslib.org/	v1.13
cellranger	https://www.10xgenomics.com/	v7.2.0
inferCNV	https://github.com/broadinstitute/infercnv	v1.10.1
Seurat	https://satijalab.org/seurat/install.html	v4.3.0
PAGODA2	Fan et al., 2016[87]	v1.0.10
NMF	https://doi.org/10.32614/CRAN.package.NMF	v0.26
Destiny	https://www.bioconductor.org/packages/release/bioc/html/destiny.html	v3.8.1
Slingshot	Street et al., 2018[88]	v2.2.1
SCENIC	Aibar et al., 2017[38]	v1.2.4
Harmony	Korsunsky et al., 2019[89]	v0.1.0
ClusterProfiler	https://bioconductor.org/packages/release/bioc/html/clusterProfiler.html	v3.18.0; RRID: SCR_016884
fgsea	https://bioconductor.org/packages/release/bioc/html/fgsea.html	v1.22.0
DESeq2	https://bioconductor.org/packages/release/bioc/html/DESeq2.html	v1.30.1; RRID: SCR_000154

RESOURCE AVAILABILITY

Lead contact

Further information and requests for resources and reagents should be directed to and will be fulfilled by the Lead Contact, Prof. Mariella Filbin (Mariella_GruberFilbin@dfci.harvard.edu).

Materials availability

The KNS42 sub-line containing only intact *H3F3A* wildtype alleles is available upon request.

Data and code availability

ChIP sequencing data for this study has been submitted to GEO and is accessible under GSE272262. Bulk RNA sequencing from patient-derived DHG-H3G34 tumor cell cultures and after CDK6-targeting are accessible under GSE272261. Single-cell RNA-sequencing data of primary patient tumors are accessible under GSE162989. All accession numbers as well as those of re-analyzed publicly available data are listed in the key resources table. Original Western blot images have been deposited at Mendeley and are publicly available as of the date of publication. The DOI is listed in the key resources table. Microscopy data reported in this paper will be shared by the lead contact upon request. All analysis pipelines, codes and publicly available packages are cited in the paper and

described in the STAR Methods section. The scRNA-seq pipeline can also be found at Zenodo under ID 7073167.[72] This study did not generate any original custom code. Any additional information required to reanalyze the data reported in this paper is available from the lead contact upon request.

EXPERIMENTAL MODEL AND STUDY PARTICIPANT DETAILS

Human patients and ethical considerations

All DHG-H3G34 tissues used in this study were de-identified and obtained with properly informed consent of patients and/or their legal representatives treated at Boston Children's Hospital, at the Medical University of Vienna, at Bambino Gesù Children's Hospital, Rome, or at the Royal Marsden Hospital, London. The study was approved by the respective local Institutional Review Board (IRB) under DFCI 10-417 (Boston Children's Hospital and Dana-Farber Cancer Institute), EK Nr. 1244/2016 (Medical University of Vienna), and 18/LO/0514 (Institute of Cancer Research, London). Clinical characteristics of the tumors profiled by scRNA-seq/snRNA-seq and IF are summarized in Table S5.

Animal studies

All animal studies were performed according to Dana-Farber Cancer Institute Institutional Animal Care and Use Committee (IACUC)-approved protocols, UK Home Office Animals (Scientific Procedures) Act 198 and the United Kingdom National Cancer Research Institute guidelines for the welfare of animals in cancer research,[90] and Stanford University Institutional Animal Care and Use Committee (IACUC) guidelines. For patient-derived xenograft knockout and drugging experiments, 4-6 week-old female NSG mice (NOD.Cg-*Prkdc*^{scid} *Il2rg*^{tm1Wjl}/SzJ, The Jackson Laboratory, Bar Harbor, ME) were used. For *in vivo* hyperexcitability experiments, NSG mice were used with male and female mice at an equal ratio. For pharmacokinetic and BBB penetration analyses, male CD1 (Jihui Laboratory Animal Co. LTD) mice at 6-8 weeks as well as female NSG mice at 6-8 weeks were used.

Cell lines

Patient-derived cultures OPBG-GBM-001 (H3.3G34R), HSJD-GBM-002 (H3.3G34R), ICR-CXJ046 (H3.3G34R), CHOP-GBM-001 (7316-158; H3.3G34R), HSJD-GBM-001 (H3.3-WT), ICR-CXJ001 (H3.3-WT), ICR-CXJ008 (H3.3-WT), ICR-CXJ015 (H3.3-WT), BT869 (H3.3K27M), SUDIPG45 (H3.3K27M), and SU-pcGBM2 (H3.3-WT) were grown in stem cell media consisting of Dulbecco's Modified Eagles Medium: Nutrient Mixture F12 (DMEM/F12), Neurobasal-A Medium, 10 mM HEPES Buffer Solution, 1 mM sodium pyruvate solution, 1% (v/v) non-essential amino acids solution (100x) and 1% (v/v) Glutamax-I supplement (100x). The media was supplemented with 2% (v/v) B-27 supplement minus vitamin A (50x), 20 ng/ml Human-EGF, 20 ng/ml Human-FGF-basic-154, 10 ng/ml Human-PDGF-AA, 10 ng/ml Human-PDGF-BB (all Shenandoah Biotech, Warwick, PA, USA) and 2 μg/ml Heparin Solution (Stem Cell Technologies, Cambridge, UK). Cells were cultured on Cultrex® 3D Culture Matrix Laminin (Bio-Techne Ltd) except for CHOP-GBM-001 cells, which were cultured on Geltrex (Invitrogen). Cells cultured as neurospheres were grown in cell culture flasks in suspension. KNS42 cells (H3.3 G34V) were obtained from the Japanese Collection of Research Bioresources Cell Bank (#IFO50356) and grown in DMEM/F12 with 10% (v/v) FBS. HEK293FT (RRID:CVCL_6911) cells were purchased from Invitrogen and grown in DMEM containing 10% (v/v) FBS. BT690 (H3.3G34R) were grown in NSA Working Media (Stem Cell Technologies, #5751), supplemented with 20 ng/ml Human-EGF and 20 ng/ml Human-FGF, and 2 μg/ml Heparin Solution. Cells were incubated at 37°C in a humidified atmosphere at 5% CO_2. Basic clinical characteristics of all DHG-H3G34 patient-derived cell lines used including sex and age are listed in Table S5.

METHOD DETAILS

Tumor tissue dissociation

To isolate whole cells from fresh tissues, tumor tissue acquired at the time of surgery was immediately processed by mechanical as well as enzymatic papain-based dissociation for 30 min at 37°C according to the Brain Tumor Dissociation Kit (Miltenyi Biotec) protocol. Single-cell suspensions were filtered through a 70 μm strainer, centrifuged at 300 x *g* for 10 min, and re-suspended in phosphate-buffered saline (PBS) supplemented with 1% bovine serum albumin (BSA) for subsequent fluorescence-activated cell sorting (FACS).

To extract intact single nuclei from frozen tissues, snap-frozen tumor tissue was disaggregated on ice in 1 ml of 0.49 % CHAPS detergent based nuclear extraction buffer, that was previously optimized for the lysis of brain tissue,[91] aided by mild chopping using sterile scissors. Single-nuclei suspensions were filtered using a 40 μm strainer, centrifuged at 500 x *g* for 5min, and re-suspended in PBS supplemented with 1% BSA.

Fluorescence-activated cell sorting (FACS)

Single-cell suspensions captured from fresh tumor tissue and re-suspended in PBS + 1% BSA were stained with 0.5 μM calcein AM (Life Technologies, C3100MP) and 0.33 μM TO-PRO3 iodide (Life Technologies, T3605) for 15 min at room temperature and subsequently placed on ice. Single-cell sorting was performed on a SH800 sorter (Sony) using 488 nm (calcein AM, 530/30 emission filter) and 633 nm (TO-PRO-3, 665/30 emission filter) lasers. Unstained and single-stained controls were included for all tumors. Viable cells were identified by positive staining for calcein AM and negative staining for TO-PRO-3. Doublet discrimination was performed by

stringent singlet-gating based on back scatter area (BSC-A) versus back scatter width (BSC-W) setting. Singlet, viable tumor cells were sorted into 96-well plates containing cold TCL buffer (Qiagen, 1031576), briefly spun down, snap frozen on dry ice, and then stored at -80°C.

Single-nuclei suspensions extracted from frozen tumor tissue and re-suspended in PBS + 1% BSA were stained with 0.5 μM Vybrant™ DyeCycle™ Ruby Stain (Invitrogen, V10309) immediately before FACS sorting. Unstained controls were included for all samples. Single-nucleus sorting was performed on a SH800 sorter using the 633 nm laser (Ruby Stain, 665/30 nm emission filter). Intact nuclei were selected by positive staining for Ruby Stain. Doublets were discriminated by singlet-gating in the Ruby Stain area versus Ruby Stain width setting. Singlet nuclei were sorted into 96-well plates containing pre-chilled TCL buffer and 1% beta-mercaptoethanol, briefly spun down, snap frozen on dry ice and stored at -80°C before processing for whole transcriptome amplification, library preparation and sequencing.

Immunofluorescence staining

Immunostaining experiments of patient tumors were performed in one experimental replicate, where the entire section was imaged. For IF staining of GABA, VGAT, and GAD67, $1.5x10^3$ cells per DHG-H3G34 cell line (OPBG-GBM-001, HSJD-GBM-002) and $1x10^3$ cells of immortalized Human Astrocytes NHA-hTERT were plated in Nunc™ Lab-Tek™ II Chamber Slides™ (ThermoFisher) coated with laminin. Cells were fixed at a confluency of ~70% in 4% paraformaldehyde in PBS for 15 min at room temperature (RT), followed by permeabilization in 0.2% Triton X-100 in PBS for 5 min at RT. After carefully washing twice with PBS, cells were blocked in a solution of PBS containing 5% BSA for 40 min at RT. Incubations with primary and secondary antibodies (diluted in 1x PBS/ 1% BSA / 0.3 % Triton X-100) were carried out overnight at 4°C and 1.5 h at room temperature, respectively. Primary antibodies used were GAD67 (Millipore Cat# MAB5406, RRID:AB_2278725, mouse, 1:1,000), VGAT (Synaptic Systems, Cat# 131003, RRID:AB_887869 mouse, 1:1,000) and GABA (Sigma Aldrich, Cat# A2052, RRID:AB_477652, rabbit, 1:500). Secondary antibodies used were anti-mouse-IgG (Alexa Fluor® 647 Conjugate – CST, Cat# 4410, RRID:AB_1904023), anti-rabbit-IgG (Alexa Fluor® 488 Conjugate – CST, Cat# 4412, RRID:AB_1904025). Cells were also stained for Dylight 554 Phalloidin (cytoskeleton) (CST, Cat# 13054, 1:200) and DAPI (nucleus) (CST #4083, final concentration 0.5 μg/ml). Imaging was performed on a Nikon Eclipse Ni C2 Si laser scanning upright confocal microscope with four laser lines (405, 488, 561, and 640 nm). Single plane multi-channel fluorescence images were acquired for each cell line with the following laser settings: DAPI (405 nm laser; HV=30, Offset=0, Laser Power=5.0), GABA (488 nm laser; HV=15, Offset=0, Laser Power=3.0), Phalloidin/f-Actin (561 nm laser; HV=35, Offset=0, Laser Power=5.0), GAD1 (640 nm laser; HV=40, Offset=0, Laser Power=5.0). Images were then exported to ImageJ (RRID_SCR_003070) for quantitative analysis.

For multiplexed IF staining and image analysis of patient DHG-H3G34 tissues, FFPE tissue sections were deparaffinized and rehydrated. Antigen retrieval was performed using a pressure cooker and 1x citrate buffer, pH 6.0. Subsequently, sections were stained using the Opal Polaris 7 Color Manual IHC Detection Kit (Akoya Biosciences). Image analysis was performed using inForm analysis software (Akoya Biosciences) and the open source software for digital pathology image analysis QuPath. The following primary antibodies were used at a 1:100 dilution: Anti-PAX6 antibody [AD2.38] (Abcam, Cat# ab78545, RRID:AB_1566562), Anti-Histone H3.3G34R Mutant rabbit monoclonal antibody [RM240] (Biozol, RMB-31-1120-00), Hopx Polyclonal Antibody (Thermo Fisher, PA5-90538), Aquaporin 4 Polyclonal Antibody (Thermo Fisher, PA5-53234), Purified anti-SOX2 Antibody [14A6A34] (Biolegend, Cat# 656102, RRID:AB_2562246), Purified anti-Tubulin β 3 (Biolegend, Cat# 801201, RRID:AB_2313773), Anti-GABA Antibody (Sigma Aldrich, Cat# A2052, RRID:AB_477652), STMN2 Polyclonal Antibody (Thermo Fisher, Cat# 720178, RRID:AB_2606219), Doublecortin Antibody (E-6) (Santa Cruz, Cat# sc-271390, RRID:AB_10610966), Purified anti-Nestin (Biolegend, Cat# 656802, RRID:AB_2562474) and Purified Mouse Anti-Ki-67 Clone B56 (BD Biosciences, Cat# 550609, RRID:AB_393778).

Lentivirus production

The human GeCKOv2 CRISPR knockout pooled library (123411 sgRNAs), kindly provided by Dr. Feng Zhang (Addgene #1000000048),[92] was transfected with lipofectamine 3000 into HEK293FT (RRID:CVCL_6911) cells along with psPAX2 (Addgene #12260, RRID:Addgene_12260) and pMD2.G plasmids (Addgene #12259, RRID:Addgene_12259) to produce lentivirus. Approximately 5 h after transfection, media was replaced with fresh media. Lentivirus supernatant was harvested 72 h post-transfection and filtered using 0.45 μM steriflip filter unit (Merck). Lentivirus was concentrated using Lenti-X concentrator solution (Clontech) and stored at -80°C.

GeCKOv2 CRISPR-Cas9 genome-wide screens

OPBG-GBM-001 genome-wide screens were performed using two biological replicates and a minimum of $2x10^8$ cells seeded onto laminin coated T225 flasks. Cells were transduced at a MOI of <0.3 with the human GeCKOv2 library (123,411 sgRNAs[92]), in the presence of polybrene 4 ug/ml, for a minimum of 500-fold coverage. Media was refreshed 16 h post-transduction and cells were incubated for a further 48 h. Media was then replaced with fresh media containing 1.25 ug/ml puromycin and cells were incubated for 144 h to allow for efficient gene-editing. At this point (9 days post-transduction) T0 samples were collected and stored at -80°C for later processing. The remaining cells were cultured for a further 10 doublings (30 days) at 500-fold coverage in the absence of antibiotics, fresh media was added to cells every 2-3 days and cells were passaged once a week. T10 samples (10 doublings) were collected and stored at -80°C for genomic DNA extraction.

Avana CRISPR-Cas9 genome-wide screen

Genome-wide CRISPR-Cas9 knockout screening of KNS42 cells was performed at the Broad Institute as part of Project Achilles using the Avana sgRNA library (74,687 sgRNAs)[60,61] and is accessible via The Cancer Dependency Map (DepMap) platform (https://depmap.org/portal/). Briefly, cells were transduced at low MOI (<1) in 3 technical replicates and selected with puromycin and blasticidin for 7 days. The cells were then passaged without selection for 21 days maintaining a 500-fold coverage per sgRNA. Genomic DNA was extracted from end-point cell pellets, PCR amplified and sequenced with standard Illumina machines and protocols.

CRISPR-Cas9 screen validations

Multiple guide RNAs (gRNA) were designed using the publicly available tool CHOPCHOP (RRID:SCR_015723) (https://chopchop.cbu.uib.no). Single-stranded, homology-directed repair (HDR) oligonucleotide templates were designed using SnapGene software (GSL Biotech LLC, Chicago, IL). crRNA, HDR templates, and tracrRNA were obtained from Integrated DNA Technologies (Coralville, IA). crRNA and tracrRNA (200 μM each) were co-incubated to form guide RNA (gRNA) complexes (95°C for 5 minutes) according to the manufacturer's instructions. gRNA complexes were incubated with 20 μM recombinant Cas9 protein (QB3 Macrolab, University of California Berkeley, Berkeley, CA) at 37°C for 15 minutes to assemble ribonucleoprotein (RNP) complexes. RNP complexes (3 μl) were electroporated into 5x10^5 OPBG-GBM-001, HSJD-GBM-002 and KNS42 cells in 20 μl of SE "X" nucleofection buffer using a 4D- Nucleofector X unit 16-well nucleocuvette (Lonza Group LTD, Basel, Switzerland) with program DS-150. After nucleofection, cells were equilibrated in pre-warmed rescue media and plated into 6-well and 96-well plates. Cell viability was assessed at days 4, 7, and 12 post nucleofection using CellTiter-Glo assay (Promega, Madison, WI). Single-gene knockout efficiency was validated on genomic DNA or protein levels using Tracking of Indels by Decomposition (TIDE) or Western blot analysis (see below). For statistical analysis, two-tailed t-test was performed and statistical significance was defined as p-value <0.05. Data was analyzed with GraphPad Prism 9 software, and all error bars represent standard error of the mean (SEM) otherwise noted.

CRISPR knockout efficiency assessment using Tracking of Indels by Decomposition (TIDE) analysis

Genomic DNA was extracted from electroporated cells at the identical time points at which viability was assessed. Genomic regions of interest were amplified by polymerase chain reaction (PCR). PCR products were purified from 1% agarose gels using MinElute Gel Extraction columns (Qiagen) and the DNA Clean & Concentrator kit (Zymo Research). Purified PCR products were analyzed by Sanger sequencing (Quintarabio). The efficiency of Cas9-mediated gene editing was determined by comparing DNA sequences from target gene-specific gRNA-nucleofected cells versus unedited controls (noRNP, Cas9 only, and *AAVS1*) using Tracking of Indels by Decomposition (TIDE) analysis.[93]

Western blot analysis

5x10^5 cells were seeded in 6-well plates in at least three independent biological replicates. At indicated time points, cells were pelleted, washed once with ice-cold PBS, and lysed on ice for 20 min using RIPA buffer (Sigma) containing protease and phosphatase inhibitors (PhosSTOP, cOmplete ULTRA, PMSF; Sigma). Whole cell protein lysates were obtained by centrifugation for 15 min at 18,000x*g* at 4°C. Protein quantification was performed using Pierce™ BCA Protein Assay Kit (Thermo Fisher). Sodium dodecyl sulfate polyacrylamide gel electrophoresis (SDS-PAGE) was performed to separate whole-cell protein extracts, using 4X Laemmli Sample Buffer (Bio-Rad, Hercules, CA) and PageRuler™ Plus Prestained Protein Ladder (Thermo Fisher). Proteins were transferred onto polyvinylidene difluoride (PVDF) membranes (Sigma). Primary antibodies SOX2 (D6D9) XP® (CST, Cat#3579, RRID:AB_2195767) Rabbit mAb, CDK6 (D4S8S) (CST, Cat#13331, RRID:AB_2721897) Rabbit mAb, and Vinculin (E1E9V) XP® (CST, Cat#13901, RRID:AB_2728768) Rabbit mAb, were purchased from Cell Signaling Technology (CST). The Horseradish peroxidase (HRP)-linked secondary antibodies anti-rabbit IgG (7074S) (CST, Cat#7074, RRID:AB_2099233) and anti-mouse IgG (7076S) (CST, Cat#7076, RRID:AB_330924) were also purchased from CST. Primary antibodies were diluted 1:1,000 in Tris-buffered saline (TBS) containing 0.1% Tween-20 (Sigma) (TBS-T) and 3% BSA (Sigma) or 3% skim milk. Membranes were incubated with primary antibodies overnight at 4°C. Secondary antibodies were diluted 1:2,500 to 1:10,000 in TBS-T containing 3% BSA or 3% skim milk and incubated for 1 h at room temperature. Blots were developed using Pierce™ ECL Western Blotting Substrate (Thermo Fisher) and imaged using Amersham Imager 680 (GE Healthcare, Chicago, IL).

Flow cytometry

Cell cycle analysis

For cell cycle analysis with propidium iodide (PI), neurosphere cells were fixed after the cells were pelleted and dissociated with Accutase. Cells were fixed with 70% ethanol and stored at -20°C until labelled with PI. Next, fixed cells were rinsed with 1 ml cold PBS and pelleted. Supernatant was removed and replaced with cold PBS containing 40 μg/ml PI (SIGMA; P4864) and 100 μg/ml RNAse A (ThermoFisher Scientific; EN0531). Cells were stored at 4°C overnight, then read on a BD Biosciences BDLSRII Analyzer.

Cell cycle profile analysis using the Click-iT™ Plus EdU flow cytometry kit assay (ThermoFisher C10337) were performed according to the manufacturer's instructions. DMSO/drug treated cells during predicted log phase growth were pulsed with 10 μM of the modified nucleotide analogue EdU (5-ethynyl-2'-deoxyuridine) for 24 hours in an incubator at 37°C, >95% and 5% carbon dioxide. Primary cells were harvested, washed, fixed and permeabilized. Further, fixed cells were incubated with a cocktail containing Alexa Fluor 647 or Alexa Fluor 488 pycolyl azide for labeling. For DNA content staining, the FxCycle™ Violet Stain was used.

Flow cytometry for identification of SOX2 and TUBB3 positive cells

Intracelullar staining of TUBB3 and intranuclear staining of SOX2 were performed with the Fix/Perm Buffer and True-Nuclear™ Transcription Factor Buffer Set (Biolegend 424401), respectively, according to the manufacturer's protocol. The following conjugated antibodies were used for the intracellular and intranuclear flow cytometry assay: Pacific Blue™ anti-SOX2 (Biolegend, Cat #656112, RRID:AB_2566189, 1:1,000) and Alexa Fluor® 647 anti-Tubulin β3 (Biolegend, Cat# 801210, RRID:AB_2686931). Analytical experiments were performed using a BD FACSCelesta™ (BD Biosciences) analyzer. Isotype and unstained controls were used.

Chromatin lysate preparation and nucleosome IP

Generation of HEK293T (RRID:CVCL_0063) cells expressing wildtype, G34V or G34R mutant H3.3 with a V5-tag were described in our previous work.[17] Cells were harvested by centrifugation and washed in PBS before lysis in Buffer A (10mM Tris-HCl pH 7.5, 10 mM KCl, 1.5 mM $MgCl_2$, 0.34 M sucrose, 10% glycerol, 0.2% Triton X-100, 1 mM DTT and EDTA-free protease inhibitor cocktail (Roche)). Cell nuclei were pelleted and subsequently lysed to collect chromatin in Buffer B (3 mM EDTA, 0.2 mM EGTA, 1mM DTT and protease inhibitor cocktail). Pelleted chromatin was resuspended in Buffer A supplemented with 2 mM $CaCl_2$ and digested with 1 unit of MNase (Sigma) at 37°C for 5 min. MNase digestion was stopped by adding 5 μL of 0.2 M EGTA. Ion concentration was increased to 150 mM NaCl and 0.5% detergent (IGEPAL CA-630, Sigma). Digested chromatin preparations were bound to pre-cleared anti-V5 conjugated affinity gel (Sigma-Aldrich, clone V5-10) overnight at 4°C. Bound samples were washed with buffer (TBS, 0.5% Triton X-100, 0.5 mM EDTA, protease inhibitors) then released from the matrix after adding 2x Tricine SDS sample buffer (Invitrogen) and incubating at 95°C for 5 min. Equal sample volumes were loaded onto a 16% Tricine gel (Invitrogen) and gels were transferred to nitrocellulose membranes (Invitrogen) and probed with anti-H3K36me3 (Active Motif, Cat# 61101, RRID:AB_2615073) and anti-H4 antibodies (Active Motif).

CRISPR mediated gene editing of KNS42 cells

KNS42 cells were transfected with a plasmid expressing dual guide RNAs targeting *H3-3A*/*H3F3A* and Cas9-D10A nickase (ATUM). Guides were selected using the German Cancer Research Center E-CRISP (RRID: SCR_019088) webtool (http://www.e-crisp.org/E-CRISP/). Guide sequences used were: H3F3A gRNA_A – TTTCTTCACCCCTCCAGTAG; H3F3A gRNA_B – CGTTACAGGTATTA AAAAAC. Briefly, cells were seeded in 6-well plates and transfected 24 hours later with lipid complexes containing the CRISPR plasmid using 0.3% (vol/vol) final Lipofectamine 2000 (Invitrogen). After 72 h cells were sorted to identify cells co-expressing red fluorescent protein (RFP) with the Cas9-D10A nickase from the plasmid using a BD FACSAriaII (BD Biosciences). The RFP positive cells identified were expanded for approximately three doubling times (one week) under standard conditions (37°C, 5% CO2). At this point cells were sorted again. RFP negative cells were sorted as single cells into 96-well plates and grown for 6 weeks under standard conditions (37°C, 5% CO2). Sub-lines that grew from the single cells were replica plated to produce two 96-well plates and genomic DNA was isolated directly from all samples as previously described.[94] First round PCR amplification was performed using tailed primers specific to *H3F3A*. Primer sequences used were: H3F3A seq tag For-TCGTCGGCAGCGTCAGATGTGTATAAGA GACAGTGCTGGTAGGTAAGTAAGGAGG; H3F3A seq tag Rev-GTCTCGTGGGCTCGGAGATGTGTATAAGAGACAGTAAGCAG TAGTTAAGTGTTC (Integrated DNA Technologies, custom synthesis). Second round PCR added a unique index to each sample using the NexteraXT index kit V2 set A (Illumina). Sub-line DNA samples were sequenced as an indexed pool on a MiSeq System (Illumina) using a V2 Nano chip (Illumina) per standard manufacturer protocols. Sequence data was parsed and binned by primer index, then aligned to evaluate the wild-type and edited alleles. A KNS42 sub-line was identified that produced no reads containing the G34V mutation with retention of wild-type reads.

Drug screen

A minimum of $1.75x10^7$ cells was screened in 384-well plates containing eight concentrations (0.5, 1, 5, 10, 50, 100, 500, 1000 nM) of each of the drugs assayed, as described previously.[95] Cells were seeded at 1,500 cells per well and continuously cultured in the presence of drugs for five days, after which cell viability was estimated by the use of 3D CellTiter-Glo reagent (Promega, Cat#G9682). Luminescence values from each well in the 384-well plate were normalized to the median of signals from wells containing cells exposed to the drug vehicle, DMSO, generating Surviving Fractions (SF). High-throughput drug screening data was also pre-processed and normalized with the cellHTS2 package in R to produce dose-response curves and Z-scores. R-package drc was used to calculate area under the curve (AUC) values from dose-response curves. AUC values for each drug in each cell line were standardized generating Z scores to allow for comparisons to be made between cell lines.

Extended drugging assays with CDK4/6 inhibitors and CDK6 degrader

Cells were plated at 1,000 cells/well in 384-well plates, and exposed to four rounds of treatment with either ribociclib, abemaciclib, palbociclib, or BSJ-03-123, at 0, 0.008, 0.024, 0.08, 0.17, 0.45, 0.96, 3, 8, and 10 μM concentrations of each of the drugs assayed over an extended interval on days 3, 7, 10, and 14 post-plating. Cell viability was assessed using CellTiter-Glo (Promega, Cat#G9682) on day 17 post-plating from at least two independent experiments, performed in triplicate for each condition.

NLGN3 and BDNF proliferation experiments

In vitro proliferation assays were performed as described previously.[56] 8-well chamber slides (Ibidi Cat#80841) were first coated with poly-L-lysine (Sigma Cat#P8920) and 5 μg/mL mouse laminin (Thermo Fisher Cat#23017015). Cells (SU-DIPGVI and

HSJD-GBM-002) were seeded at 20,000 cells per well in Tumor Stem Medium (TSM) base without growth factors and were starved in this way for 24h. After 24h, one-third of medium was removed and was replaced by TSM base containing 30 μM EdU (10 μM final) and either 300 nM recombinant NLGN3 (100 nM final, OriGene Cat#TP307955), 300 nM recombinant BDNF (100 nM final, Shenandoah Cat#100-01-10), or corresponding vehicle. 24h following treatment, cells were fixed with 4% paraformaldehyde and stained using the Click-iT EdU kit and protocol (Thermo Fisher Cat#C10337). Slides were imaged by confocal microscopy at 20X magnification, images were blinded, and proliferation index was quantified by determining the percentage of EdU labeled cells. Each experiment consisted of 2 wells per condition and was replicated 3 times.

Neuron-glioma co-culture proliferation assays

Neurons were isolated from the brains of P0 or P1 CD1 mice using the Neural Tissue Dissociation Kit and the Neuron Isolation Kit (Miltenyi Cat#130-092-628, 130-115-389). After isolation, 200,000 neurons were plated onto glass coverslips pre-coated with poly-L-lysine (Sigma Cat#P8920) and 5 μg/mL mouse laminin (Thermo Fisher Cat#23017015). On DIV0, neurons were cultured in BrainPhys Neuronal Media (STEMCELL Tech Cat#05790) supplemented with Glutamax (Invitrogen 35050-061), β-mercaptoethanol (Tocris Cat#2906), 2% fetal bovine serum (Thermo Fisher 10-437-028), penicillin/streptomycin (Thermo Fisher Cat#15140148), SM1 supplement (STEMCELL Tech Cat#05711), 10 ng/mL BDNF (Shenandoah Cat#100-01-10), 5 ng/mL GDNF (Shenandoah Cat#200-37-10), and 5uM TRO19622 (Tocris Cat#2906). On DIV1 and DIV3, half the media was replenished and 1 uM UFDU (Sigma F0503, Cat#U3750) was added. On the morning of DIV5, half the media was replaced serum-free and without UFDU. In the afternoon of DIV5, another serum-free half media change without UFDU was performed with the addition of 50,000 glioma cells (HSJD-GBM-002, SU-DIPG13FL) per well. On DIV7, a final serum-free half media change was performed with 20 μM EdU (10 μM final). After 24h in EdU, co-cultures were fixed with 4% paraformaldehyde in PBS and stained using the Click-iT EdU kit and protocol (Thermo Fisher Cat#C10337) for proliferation analyses. To obtain a baseline proliferation rate of glioma cells without neural input, 50,000 cells were plated in BrainPhys Neuronal Media as described above with 0.5% fetal bovine serum. 10 μM EdU was added 48 hours later for the final 24h before fixation. Cover slips were imaged by confocal microscopy at 20X magnification, images were blinded, and proliferation index was quantified by determining the percentage of EdU labeled glioma cells. Each experiment consisted of 3 wells per condition and was replicated 3 times.

In vivo orthotopic DHG-H3G34 knockout xenograft models

HSJD-GBM-002 neurosphere cells, stably expressing luciferase, were dissociated and nucleofected to knockout *SOX2, DLX2, DLX5, CDK6* or *AAVS1* negative control guide RNA using CRISPR-Cas9 as described above. Prior to injections, luciferase expression was confirmed using the ONE-Glo EX Luciferase Assay System (Promega Cat#E8110). 12 hours post-nucleofection, cells were injected stereotactically into the right hemisphere of 4-6 week-old female NSG mice (NOD.Cg-*Prkdc*^{scid} *Il2rg*^{tm1Wjl}/SzJ, The Jackson Laboratory, Bar Harbor, ME) treated with buprenorphine 0.05mg/kg and anesthetized with isoflurane 2–3%. The skull of the mouse was exposed through a small skin incision, and a small burr hole was made using a 25-gauge needle at the selected stereotactic coordinates zeroed on lambda: -2.0 mm X, +1.0 mm Y and 2.5 mm Z. HSJD-GBM-002 cells (300,000 cells in 3μL PBS per mouse, n=6 per group, for *SOX2, DLX2, DLX5* vs. *AAVS1*) or BT690 cells (300,000 cells in 3μL PBS per mouse, n=6 per group, for *CDK6* vs. *AAVS1*) were loaded into a 33-gauge Hamilton syringe, and injected at a rate of 0.5 μl/min with use of an infusion pump. Upon completing injection, the needle was left in place for another minute, then withdrawn slowly to help reduce cell reflux. After closing the scalp with suture and staple, mice were returned to their cages placed on a warming pad and visually monitored until full recovery. Mice were then checked daily for signs of distress, including seizures, weight loss, and tremors, and euthanized as they developed neurological symptoms, including head tilt, seizures, sudden weight loss, loss of balance, and/or ataxia.

In vivo orthotopic DHG-H3G34 inducible *CDK6* knockdown xenograft models

DHG-H3G34 BT690 cells expressing a plasmid for stable luciferase expression were transduced with a doxycycline Tet-ON inducible short hairpin RNA (shRNA) vector for scramble negative control and *CDK6* knockdown, and further selected with puromycin treatment. CDK6 protein depletion was confirmed via Western blot (Figure S5M), and the cells were injected into the right cerebral hemispheres of female NOD SCID mice (4-6 weeks, 6 mice per group) at a density of 3 x 10^5 cells. The mouse skull was exposed through a small skin incision, and a small burr hole was made using a 25-gauge needle at the selected stereotactic coordinates zeroed on lambda: -2.0 mm X, +1.0 mm Y and 2.5 mm Z. BT690 cells (300,000 cells in 3μL PBS per mouse) were loaded into a 33-gauge Hamilton syringe, and injected at a rate of 0.5 μl/min with use of an infusion pump. Upon completing injection, the needle was left in place for another minute, then withdrawn slowly to help reduce cell reflux. After closing the scalp with suture and staple, mice were returned to their cages placed on a warming pad and visually monitored until full recovery. Mice were then checked daily for signs of distress, including seizures, weight loss, and tremors, and euthanized as they developed neurological symptoms, including head tilt, seizures, sudden weight loss, loss of balance, and/or ataxia. Once tumor growth was detected via bioluminescence signal, the mice were given a continuous chow-doxycyclin hyclate diet. Tumor growth was followed via IVIS Spectrum *In Vivo* Imaging System (PerkinElmer) as described below.

Bioluminescence imaging (BLI)

Tumor growth was monitored monthly, using the IVIS Spectrum *In Vivo* Imaging System (PerkinElmer), starting at 2.5 months post cell injections. Briefly, mice were injected subcutaneously with 75 mg/kg D-luciferin potassium salt (Promega Cat#E1605) in sterile PBS,

and anesthetized with 2% isoflurane in medical air. Serial BLI images were acquired using the automated exposure set-up. The peak BLI signal intensity within selected regions of interest (ROI) was quantified using the Living Image Software (PerkinElmer), and expressed as photon flux (p/sec/cm2/sr). Representative planar BLI images were displayed with indicated adjusted minimal and maximal thresholds.

In vivo hyperexcitability experiments

Animals were housed according to standard guidelines with free access to food and water in a 12 h light:12 h dark cycle. For hyperexcitability xenograft studies, NSG mice (NOD-SCID-IL2R gamma chain-deficient, The Jackson Laboratory) were used. Male and female mice were used equally. A single-cell suspension from cultured SU-DIPGVI, HSJD-GBM002 or OPBG-GBM-001 neurospheres were prepared in sterile HBSS immediately before the xenograft procedure. Animals at postnatal day (P) 32 were anesthetized with 1–4% isoflurane and placed in a stereotactic apparatus. The cranium was exposed via midline incision under aseptic conditions. Approximately 600,000 cells in 3 μl sterile HBSS were stereotactically implanted into the CA1 region of the hippocampus through a 31-gauge burr hole, using a digital pump at infusion rate of 0.4 μl min^{-1} and 31-gauge Hamilton syringe. Stereotactic coordinates used were as follows: 1.5 mm lateral to midline, 1.8 mm posterior to bregma, −1.4 mm deep to cranial surface. At the completion of infusion, the syringe needle was allowed to remain in place for a minimum of 2 min, then manually withdrawn at a rate of 0.875 mm min^{-1} to minimize backflow of the injected cell suspension.

Transverse 300 μm hippocampal slices were prepared from mice 3-4 weeks after xenografting with a protocol approved by Stanford University APLAC. After rapid decapitation, the brain was removed from the skull and immersed in ice-cold slicing artificial cerebrospinal fluid (ACSF) containing (in mM): 125 NaCl, 2.5 KCl, 25 glucose, 25 $NaHCO_3$ and 1.25 NaH_2PO4, 3 $MgCl_2$ and 0.1 $CaCl_2$. After cutting, slices were incubated for 30 min in warm (30°C) oxygenated (95% O2, 5% CO2) recovery ACSF containing (in mM): 100 NaCl, 2.5 KCl, 25 glucose, 25 $NaHCO_3$, 1.25 NaH_2PO_4, 30 sucrose, 2 $MgCl_2$ and 1 $CaCl_2$, before being allowed to equilibrate at room temperature for an additional 30 min. Slices were transferred to a recording chamber and perfused with oxygenated, warmed (28–30°C) recording ACSF containing (in mM): 125 NaCl, 2.5 KCl, 25 glucose, 25 $NaHCO_3$, 1.25 NaH_2PO_4, 1 $MgCl_2$ and 2 $CaCl_2$. Slices were visualized using a microscope equipped with DIC optics (Olympus BX51WI). Recording pipettes (2–3 MΩ) were filled with 1 M NaCl and placed in proximal strata radiatum of CA1. Field responses were evoked with a bipolar electrode placed in the stratum radiatum to activate Schaffer collateral commissural fibers and connected to an Iso-flex stimulus isolator (A.M.P.I.). Signals were acquired with a MultiClamp 700B amplifier (Molecular Devices) and digitized at 10 kHz with an InstruTECH LIH 8+8 data acquisition device (HEKA). Data were recorded and analyzed using AxoGraph X (AxoGraph Scientific) and IGOR Pro 8 (RRID:SCR_000325) (Wavemetrics). For representative traces, stimulus artifacts preceding the field potential have been removed for clarity.

Pharmakokinetic and blood-brain-barrier penetration analyses

DFCI: N=12 male CD1 mice at 6-8 weeks, 23-24 g (Jihui Laboratory Animal Co. LTD) were treated with one dosage of abemaciclib at 100 mg/kg in 05% methylcellulose or ribociclib at 200 mg/kg in 0.5% methylcellulose, respectively. At 2, 4, 12, and 24 hrs post-treatment, 3 mice per group were sacrificed for plasma and brain homogenate analyses by positive ion mass spectrometry on a UPLC/MS-MS-002 (API-4000) instrument.

ICR: N= 9 female NSG mice (NOD.Cg-Prkdcscid Il2rgtm1Wjl/SzJ ; Charles Rivers; Wilmington, MA, USA) at 6-8 weeks were treated with one dose of abemaciclib/LY2835219 (Selleckchem S5716; Houston, TX, USA) at 150 mg/kg in 1% hydroxy ethyl cellulose (HEC) in 25 mM phosphate buffer pH 2 by oral gavage. At 1, 4 and 24 hrs post-treatment, 3 mice per group were sacrificed for plasma and brain homogenate and analysis was carried out by LC-MS/MS in positive ion mode on a Xevo TQ-S (Waters; Milford, MA, USA).

Treatment of *in vivo* DHG-H3G34 orthotopic xenograft models with CDK4/6-inhibitors

Generation of Akaluciferase labelled cells

Patient-derived primary cell model HSJD-GBM-002 was transduced with lentivirus containing AkaLuciferase with an N-terminal Venus fusion (pLenti-PGK-Venus-Akaluc (neo, which was a gift from Roland Friedel (Addgene plasmid # 124701; http://n2t.net/addgene:124701; RRID:Addgene_124701).[96] After two weeks of chemical selection with G418 (ThermoFisher Scientific; 10131035) at 100 ug/mL and prior to *in vivo* injections, Akaluciferase expression was confirmed using the Akaluciferase substrate, Akalumine-HCl/TokeOni (Bio-Techne Ltd.; 6555; Minneapolis, MN, USA) in an *in vitro* plate-based assay of these cells.

Treatment of *in vivo* DHG-H3G34 orthotopic xenograft model HSJD-GBM-002 with CDK4/6-inhibitors

Six-week-old female NSG mice (NOD.Cg-Prkdcscid Il2rgtm1Wjl/SzJ; Charles Rivers; Wilmington, MA, USA) were treated with buprenorphine 0.03mg/kg and anesthetized with isoflurane 2–4%. Mice were immobilized within a stereotaxic apparatus (Stoelting; Wood Dale, Ill, USA) and 250,000 cells were injected into the right hemisphere at coordinates x -2 mm and y+1 mm from the bregma suture at a depth of 2.5mm using a 10 uL syringe (Hamilton) attached to a stereotaxic arm employing a digital pump (HA1100, Pico Plus Elite; Harvard Apparatus; Holliston, MA, USA).

Tumor growth was monitored monthly, using the IVIS Spectrum CT *In Vivo* Imaging System (PerkinElmer; Waltham, MA, USA), starting at 2 months post-cell injections. Briefly, mice were injected intraperitoneally with 200 uL of 2.5 mg/mL Akalumine-HCl (Akaluciferase substrate) dissolved in sterile H2O and anesthetized with 2% isoflurane in medical air. Eight minutes after substrate injection mice were imaged using the parameters of exposure time: 1 min; field of view: E; binning: large; f/stop: 1. If any signals became

saturated at 1 min exposure time, this was reduced to capture unsaturated data. The peak bioluminescence signal intensity within selected regions of interest (ROI) was quantified using the Living Image Software (PerkinElmer; Waltham, MA, USA), and expressed as photon flux (p/sec/cm2/sr). The photon flux data was used to graph the signal change over time relative to the signal at the start of drug dosing.

Two hundred and fifty days post intracranial injection, the vast majority of animals produced a BLI signal at or above 10^6 photon flux (p/sec/cm2/sr) and animals were divided to generate two groups (n=10 each) with matched bioluminescent signal intensity. Abemaciclib was dosed at 75mg/kg/day (orally) in a 5 day on two day off schedule for a total of 8 weeks while the vehicle group received 1% hydroxy ethyl cellulose (HEC) in 25 mM phosphate buffer pH 2 by oral gavage on the same schedule.

Treatment of *in vivo* DHG-H3G34 orthotopic xenograft model BT690 with CDK4/6-inhibitors

Female NOD SCID mice (4-6 weeks) were injected with BT690 cells at a density of 3 x 10^5 cells in right hemispheres. The skull of the mouse was exposed through a small skin incision, and a small burr hole was made using a 25-gauge needle at the selected stereotactic coordinates zeroed on lambda: -2.0 mm X, +1.0 mm Y and 2.5 mm Z. BT690 cells (300,000 cells in 3μL PBS per mouse,) were loaded into a 33-gauge Hamilton syringe, and injected at a rate of 0.5 μl/min with use of an infusion pump. Upon completing injection, the needle was left in place for another minute, then withdrawn slowly to help reduce cell reflux. After closing the scalp with suture and staple, mice were returned to their cages placed on a warming pad and visually monitored until full recovery. Mice were then checked daily for signs of distress, including seizures, weight loss, and tremors, and euthanized as they developed neurological symptoms, including head tilt, seizures, sudden weight loss, loss of balance, and/or ataxia.

Tumor growth was monitored monthly and, upon intiation of treatment, weekly, using the IVIS Spectrum *In Vivo* Imaging System (PerkinElmer) as described above. Treatment started when mice reached an uniform signal between 10^6 and 10^5 photon efflux across individuals. All treatments with either 75 mg/kg abemaciclib q.d. or 200 mg/kg ribociclib q.d. were performed from Monday through Friday over 56 days. Vehicles utilized for Abemaciclib and Ribociclib consisted of 1% hydroxy ethyl cellulose (HEC) in 25 mM phosphate buffer pH 2, 5%DMSO :95% methylcellulose (3000-5600 cps, 0.5 w/v in water), and 20% 2-hydroxypropyl-β-cyclodextrin (HPBCD) in 25 mmol/L phosphate buffer pH 2, respectively. At clinical endpoint, brains were collected for fresh tumor dissociation or perfused with 4% paraformaldehyde and fixed in formalin for immunostaining/histological analyses.

Immunostaining of PDX brains

Mouse brains collected at survival endpoint were fixed in 4% paraformaldehyde for 24 hours and subsequently stored in 70% ethanol. Fixed mouse brains were cut in half mid-sagittally and embedded in paraffin to generate formalin fixed paraffin embedded (FFPE) blocks. FFPE blocks were sectioned into four-micron thick sections and stained for Anti-Histone H3.3G34R (Biozol, Cat#RMB-31-1120-00) mutant rabbit monoclonal antibody [RM240], Hopx Polyclonal Antibody (Thermo Fisher, Cat#PA5-90538, RRID:AB_2806113), Aquaporin 4 Polyclonal Antibody (Thermo Fisher, Cat#PA5-53234, RRID:AB_2638104), Purified anti-SOX2 Antibody (Biolegend, Cat#656102, RRID:AB_2562246) [14A6A34], Purified anti-Tubulin β 3 (Biolegend, Cat#801201, RRID:AB_2313773), Anti-GABA Antibody (Sigma Aldrich, Cat#A2052, RRID:AB_477652), STMN2 Polyclonal Antibody (Thermo Fisher, Cat#720178, RRID:AB_2606219), Doublecortin Antibody (Santa Cruz, Cat#sc-271390, RRID:AB_10610966) (E-6), Purified anti-Nestin (Biolegend, Cat#656802, AB_2562474) and Purified Mouse Anti-Ki-67 Clone B56 (BD Biosciences, Cat#550609, RRID:AB_393778), by multiplexed IF, as described above.

Bulk RNA sequencing of patient tumors and patient-derived cells

Publicly available RNA sequencing from the European Genome Phenome Archive (EGA) (EGAS00001000192)[3] was combined with data from the Short Read Archive (GSE117446),[22] and newly sequenced pediatric high grade glioma tumors or patient-derived cell cultures. The final dataset comprises 191 primary tumors (9 DHG-H3G34, 81 DMG-H3K27 and 101 H3-wildtype) and 143 sequences from 74 unique cultures (4 DHG-H3G34, 37 DMG-H3K27 and 33 H3-wildtype). FASTQ files were aligned to build 37 of the genome using STAR (RRID:SCR_04463, v2.7.3a) with a full ensembl gene model using standard ENCODE defaults for both single and paired end alignment. Raw counts covering known protein coding ensembl genes from build 37 assembly 87 were recovered using HTSeq (RRID:SCR_005514). Expression data from tumors and cells was processed independently. Differential expression was identified using DESeq2 (RRID:SCR_000154) based upon pairwise comparisons of histone subgroups as above. Pre-ranked gene set enrichments for each dataset were performed with the R package fgsea and gene ontology enrichments were run using clusterProfiler (RRID:SCR_016884). Heatmaps of centered data using the most differentially expressed genes were made with pheatmap.

Bulk RNA sequencing of DHG-H3G34 cell lines treated with CDK4/6-inhibitors

Raw fastq reads were aligned using bowtie (v.0.12.7) to the hg19 reference genome and gene counts were quantified using RSEM (v1.2.19) as expected counts. We determined differentially expressed genes between CDK4/6 inhibition and DMSO treatment using DESeq2 and default parameters (v1.30.1). Gene counts of each sample were normalized by DESeq2's median of ratios method and fitted with a negative binomial regression model. Differentially expressed genes were assessed using Wald's test. Only genes with a p-value (adjusted by Benjamini-Hochberg Procedure) less than 0.05 were selected for subsequent analysis. Statistically significant differentially expressed genes were used for GO term (biological process) enrichment analysis using clusterProfiler v3.18.0. Only GO terms of biological with adjusted p-value < 0.05 were retained. Gene set enrichment analysis was run on fold changes in response to treatment using the R package fgsea (v1.22.0) and heatmaps show ratios of expression relative to DMSO controls.

ChIP sequencing

ChIP-seq was performed from five H3G34R/V-mutant patient derived high grade gliomas (Active Motif). ChIP was performed using antibodies against H3K27ac (Active Motif, Cat#39133, RRID:AB_2561016), H3K27me3 (Active Motif, Cat#39155, RRID:AB_2561020), H3K36me3 (Active Motif, Cat#61101, RRID:AB_2615073), H3K9me3 (Active Motif, Cat#39161, RRID:AB_2532132) and RNA polymerase II (Active Motif, Cat#39097, RRID:AB_2732926). ChIP of G34R and G34V mutant H3.3 was performed separately and compared to total H3.3. Single ended sequence data was aligned to build 37 of the genome using bwa with default parameters. Both broad and narrow peaks were called using MACS3 (v3.0.0) with reference to input controls. Super Enhancers in H3K27ac data were identified with ROSE. Peaks were annotated using both HOMER (RRID:SCR_010881) and chipPeakAnno. Smoothed coverage vectors binned across 100 bp regions for each sample were recovered using the GenomicAlignments R package and are shown as bigWig tracks using Rtracklayer. Binding surrounding transcription start and end sites and covering coding regions of known ensembl genes were calculated with use of both GenomicAlignments and ngs.plot.

For comparison of H3K27ac SuperEnhancers ChIP-Seq data from DMG-H3K27 (n=6) and histone WT (n=3) patient-derived pediatric high-grade glioma cultures was recovered from the short read archive[22] (GSE117446) and processed in the same way. Epigenetic states across the genome were defined using chromHMM based upon a 10 state model with reference to those defined in ENCODE 15.[97] Differential binding analysis comparing DHG-H3G34 samples with either DMG-H3K27 or H3-wildtype cells was performed using the diffbind R package based upon DESeq (RRID:SCR_000154) methodology.

DNA methylation array analysis

DNA methylation microarray data from pediatric HGGs profiled on the Infinium HumanMethylation450 and EPIC BeadChip arrays were combined from publicly available repositories - GSE109379 and GSE90496,[84] GSE73801,[85] E-MTAB-5528.[18] Raw methylation IDAT files were preprocessed using the minfi package in R. The Heidelberg brain tumor classifier (molecularneuropathology.org) was used to assign subtype scores for each sample compared to 91 different brain tumor entities using a training set built from more than 2000 tumors implemented in the mnp.v11b4 R package. Samples with a classification of GBM_G34, DMG_K27, GBM_MYCN, GBM_RTK_III, GBM_MID with a calibrated score >= 0.9 were used for dimensionality reduction and differential methylation analysis (n = 295). A matrix of beta-values was pre-filtered to remove cross-hybridising probes, probes with a minor allele frequency (MAF) of 5% or higher and probes up to 2 base-pairs from a known single-nucleotide polymorphism (SNP).[98,99] Differential methylation was compared between H3.3G34RV, H3K27M and histone WT groups using the DMRcate R package. The averages of smoothed beta values covering target genes within histone subgroups were plotted using the GViz R package and GSEA was carried out using the fgsea R package.

Affymetrix microarray expression datasets

Microarray data from pediatric HGGs profiled on Affymetrix U133 plus 2 arrays was merged from publicly available GEO datasets - GSE19578,[100] GSE26576 [101] GSE34824,[2] GSE36245,[4] GSE49822,[102] GSE50161,[103] GSE73038,[85] GSE134404.[104] The final dataset comprised 195 tumors (23 DHG-H3G34, 53 DMG-H3K27 and 93 H3-wild-type). U133 plus2 CEL files were read and normalized using rma in the affy R package. Differential expression was identified with limma based upon pairwise comparisons between DHG-H3G34, DMG-H3K27 and H3-wild-type groups.

Genomic DNA library preparation and sequencing

Genomic DNA was extracted from cell pellets using the QiaAMP DNA Blood Maxi Kit (Qiagen) following manufacturer's protocol. PCR amplification of the gDNA was performed as described.[105] Briefly, for each sample, 400 μg of gDNA was amplified in 266x 50 μl PCR reactions using the NEBnext high-fidelity 2X PCR Master Mix, pooled forward primers (NGS-Lib-FWD-1 - 10, 0.25 μM) and a unique barcoded reverse primer (0.25 μM) for each sample. Large-scale PCR purification was performed using the Zymo-Spin V with reservoir (Zymo Research), all steps were carried out at room temperature. PCR reactions for each sample were pooled, mixed with 5 volumes of DNA binding buffer (Zymo Research) and transferred to the Zymo-Spin V with Reservoir in a 50 ml falcon tube and centrifuged at 500x*g* for 5 min. Zymo-Spin V columns were washed twice with 2 ml DNA Wash Buffer (Zymo Research), centrifuged at 500x*g* for 5 min each time. Zymo-Spin V columns were then placed into 2 ml collection tubes and centrifuged at >13,000 rpm for 1 min to remove residual wash buffer. Zymo-Spin V columns were incubated with Elution Buffer (Zymo Research) for 1 min and placed into 1.5 ml microcentrifuge tubes and centrifuged at >13,000 rpm for 1.5 min, this was repeated for an additional elution for each column. Purified PCR samples were quantified using NanoDrop (Thermo Scientific), pooled in equal concentrations and gel-purified before submission for next-generation sequencing (read depth 500-fold) using the Illumina NextSeq500.

scRNA-seq and snRNA-seq data generation

ScRNA-sequencing of primary patient tumors were performed in one experimental run, which is typical for human studies due to limited tissue availability. Whole transcriptome amplification, library preparation, and sequencing of single cells and single nuclei was performed using the Smart-seq2 modified protocol as previously described.[8,32,33,106,107] RNA was purified with Agencourt RNAClean XP beads (Beckman Coulter). Oligo-dT primed reverse transcription was performed using Maxima H Minus reverse transcriptase (Life Technologies) and a template-switching oligonucleotide (TSO) containing a locked nucleic acid (LNA) (Qiagen). Subsequent PCR amplification was performed using KAPA HiFi HotStart ReadyMix (KAPA Biosystems), followed by Agencourt AMPure XP bead (Beckman Coulter) purification. Library tagmentation was performed using the Nextera XT Library Prep kit (Illumina).

Libraries from 768 cells with unique barcodes were combined and sequenced on a NextSeq 500 sequencer (Illumina) using a NextSeq 500/550 High Output Kit v2.5 (Illumina).

QUANTIFICATION AND STATISTICAL ANALYSIS

Statistical tests were performed using GraphPad Prism 8 (RRID:SCR_002798), R 4.0.3 or Python 2.7/3.6. For computational as well as cell/molecular biological methods, statistical analyses are described in detail in respective methods chapters as well as indicated in figure legends and in corresponding results sections. For statistical comparisons within two groups, we used a two-tailed Student's t-test. Significance values are given in figures, figure legends, and/or the results section.

Adjustment of p-values for multiple testing was carried out using false discovery rate (FDR), Benjamini Hochberg (BH) or Bonferroni correction where indicated. Treatment conditions compared statistically are indicated in figures, figure legends and/or the results section. Data points represent mean values ± SEM, as specified in figure legends and corresponding methods sections. In boxplots, boxes show the median and interquartile range, whiskers show the 1.5x interquartile range (IQR), individual values are plotted with jitter.

Analysis of genome-wide screening data

For OPBG-GBM-001, the python library MAGeCK was used to map reads from each condition to the GeCKOv2 guide reference library. Maximum-likelihood estimation (MLE) of gene essentiality was carried out using MAGeCK on raw read counts by comparing T0 with T8, and T0 with T10. For visualization purposes, raw MAGeCK read counts were used. Guides with read counts < 50 and genes with 2 or fewer guides were removed. T10 counts were normalized by the ratio of median counts of the non-targeting controls between T0 and T10. Genes, where > 50% of guides exceed extreme values of 5x replicate median, were removed. The python library CHRONOS[108] was used to generate gene-level screen effect scores across experiment timepoints in OPBG-GBM-001 comparable to scaled CERES scores (see section below) obtained from DepMap (RRID:SCR_017655). The un-scaled gene effect obtained from CHRONOS was scaled so that the median score for common essential genes is -1 and non-essential genes is 0. For OPBG-GBM-001, the lists of essential and non-essential genes were obtained from an earlier DepMap dataset that utilized the GeCKO CRISPR-Cas9 genome-wide library (GeCKO 19Q1), with the addition of 1,000 non-targeting control guides to the non-essential list.

For KNS42, processed data was obtained from the DepMap Portal for release 20Q2. Full analysis methodology is detailed as previously published.[60,61] Briefly, raw read counts were summed by replicate and guide. Guides with off-target effects were removed. Replicates which failed fingerprinting with parental of derivative lines and those with fewer than 15 million reads were removed. For each replicate, counts per million (CPM) were calculated, a pseudo-count of 1 added and counts log2-fold-change calculated from pDNA. Null-normalized mean difference (NNMD) was calculated for each replicate for genes as previously described.[109,110] Replicates per line were removed where Pearson correlation <= 0.61 with at least one other replicate across top 3% most variable genes by gene effect variance. Gene-level scores were calculated by CERES which takes into account copy-number effects of the genomic region targeted by the sgRNA that can confound cell viability and subsequent sgRNA depletion into a least square regression model to infer the gene-knockout effects.[61] Obtained scores were then scaled so that the common essential gene median in each cell line was -1. Genes were normalized to have a mean of 0 and a variance of 1 and first 5 principle components were removed from the data, then re-scaled for common essential gene medians to equal -1. Genes on X chromosome where detailed copy number for lines was not available were replaced with NA, as were 1,309 genes in 12 cell lines due to contamination.

Integration of CRISPR screen readouts at multiple timepoints using the Chronos model

Chronos[108] assumes that cells infected with an sgRNA are divided into two populations: those where the function of the targeted gene remains intact (e.g. due to in-frame INDEL mutations), which continue proliferating at the original rate, and those where the gene was successfully knocked out, which proliferate at some new, potentially negative rate. For an sgRNA i targeting gene g in cell line c, the number of cells Ncj with the sgRNA at time t after infection is

$$N_{cj}(t) = N_{cj}(0)\left(p_{cj}^{e^{R_c(1+r_{cg})t}} + (1 - p_{cj})e^{R_c t}\right)$$

where pcj is the probability that the sgRNA achieves knockout of its target, Rc is the unperturbed growth rate of the cell line, and rcg is the fractional change in growth rate caused by knockout of the targeted gene. This last term is the gene score. sgRNAs targeting more than one gene were excluded.

Knockout probability per sgRNA and cell line approximate was approximated as the product of a per-line and per-sgRNA factor, both constrained to the interval [0, 1]: pci = pc pi. Delay between infection and the emergence of the knockout phenotype is termed dg. The proportion of all reads that map to a particular sgRNA assumed to have expectation equal to the proportion of cells with that sgRNA:⟨nci⟩= Nci / $\sum$ i Nci. Chronos' estimation of nci is νci. Then,

$$v_{ci}(t > d_g) = v_{ci}(0)\left(1 + p_c p_i\left(e^{R_c r_{cg}(1-d_g)} - 1\right)\right) \Big/ Z_c(t)$$

where Zc is a normalization term:

$$Z_c(t) = \sum_i 1 + p_c p_i \left(e^{R_c r_{cg} \left(1 - d_g\right)} - 1 \right)$$

Chronos aimed to maximize the likelihood of the observed readcount fractions nci according to the NB2 parameterization of the negative binomial distribution. The NB2 cost was defined (up to an additive constant).

$$C_{\mathrm{NB2}} = \sum_{c,i,k} \left(n_{ci}(t_k) + \alpha_c^{-1} \right) \ln \frac{1 + \alpha_c v_{ci}(t_k)}{1 + \alpha_c n_{ci}(t_k)} + n_{ci}(t_k) \ln \frac{n_{ci}(t_k)}{v_{ci}(t_k)}$$

where νci is the model prediction of the normalized readcounts and k enumerates the timepoints measured. The overdispersion parameter αc of the NB2 model was set to 0.05.

scRNA-seq data processing

Pre-processing of scRNA-seq data was performed as previously described with some modifications.[32,106] Raw sequencing reads were aligned to hg19 genome using hisat2 aligner (v2.1.0), and expression levels were calculated as *Ei,j* = log2(TPM*i,j*/10 + 1) for gene *i* in sample *j*, with TPM referring to transcript-per-million as quantified by RSEM (version 1.3.0).[86] For snRNA-seq data, we included introns in gene annotation files. TPM values were divided by 10 for better approximation of the estimated complexity of single-cell libraries, which is in the order of 100,000 transcripts. We detected a median of n=2,687 uniquely expressed genes in the fresh cells and a median of n=2,643 genes in the frozen nuclei. For quality control filtering, we applied a threshold of >2,000 uniquely detected genes and average expression of a curated set of housekeeping genes >2.5 for fresh tumors. For frozen tumors, a threshold of >1,000 uniquely expressed genes and an alignment rate of >0.4 was employed. To filter out lowly expressed genes, we removed genes with TPM greater than 10 in less than 10 cells. For the remaining cells and genes, we calculated the aggregate expression of each gene as *Ea(i)* = log2(average(TPM*i,1...n*) + 1), and defined relative expression as centered expression levels, *Eri,j* = Ei,j − average[Ei,1...n].

Analysis of CNAs in single-cell data

Copy number aberrations (CNAs) were estimated as previously described by sorting the analyzed genes by their chromosomal location and computing a moving average of the relative expression values within a sliding window of 100 genes in each chromosome using the inferCNV package.[8,32,34,106] Spike-in non-malignant cells or nuclei from previous publications[8,106] were used as reference normal karyotype and their average CNA values were subtracted from each cell. Hierarchical clustering of the single-cell copy-number profiles within each sample with the reference non-malignant copy-number profiles was used to classify the presence of CNAs. In fresh tumors, most cells exhibited clear evidence of CNAs (Figure S1B) and did not cluster with the non-malignant cells. Six of seven frozen tumors were found to harbor cells with CNAs, while one tumor (ICR-CXJ-041) did not present any cells with an evident CNA signal. This could be either due to absence of CNAs or malignant cells in this sample or due to technical artefacts arising from frozen nuclei data. If these cells without evident CNAs did not cluster with the non-malignant spike-ins in subsequent gene expression-based clustering, they were retained as malignant cells (see below).

Clustering analysis and visualization

Highly variable genes (HVGs) were defined using the Seurat v4 pipeline as the top 2,000 genes with the highest standardized variance after applying a variance-stabilizing transformation (vst) using local polynomial regression to account for the mean-variance relationship inherent in scRNA-seq data.[111] *Z* score transformed expression values of these HVGs were used for linear dimensional reduction by principal component analysis (PCA). The number of statistically significant principal components (PCs) was determined by Seurat's permutation testing-based JackStraw procedure, and/or by ranking PCs according to the percentage of total variance explained. The selected PCs were used for Seurat's graph-based clustering procedure using Louvain clustering based on a K-nearest neighbor (KNN) graph. We then visualized these clusters using uniform manifold approximation and projection (UMAP), depicting good separation of clusters (Figure 1C). The majority of clusters contained cells from a single sample, but two clusters included cells from multiple samples and showed high expression of cell type specific marker genes for oligodendrocytes (*MBP, KLK6, MOG*) and immune cells (*CCL3, CD14, CSF1*).

Integrated definition of malignant cells

We combined CNA analysis with gene expression-based clustering and expression of non-malignant marker genes to classify malignant and non-malignant cells. Non-malignant cells showed high expression of oligodendrocyte or immune cell specific marker genes, clustered with spike-in non-malignant cells and concordantly lacked apparent CNAs. As such, malignant cells were defined as those which were not part of the clusters with high expression of markers for non-malignant cell types and exhibiting CNAs. Cells with discordant classifications by clustering and CNA detection were excluded from downstream analysis.

Analysis of the H3.3G34R/V-mutation in Smart-Seq2 data

Sequencing reads were aligned to GENCODE's Human Reference Genome Build hg19 (GRCh37p.13) using STAR (v2.7.3a). The H3.3G34R/V (at position G35) was then quantified in each cell at coordinate 226252155 of chromosome 1 using the mpileup function

of samtools (v1.13). We next filtered out lower quality reads (phred score <20) and counted the total number of reads with either reference (G) or mutant (A) nucleotide at this genomic position in each cell. We then determined the proportion of reads with the mutant nucleotide (A) as the RNA 'variant allele frequency (VAF)'. Only cells with sequencing coverage greater than 10 (i.e., at least 10 reads mapped to this genomic coordinate) were used to compare H3.3G34R RNA VAF between different malignant and non-malignant cell populations.

Identification of intra-tumor variability programs using NMF

Non-Negative Matrix Factorization (NMF) was applied to the centered expression data (with negative values converted to zero, number of factors set to 6) of tumor cells within each sample individually[8,106,107] using the top 10,000 over-dispersed genes, as determined by PAGODA2.[87] The top 50 genes with the highest NMF weights were considered as representative for each of the resulting NMF factors, respectively. All malignant cells from each sample were then scored for these top 50 genes of each NMF program and the NMF programs were ordered by hierarchical clustering (distance metric: one minus Pearson correlation; linkage: Ward's linkage) based on these scores. Positively correlated (Pearson correlation coefficient >0.4) NMF programs were retained and combined into metaprograms based on the top 50 genes with the highest average NMF weight within each metaprogram (Table S2). To control for potential artefacts arising from technical differences, we derived NMF programs separately for fresh and frozen tumors. Five different metaprograms were identified in fresh samples. In frozen tumors, an additional metaprogram consisting of mitochondrial genes was detected. As nuclei highly expressing this 'mitochondrial metaprogram' also ranked in the lower tier of alignment rates, we considered these to be low-quality nuclei and removed those from downstream analysis. NMF analysis was again performed on the remaining 1,098 nuclei, resulting in five metaprograms for the frozen samples. For integrated analysis of fresh and frozen metaprograms, we retained the cycling and more granular RG-like, NPC-like, INPC-like, and eIN-like interneuronal lineage metaprograms derived from fresh tumors, and the AC-like and MES-like metaprograms uniquely derived from frozen tumors to a combined set of seven metaprograms, which we then scored onto all fresh and frozen single cells/nuclei for downstream analyses.

Definition of single-cell expression scores

Single-cell expression scores were computed similarly as described previously.[8,106,107] For a set of genes (*Gj*) reflecting a NMF program, metaprogram or specific cell type, a score, SCj(i), which quantifies the relative expression of Gj for each cell i, was calculated as the average relative expression (Er) of the genes in Gj, compared to the average relative expression of a control gene set Gcont: SC(i) = average[Er(G , i)]−average[Er(Gcont, i)]. The control gene set is defined as the 100 genes with the most similar aggregate expression level to each gene included in the set of genes to score, and thus represents a comparable distribution of expression levels to that of the considered gene set while being 100-fold larger. Single cells from fresh or frozen tumors were assigned to different cell subpopulations based on their maximum expression score for respective metaprograms. Cells were classified as 'cycling' or 'non-cycling' based on their maximum scores for the cycling programs (larger or smaller than 1 in fresh tumors and 0.5 in frozen tumors, respectively).

Data integration and graph-based clustering

As an orthogonal analysis of tumor cell heterogeneity, graph-based clustering following data integration was performed. The top 2,000 HVGs were selected using Seurat (see 'clustering and data visualization') and used for PCA analysis. To account for sample-specific batch effects and discern these from cell subpopulation-specific variations, the linear adjustment data integration method Harmony was applied to the first 100 principle components to create a corrected embedding.[89] The first 20 Harmony corrected dimensions were then used for Seurat's Louvain clustering algorithm and to generate a UMAP embedding using Seurat's RunUMAP function.

Annotation of metaprograms and projection onto normal human brain atlas

We characterized the metaprograms by comparison to glioma and non-tumor reference datasets. First, we compared expression of metaprogram marker genes to those of individual metaprograms previously identified in DMG-H3K27 glioma and H3/IDH-wild-type glioblastoma by scRNA-seq.[8,32]

Next, we projected the DHG-H3G34 metaprograms onto a human brain single-cell atlas.[25] We aggregated expressions of all reference cells by their reported cell type annotation and scored those for the DHG-H3G34 metaprogram marker genes. To integrate DHG-H3G34 scRNA-seq data with the human cortex reference scRNA-seq data, Seurat's (v4.3.0) reciprocal principal component analysis ('RPCA') approach was used which projects each dataset into another's PCA space, thereby identifying shared correspondences/anchors and creating a batch-effect corrected count matrix for joint downstream analysis.[112,113]

Differential gene expression analysis in cell subpopulations

We tested for differential gene expression between cell subpopulations using a two-sided Wilcoxon rank sum test based on comparison of log transformed uncentered expression values, as implemented in Seurat. Genes with a Bonferroni-adjusted p-value <0.05, at least 2-fold mean difference and expressed in at least half the number of cells for the particular cell population were defined as differentially expressed (Table S2).

Pseudotime analysis of scRNA-seq cell populations

We inferred pseudotime ordering of all non-cycling tumor cells by Slingshot.[88] Slingshot constructs a cluster-based minimal spanning tree to identify global lineage structure and fits a principal curve to represent each lineage. We first computed a diffusion map embedding using log2 transformed expression levels of the top 2,000 highly variable genes and default values for other parameters by the R package destiny's DiffusionMap function. The first two dimensions of the resulting diffusion map (DC1/2) were used for downstream analysis. Pseudotime inference was implemented using the Slingshot function with default parameters. We next fit a general additive model (GAM) to each gene to identify temporally dynamic genes that change their expression over the course of the trajectory and we retained genes with adjusted p-values less than 0.05.

Integration of DHG-H3G34 scRNA-seq data with genetically edited human forebrain neural stem cell transcriptomes

Bulk transcriptomic data of human embryonic forebrain neural stem cells, +/- genetically engineered to express the H3.3G34R-mutant histone with *TP53* and *PDGFRA* co-alterations (PP5G & PP5W) were downloaded from GSE163044.[20] Raw counts were converted to TPM and scored for the DHG-H3G34 fresh and frozen metaprogram marker genes. Resulting scores were compared between genetic conditions using a two-sided Student's t-test.

Integration of DHG-H3G34 Smart-Seq2 data with published 10x scRNA-seq data

10x scRNA-seq fastq files generated for 16 patient DHG-H3G34 tumors as published by Chen et al., 2020,[19] were downloaded from EGAS00001004301 and aligned to hg38 pre-mRNA using cellranger-7.2.0. Preprocessing and QC-filtering were performed using sample-specific QC metrics as previously indicated.[19] To avoid potential technical biases, 2 freshly processed tumors were removed, and 14 frozen tumors retained for downstream analyses. Single cells were annotated as malignant and non-malignant cell types based on CNV calling, graph-based clustering and marker gene expressions, resulting in 34,638 high-quality malignant cells. Sample-specific batch effect correction using Harmony was performed on the remaining cells, followed by Seurat's graph-based clustering. Tumor cells were then scored for the DHG-H3G34 tumor metaprograms identified in the Smart-Seq2 data. Only cells with single-cell cores >0.2 (n=31,272 cells) were assigned to a tumor metaprogram, while cells that did not meet this cutoff were removed from the final clustering.

Identification of active transcription factors and their regulatory modules

Active TFs and their gene targets in the single-cell dataset were inferred using single-cell regulatory network inference and clustering (SCENIC).[38,114] First, coexpression modules between TFs and putative target genes were estimated by GENIE3. Second, putative regulatory regions of the inferred target genes were queried for enriched cis-regulatory motifs using RcisTarget and indirect targets lacking motif binding sites were pruned. Next, the activities of the resulting regulatory modules (regulons, modules of target genes co-expressed with TFs and enriched with motifs for correct upstream regulators) were scored and binarized by AUCell, which classifies if an inferred regulon is active in each cell based on the distribution of regulon activity across all cells. To compute regulon activities for each cell subpopulation, we averaged the regulon activity across all cells in each subpopulation and also computed proportions of cells within a subpopulation classified as active for that regulon (Table S4). To further identify cell type-specific regulons, we computed a regulon specificity score (RSS) by gauging the distance between the distribution of regulon activities and the distribution of metaprogram annotations using Jensen-Shannon Divergence.[114]